Mechanisms and Kinetics of Electron Injection in Dye-Sensitized Solar Cells

Mindaugas Juozapavicius

Department of Physics

Imperial College London

A thesis submitted for the degree of

Doctor of Philosophy

January 2015

Abstract

Electron injection in dye-sensitized solar cells (DSSC) has been extensively studied in the present thesis. Many transient and steady-state experimental techniques were utilized: ultrafast transient absorption spectroscopy in the visible, near-IR and mid-IR regions; time-correlated single photon counting; incident photon to current conversion measurement; temperature dependence of luminescence and device efficiency; determination of energy conversion efficiency parameters. All these methods were collated and analysed as a whole, providing a very detailed picture of the electron injection. It was found that in devices utilizing the most efficient Ru-bipyridyl dyes and commercially viable, performance optimized iodine/triiodide electrolytes, electron injection kinetics are multiphasic, with significant components in the femtosecond, tens of picoseconds and in nanosecond regimes. The broad non-exponential kinetics gave rise to non-100% efficient injection. A fraction of the dyes manage to decay giving rise to luminescence. All of these observations were fully quantified and validated by performing measurements on different systems. The huge length of the delay lines in TAS measurements and very broad probe wavelengths used in the current work gave a very detailed picture of the injection process. Along the way, some very basic experiments were done, which added confidence to the results obtained in the thesis. In addition, interesting phenomena occurring in the ultrafast timescales were found and spectra of transient species such as the dye excited states were recorded. Finally, relevance of the current work to the practical aspects of the solar cells was described and future work discussed.

Table of Contents

Abstract 2
Table of Contents 3
Declaration of Originality 6
Copyright Declaration 7
Chapter 1. Introduction 8
Introduction 8
Background: global energy landscape 8
Photovoltaics and DSSC 8
DSSC working principles 9
Literature review 12
Structure of the Thesis 18
Chapter 2. Experimental methods & techniques 19
Introduction 19
Solar cell materials: dye solution, TiO_2 paste, ZrO_2 paste, electrolytes, electrodes 19
Solar Cell Preparation. 20
Sapphire and CaF_2 devices manufacturing 21
Film thickness measurements 22
Temperature control equipment 22
Current-voltage equipment 22
UV-Vis absorption equipment 22
IPCE equipment 23
TCSPC equipment 23
Ultrafast transient absorption spectroscopy in the mid-IR 24
VIS/Near-IR ultrafast TAS 25
Chapter 3. Methods and Theory 26
Introduction 26
Ultrafast pump-probe transient absorption spectroscopy 26
Probe chirp 27
Perturbed free induction decay in vibrational spectroscopy 28
Cross-phase modulation 28
Time-Correlated Single Photon Counting 29
Reliability of the TCSPC equipment 30
IPCE front/back method 33

Chapter 4. Transient absorption spectroscopy in the mid-IR 34
Introduction 34
Experimental methods 34
Visible pump, mid-IR probe of N719 on ZrO_2 35
Transient spectra at 4000 – 5700 nm range 35
Assignment to SCN and steady-state FTIR 36
Long-lived absorption in the TAS before time zero: another experimental artefact 37
Absorption of photoexcited N719 on ZrO_2 after pump pulse 39
Pump-probe spectroscopy in the mid-IR of dyes on TiO_2 40
Experimental conditions 40
Spectrum of photoexcited N719 and D149 on TiO_2 41
Subtraction of before-time-zero negative absorption change 42
Discussion of spectra 43
Discussion of kinetics 44
High light intensity induces ultra-fast apparent injection kinetics 45
D149 TAS analysis: kinetics 47
Acidity causes band edge shifts, which results in lower V_{oc} 47
Sample translation vs no translation 48
Pulse peak-power intensity independence of electron injection 49
Additional spectra around 7500 nm 50
The measurements in perspective 51
Open circuit condition used for TAS 52
Last words on the mid-IR spectra 52
Conclusion 53
Chapter 5. Visible to near-IR transient absorption spectroscopy 54
Introduction 54
Experimental 54
Vis-NIR femtosecond transient absorption setup 54
Sample preparation 55
Device description and their absorption spectra 55
Current-voltage and performance of the solar cells 56
Samples do not degrade or change during the TAS measurements 57
Pump pulse intensity affects amplitude linearly and does not change absorption difference dynamics 58

Short circuit or open circuit measurement conditions do not impact injection kinetics 59
Photo-excited N719 on ZrO_2 does not undergo any charge transfers 60
Spectrum of N719 on TiO_2: electron injection 61
The Vis/NIR kinetics of N719 on TiO_2 62
The Vis/NIR kinetics of C106 on TiO_2 66
Conclusion 70
Chapter 6. Electron injection mechanisms and efficiency 71
Introduction 71
Device details and absorption 71
Current-Voltage and device efficiencies 72
Photon to current conversion efficiency measurements 74
Time-resolved Photoluminescence 81
Ultrafast pump-probe spectroscopy in the mid-IR 84
Discussion of electron injection 85
Temperature dependence of electron injection 88
Conclusion 90
Chapter 7. Summary and further work 92
References 94

Declaration of Originality

This thesis is a write-up of the work carried out at Imperial College London during my time as a PhD student. The work was supervised by Dr. Brian C. O'Regan and Dr. Martin Heeney. In addition, some parts of the work were done in collaboration with Dr. Marius Kaucikas and Dr. Jasper van Thor. The work presented here is a product of my own work, unless otherwise stated in specific cases. Neither any parts nor the whole of this thesis have been submitted for the award of a degree at this or any other institution.

Mindaugas Juozapavicius

January 2015

Copyright Declaration

The copyright of this thesis rests with the author and is made available under a Creative Commons Attribution Non-Commercial No Derivatives licence. Researchers are free to copy, distribute or transmit the thesis on the condition that they attribute it, that they do not use it for commercial purposes and that they do not alter, transform or build upon it. For any reuse or redistribution, researchers must make clear to others the licence terms of this work.

Chapter 1. Introduction

Introduction

In this Chapter, a general motivation for the PhD is provided. The basic underlying principles of solar energy and dye-sensitized solar cells are discussed. Electron injection is introduced and motivation for its study is given. Finally, a critical literature review follows, providing a historical context to the research done on electron injection along with analysis of several important papers. Structure of the thesis is outlined at the end of the Chapter.

Background: global energy landscape

The current global reliance on fossil fuels as a source of energy is bound to come to an end.[1] In the long term, the fossil fuel reserves are not being replenished fast enough. In the short term, there is strong evidence that introducing greenhouse gases into the atmosphere via oxidation of the fossil fuels contributes to global climate change, which may result in ice cap melting and flooding of coastal areas, among other consequences.[2] Current nuclear fission based reactors require radioactive materials uranium or plutonium, reserves of which are also finite. Alternative renewable sources which are not environmentally hazardous are several, namely, wind, geothermal, hydro, fusion and solar. Out of all of these, only solar power is a fully viable option to replace the majority of energy sources in the next decades. Only solar energy is viable because the technology to do that currently exists and there is more than enough power available to be harvested, as at any given moment the sun provides roughly 100,000 TW of power. This is the average amount of power reaching the surface of the Earth from the Sun.[3] The current global power consumption is estimated to be roughly 20 TW. Developing affordable and environmentally friendly solar power harvesting equipment would completely solve the future energy issue. Out of the available solar power harvesting technologies, only photovoltaics will be reviewed in this thesis and only one type, the dye-sensitized solar cells (DSSC) will be considered and discussed in detail.

Photovoltaics and DSSC

A photovoltaic device converts energy contained in light directly to electric energy. There are several different technologies currently available, although most require considerable amounts of further research. These technologies are different in terms of their manufacturing procedures, materials required and mechanisms of operation.[4] To use the National Renewable Energy Laboratory (NREL)

classification, there are 5 different types, namely: multi-junction, single-junction GaAs, crystalline silicon, thin-film technologies and emerging photovoltaics.[5] All except the emerging photovoltaics are based solely on semiconductor technology, where an absorbed photon directly creates an electron-hole pair in the semiconductor material, with the energy of the pair at or above the valence - conduction band gap. The emerging photovoltaic technologies are mainly based on molecular absorbers. Due to the discrete nature of the absorber, in contrast to the continuous crystalline or amorphous semiconductor structures, these devices are also sometimes referred to as "excitonic" solar cells.[6] In contrast to high-efficiency semiconductor photovoltaics, the emerging, molecular based devices are potentially cheaper to manufacture because they are made of discrete components. Molecular components can be produced cheaply in bulk, after the synthetic process is optimized. Once the components are ready, the device assembly process lends itself to the well-developed printing technologies. For example, organic photovoltaics can be ink-jet printed, or better yet, gravure printed, a method which is currently used for printing newspapers.[7] Such processes are very fast and cheap as neither high temperatures nor ultra-high vacuum are required. Another important example, the DSSCs can be produced using roll-to-roll processing, while the metal oxide semiconductors can be deposited with either screen printing or doctor blading.[8] Several commercial firms have demonstrated this successfully by developing these processes, one example of which is the UK based "G24 Power Limited".

Before the seminal paper reporting > 7% efficient DSSC,[9] there were some early attempts at the dye-sensitization idea for power generation. Some of the early attempts originated from photography,[10] leading to sensitized semiconductors, organic dye sensitized ZnO [11] and later to sensitized TiO_2.[12] Only since 1991, after the demonstration of > 7% efficient DSSC, the interest in DSSC technology soared and at the time of writing of this thesis, there are more than 20,000 citations of the Nature paper.[13]

DSSC working principles

The introduction and discussion of the working principles of DSSCs in this section is based on several references, [14], [15], [16]. In the most general case, a DSSC is composed of a light absorbing component, a semiconductor for transporting one of the separated charges and an opposite charge transporting component. In contrast to conventional semiconductor photovoltaics, where the electron-hole pair is separated by an inner electric field, in a DSSC, the electron/hole pair is separated by a nearby semiconductor component with a lower energy for accepting electrons or holes. If the transport of the electrons away from the interface, where the light absorbers are

located, is faster than electron-hole recombination, an electric current will be generated. In this thesis, either a purely organic compound or a ruthenium metal-centered complex was used as a dye, adsorbed via carboxylic acid anchoring groups to a TiO_2 nanocrystalline, mesoporous high surface area semiconductor. For hole transport, an electrolyte based on the I^-/I_3^- redox couple was used. A scheme of the main electronic processes that follow light absorption is given in the Figure 1.1.

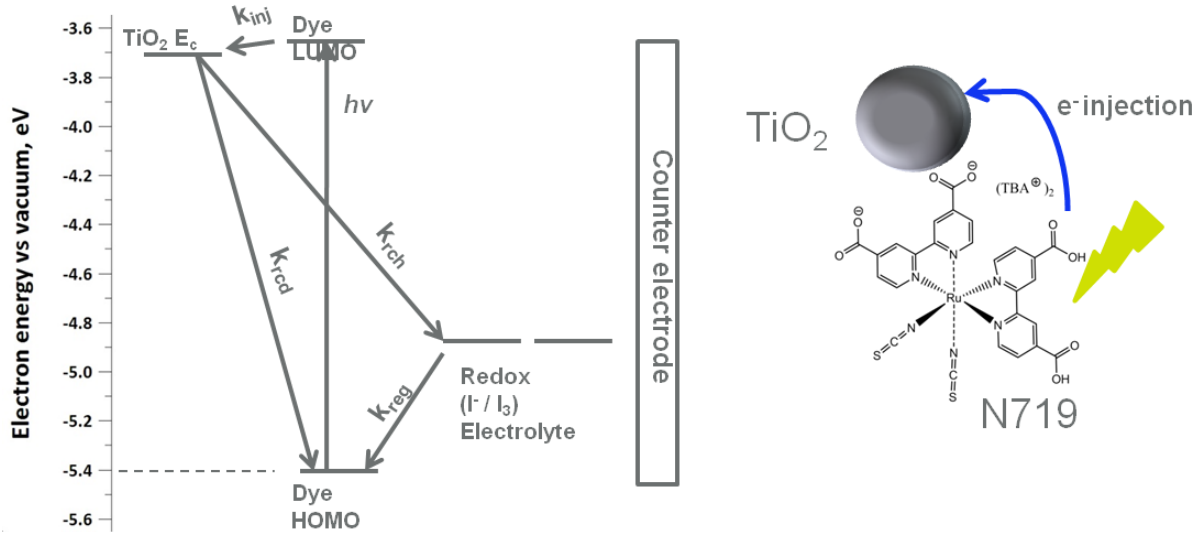


Figure 1.1. Fundamental electron transfer processes in a typical DSSC.

For a DSSC to have a high percentage of photons resulting in current generation, kinetic competitions between different electronic transitions presented in Figure 1.1 have to favour the charge separating route. First, after the dye molecule is optically excited and an electron is promoted to the dye's lowest unoccupied molecular orbital (LUMO), the rate of electron transfer (injection) to the metal oxide has to be higher than the natural decay of the excited state of the dye back to the ground state. After injection, there are two loss pathways: electron may recombine back with the oxidized dye or it may react with an electron acceptor in the electrolyte. Transport of the electron to the transparent conducting electrode on which the TiO_2 is deposited has to be faster than both these processes. When electron is injected into the TiO_2, a photooxidized dye is left on the surface. It has to be regenerated back to the ground state of the neutral dye in order for the dye to not degrade and become again available for further light absorption. This step is known as the regeneration. The rate of regeneration has to out-compete the k_{rcd}, which is the electron recombination to the photooxidized dye. Finally, the transport of the oxidized species in the electrolyte, in this case an I_3^- molecule, towards the counter electrode has to be faster than the k_{rch}, the electron recombination with the I_3^- molecule. Once the I_3^- reaches the counter electrode and the injected electron reaches the working (front) electrode, the electron can do work in an external circuit and then recombine with the I_3^- species to form I^- species, which originally regenerated the

oxidized dye. When this happens, the electronic circuit is complete and conversion of light to electricity is achieved.

An experimental technique which measures the efficiency of the final combination of all these processes is known as incident photon to current conversion (IPCE). Taking IPCE and accounting for only the absorbed photons, absorbed photon to current conversion (APCE) efficiency is obtained, which is the process just described in this section as only the absorbed photons were taken into account. When the solar cell is short-circuited and the current is measured upon light illumination, the amount of electrons coming out is given by the short circuit current (J_{SC}).

Nothing has been said about the amount of energy that is extracted from the absorbed photons yet. The amount of energy that can be extracted from each electron coming out of the solar cell is determined by the potential difference (Fermi level of electrons) between the working and the counter electrodes. If the electron coming from the working electrode has the same amount of energy as the electron accepting species at the counter electrode, there is no extractable energy and hence the energy conversion efficiency would be zero. In theory, the maximum attainable energy is the difference between the semiconductor conduction band edge and the redox electrolyte acceptor level, given by the chemical potential of the redox couple. In the dark, to reach equilibrium conditions, metal oxide and the redox electrolyte will undergo electron transfer events until the metal oxide Fermi level (equivalent to the electrochemical potential) equals the electrochemical potential of the redox electrolyte. As an electron is injected into the TiO_2, the extractable energy is not equal to the difference between the conduction band edge and the chemical potential of the redox electrolyte, but instead between the new Fermi level (here referred to as 'new' because an electron was added hence raising the Fermi level) and the chemical potential of the redox electrolyte. Quantitatively, how the Fermi level changes with addition of new electrons is determined by the density of states (DOS) of the semiconductor. The higher the DOS at each energy level, the more electrons will have to be injected to raise the Fermi level and hence achieve a higher potential difference to extract more energy. In a DSSC, as the concentration of electrons is increasing and the Fermi level is rising, equilibrium is reached where the Fermi level stays constant. This equilibrium is established when equal amounts of electrons are lost per unit time to recombination as are generated from light absorption and injection. If no electrons are allowed to escape through the external circuit, the solar cell is in the open circuit conditions and the potential difference can be measured with a voltmeter. This voltage difference is called the open circuit voltage, V_{OC}. If an electron is allowed to travel from the working electrode to the counter electrode, the amount of energy extractable as work per electron is given by this voltage difference. However, that is true only in theory, as in reality there is an additional property, called the fill factor (FF), which determines

how much power is actually generated at the maximum power point on a current-voltage (JV) curve. In essence, if the device would be infinitely thin, with no resistance at the contacts, the maximum power point would be almost equal to the V_{OC} times the J_{SC}. However, during electron transport towards the working electrode, some electrons recombine with the redox electrolyte or photooxidized dyes before reaching the electrode and hence reduce the amount of electrons and consequently the Fermi level inside the semiconductor. This recombination is one of the many factors that influence the FF. The fill factor also depends on all the contact resistances, amount of overpotential required at the counter electrode to facilitate fast electron transfer to the redox couple and the efficiency of dye regeneration relative to recombination to the photooxidized dye.

In the early 2000s it was a well-established (mis)understanding that the injection kinetics are faster than 100 fs and therefore have 100% yield. As early as 2003, Gratzel et al., have been claiming 100% femtosecond injection, which occurs "8 orders of magnitude faster than any other decay channel" even without giving a citation for the claim.[17] Such claims directed researchers' attention away from studying injection and testing dyes or electrolyte components which increase the injection yield. Thanks to the work of Durrant [18, 19], the issue of sub-unity injection yield picked up pace. The current thesis was inspired by the availability of many different conflicting reports and interpretations of the injection yields and kinetics in the literature published in the past decade. The work done during the current PhD and detailed in this thesis proves that injection is a complex process requiring careful consideration if the power conversion efficiency of DSSCs is to be advanced further.

Literature review

This section critically reviews the literature on experimental results and their interpretation relating to electron injection in dye-sensitized solar cells. The view expressed in this section by the author is that up until very recently, it was hard to make definite conclusions about the scope and the scale of electron injection dynamics in different DSSC-based samples from the sum of all the papers. This section will detail both: good points that were made by others as well as errors that were made in the literature.

Several papers describing electron injection measured in the nanosecond to microsecond regime have been published before ultrafast spectroscopy was utilized.[20, 21] Photoinduced heterogeneous interfacial charge transfer from a metal-organic chromophore into a nanocrystalline TiO_2 occurring at ultrafast timescales was first reported to be sub 10 ps in 1990.[22] Later, ultrafast,

on the order of 100 fs was reported by several other groups.[23-25] Ruthenium-based dye N3 sensitized TiO_2 films in air were excited at 605 nm (pulse intensity 0.4 mJ/cm^2) and probed at 500 – 900 nm.[23] Sample of a dye-sensitized ZrO_2 was used as a non-injecting reference. The biphasic kinetics observed exhibited a 50% < 150 fs and 50% ~1.5 ps components. In the following years, the same authors and several other research groups, namely of Willig, Heilweil, Lian, Kallioinen and later Sundstrom, Furube and McCusker observed similar ultrafast injection kinetics.[25-37] Experimental conditions in these reports included ultra-high vacuum, air and inert solvents. The transient absorption spectroscopy instrumentation was extended to not only visible-NIR spectrum, where excited dye, oxidized dye and electrons in TiO_2 absorb, but to mid-IR as well (1800-2400 cm^{-1}), where mostly injected electrons in metal oxide and to some extent, dye molecular vibrations, absorb. Different chromophores, based on coumarin or porphyrin frameworks were also investigated. In all cases, injection dynamics varied with different experimental conditions and setups, but retained a biphasic structure, with the < 100 fs component accounting for 40 - 84% of the rise. Ultrafast TAS was recorded on samples with varying applied electrical potential as well as in the presence of lithium ions.[38] Both, applied electrical bias and presence of lithium ions were found to strongly influence the electron transfer kinetics. Addition of lithium ions resulted in a 7-fold decrease in injection half-time, while application of electrical potential of -0.7 V vs Ag/AgCl electrode retarded the injection dynamics 25-fold, with appearance of a multi-exponential component of > 60 ps. Slower injection component, on the order of 190 ps was observed for a dye N719, which is very similar to the dye N3. N719 is a doubly deprotonated N3 dye.[39] At this point it became apparent that the injection kinetics are inherently at least biphasic, with the proportion and lifetimes of the components strongly dependent on the experimental conditions. Kallioinen et al published a report on N3/TiO_2 system, where different experimental conditions were compared.[40] Sundstrom used ultrafast TAS to conclude that the ultrafast component is due to vibronically non-thermalized singlet excited state, while the slower components proceed from the thermalized triplet excited state.[28] Similar conclusions were reached by Kuciauskas et al, who studied ruthenium and osmium bipyridyl complexes on TiO_2. The ultrafast component was lower for the osmium complexes, consistent with an expected faster inter-system crossing due to osmium being a heavier atom than ruthenium. Injection kinetics of the same dyes on the other metal oxides, namely ZnO, SnO_2, In_2O_3 and Nb_2O_5 were also studied.[27, 41-43] Compared to TiO_2, electron transfer dynamics were not quantitatively different, but other oxides exhibited a higher proportion of injection occurring in the slower picosecond regime. A small fraction of injection was observed even at > 1 ns timescale. The more precise determination of the lifetimes and proportions of the slower injection components in all

cases were hampered experimentally by the length of the delay line, which was usually only up to 1 ns.

Electron transfer into ZnO was attributed to be ultrafast by Furube et al, with the slower component attributed to relaxation of an intermediate formed at the surface after initial electron relaxation.[43] Similar conclusions were reached recently by Lian's group, who studied Coumarin 343 dye on TiO_2, SnO_2, and ZnO. Monitoring excited state decay of a Coumarin dye in the visible and also probing appearance of free conduction band electrons in the mid-IR, it was concluded that neither tin nor titanium dioxides form long-lived interface bound charge separated pairs.[44] ZnO did show a formation of an interface bound state, which decayed with a lifetime of 12 ps. The assignment of such a state is, however, very tricky, because it is almost impossible to distinguish it from the dye excited state. Other researchers attribute the slower injection on ZnO to be due to lower density of states in the conduction band, which is composed mostly of s and p orbitals, in contrast to d-band, which has much higher acceptor DOS in TiO_2.[41] This conclusion is consistent with a Marcus electron transfer model, where reduced acceptor DOS results in a slower transfer rate.[45] Ultrafast injection accompanied with slower injection components have also been observed for rhenium complexes. Some of them, with longer, insulating non-conjugated binding groups, exhibited close to 1 ns injection.[46] In another study, both rhenium and ruthenium complexes with phosphonic acid anchoring groups were compared to carboxylic acid containing complexes. Phosphonic acid groups were found to give faster injection kinetics in the picosecond regime for both complexes, however carboxylic acid bearing ruthenium complex had a higher proportion of ultrafast (< 100 fs) injection component.[47]

Excitation wavelength dependent injection kinetics in acidic solution and in inert organic solvents were conducted by Lian's group.[48] It was found that relative injection yield did not change with varying excitation energy, but the proportion of ultrafast and picosecond components changed, with the ultrafast component accounting for smaller fraction of injection at lower energy photons. The triplet lifetime of the dye studied was 20 ns, therefore a higher proportion of picosecond component, as long as it is much faster than excited state relaxation, does not influence the injection yield. An alternative, non-ultrafast technique for probing injection yield was developed, using thin film actinometers.[49] However, the technique is flawed, as at the time of publication, it did not take into account the Stark effect, which severely complicates analysis. In addition to bleaching of the ground state absorption of the dye, there is another negative component due to injected electrons after optical excitation, known as the Stark effect, which is difficult to quantify and account for.[50]

TiO_2 nanoparticle size dependent injection yields were studied by both time-resolved microwave conductivity [51] and optical TAS.[52] Interestingly, injection yield was found to decrease on

particles bigger than 30 nm, with particles of ~300 nm having only 50% relative injection efficiency compared to 20 nm particles. Larger particles did not exhibit deep trapping effects, which were assumed to occur in 20 nm particles, because of increased microwave conductivity signal upon higher light illumination. Another interesting effect is observed when different pump intensities are employed. At higher pump intensity, a decay of the transient signal at early times (few picoseconds) is observed instead of an increase, which is observed at lower light intensity.[40] An even higher decay is observed when samples are held stationary (i.e. not translated to avoid saturation). A possible explanation could be that the decay becomes faster due to increasing recombination rate [53] or faster electron diffusion away from the probe area at higher number of electrons per particle. At high light intensities, experiments suffer from many uncertainties, as will be shown in later chapters.

The nature of the slower component of electron injection was investigated by several groups. Durrant and co-workers attributed it to local inhomogeneities in excited state energy of the dye compared to an exponential density of states of TiO_2 conduction band.[54] Lian's group attributed it to different electronic couplings of the dyes to TiO_2 surface due to different modes of binding.[48] Using time resolved absorption anisotropy measurements, Sundstrom et al., attributed the slower picosecond component of electron injection to be limited by inter-ligand charge transfer on the chromophore.[55] Another report attributed the slow component of electron injection to dye aggregates on the surface of TiO_2, with electron transfer kinetics slowed down due to increased distance.[56] No aggregation was expected in that study, as dyes were purified and TiO_2 film exposure to dye solution was carefully controlled. However, a single probe wavelength was used at which the excited state is known to absorb as well, invalidating the conclusions of the paper. Attempting to reproduce the experiment, different conclusions were reached by another group.[57] Although similar dye concentration and exposure times were used, they still observed slower triplet injection. Unexpectedly, quenching of electron injection was observed when a higher concentration of the dye solution was used. However, authors used a narrow range of wavelengths in the visible, which from previous studies are known to be hard to interpret due to overlap of three different signals: oxidized dye, excited state of the dye and electrons in the TiO_2 conduction band. This considerable overlap of absorption is further exemplified by Du et al., where a signal in the visible spectrum shows no change in the picosecond timescale, but a significant decrease in excited state absorption is observed in the near-IR region.[52]

Durrant et al. were the first to measure ultrafast TAS on fully operational solar cells. By subtracting the excited state absorption in the visible region of a reference dye-sensitized ZrO_2 sample, injection was attributed to occur only on the longer > 100 ps time scale.[18] This is based on the assumption

that absorption at ~ 800 nm of a dye-sensitized TiO_2 sample is initially, that is, after roughly 100 ps, solely due to the excited state of the dye, discounting any amount of the absorption by the oxidized dye. This interpretation simplifies quantification of electron injection using time resolved single photon counting (SPC) technique.[19] As will be seen in later chapters, this assumption is wrong and more care must be taken to arrive at meaningful injection yields when interpreting SPC measurements. Another technique, based on incident photon to current conversion efficiency measurements coupled to a full model of the operating cell, was compared to the findings of the TCSPC method, in close agreement.[58] By varying the electrolyte components in order to shift the conduction band edge up or down, the short circuit current was also found to correlate (although not perfectly) with the TCSPC method.[59] For some devices, the short circuit current differed by ~25%, although injection yields obtained from TCSPC measurements were identical. Similar discrepancies between inferred injection yield and actual short circuit currents have been observed in ionic liquid based solar cells.[60] Although qualitatively the TCSPC method can indicate a problem with injection, TCSPC is not fully quantitative. When there is a much faster component to injection, it enhances this discrepancy: the reported TCSPC measurement only probes the amount of luminescence left 200 ps (this number depends on the instrument response time) after excitation. It is possible that the injection yield at ultrafast timescales is affected by a different amount than the injection at > 200 ps timescale. Such a discrepancy could cause inaccuracies in the overall injection yields obtained by TCSPC. A recent study, utilizing time resolved terahertz spectroscopy showed that indeed there is an ultrafast component (> 40%) even in fully operational cells.[61] The slower component exhibited stretched exponential character, with a lifetime of ~50 ps and a 0.7 stretching factor, tail of which would show up on the SPC measurements. Research papers studying devices in redox electrolytes instead of metal oxide bound dyes in inert solvents or in vacuum picked up since 2011. In addition to ruthenium dyes, new high-efficiency organic dyes were measured and interest in the injection kinetics increased. One such dye, D149, was shown to have injection kinetics with a lifetime of 2-3 ps when on TiO_2, probed via ultrafast fluorescence decay.[62] Injection dynamics probed by both ultrafast TAS and time resolved fluorescence were studied for a porphyrin dye. These authors found non-injecting dyes coexisting with injecting dyes on TiO_2, an effect attributed to electron injection inhomogeneity.[63] As will be seen in Chapter 6, such claims are very hard to prove experimentally and the study suffers from the short length of the delay line, which extends only up to 1 ns. In addition, authors used dye ground state bleaching decay as one of the probe signals, which is unreliable due to strong Stark effects present in DSSCs.

Another recent paper studied very simple donor-accept organic systems adsorbed on TiO_2.[64] As for Ru-based dyes, a much slower > 50 ps, non-exponential injection component was observed.

Authors attributed the slower injection component to the trap states below the conduction band edge of TiO_2, which then undergo fast recombination to restore the ground state of the dye. Another extensive review of porphyrins on TiO_2 argued for the presence of non-injecting dyes on TiO_2, which become injecting after "light soaking". Ultrafast TAS at 3440 nm probe wavelength in addition to APCE measurements were used to reach this conclusion, however no photoluminescence data were presented.[65] Another study involving organic dyes reported close to 100% injection efficiency in a number of electrolytes. Interestingly, V_{OC} varied from 400 to 550 meV, and injection efficiency was still estimated to be close to 100%. Unfortunately the authors did not produce any further evidence from non-spectroscopic methods, i.e. APCE or simple JV curves, hence the conclusion is not proven. In addition, the highest V_{OC} in the paper reported was 200 meV lower than the best performance reported in the literature at 750 meV, implying the electrolytes used might have been too acidic to start with.[64, 66] An interesting observation was the increase in injection rate with increasing optical excitation energy, which implies the injection proceeded faster from a non-thermalized, vibrationally excited state. Time-resolved terahertz spectroscopy was utilized to study electron injection of both metal-free and metal-containing porphyrins adsorbed on either TiO_2 or SnO_2. In contrast to the non-injecting porphyrin dye review paper, biphasic injection over broad timescales, with lifetimes spanning up to 200 ps were observed.[67] Another paper, comparing D149 on TiO_2 and on ZnO using ultrafast spectroscopy recently came out.[68] Authors did a lot of extensive ultrafast experiments, however an unfortunate shortcoming renders the paper inconclusive: an electrolyte with a pyridine derivative was used, which is known to desorb the D149 dye from the metal oxide. This is one of many examples of the flawed publications on electron injection into metal oxides from photoexcited dyes.

A structure/function relationship study of phthalocyanines on metal oxides was recently reported.[69] Here, in operational devices, authors observed multi-exponential, but close to ultrafast injection kinetics, going from femtoseconds to a few picoseconds. Instead of attributing injection losses to non-injecting dyes, authors concluded that back electron-transfer was mostly responsible for reduced photocurrent generation. Interestingly, the back electron transfer rates were on the order of hundreds of picoseconds with at least 40% component having a decay lifetime of 100 ps. This is in direct contradiction with observed IPCE's of > 60% for the devices. In the ultrafast TAS, several slow decay components were observed which were attributed to back electron transfers. In light of the IPCE data, however, it could have been misinterpreted, as the decays might have been due to electron injection. This interpretation has been reported before and was not mentioned in the Sharma publication.[70] The lifetimes of the excited phthalocyanines are on the order of several nanoseconds, hence the observed signals could have also been attributable to the

decay of the phthalocyanine excited states. A recent publication from the Gratzel group[71] attributed more than 75% of injection to ultrafast < 100 fs processes, while the rest of the injection to the aggregated dyes. The paper had some serious flaws, where they claimed they used a "performance optimized device" when in reality it had 120 meV less V_{OC} than devices with the same components in the literature. In addition, the authors repeated their mistake from over 8 years ago and probed injection at a single wavelength, which has been shown several times to be inappropriate for measuring injection.[52]

Structure of the Thesis

In this thesis, the vast differences in the observed electron injection kinetics as reported in the literature will be, in some cases, reproduced and explained. Operational, performance optimized devices will be measured and fully analyzed over a very broad wavelength range (800 – 8000 nm). Injection yield will be derived for several ruthenium polypyridyl dyes and interpreted in light of the newly obtained spectroscopic data. The current work is hence structured as follows. In Chapter 2, experimental methods and equipment are introduced. All the sources of materials and device manufacturing techniques are explained in full detail. In Chapter 3, a theoretical explanation of the experimental techniques is given in addition to the methods used for data analysis and interpretation. Reliability of some of the methods is reviewed. A few sections are dedicated for detailing the various phenomena that occur on ultrafast timescales due to optical effects in the equipment and between ultrafast light pulses. Mathematical models are briefly introduced and appropriate references indicated. In Chapter 4, the very basic ground work for ultrafast transient absorption spectroscopy is reported. Various experimental conditions are tested and shown to not influence, or in some cases influence, the spectroscopic findings of the dye-sensitized solar cells. Initial results are presented, where electron injection is shown to be clearly multi-phase with very broad kinetics, when measured in efficiency-optimized devices. All the spectroscopy is done in the mid-IR region. Chapter 5 complements Chapter 4 with additional near-IR and visible ultrafast TAS. Several more materials are introduced into the DSSCs and studied. It is shown that the mid-IR data is consistent with the near-IR findings and that the spectra in the near-IR is much more complicated and experimental-condition dependent than the one in Chapter 4. Finally, performance data, IPCE data and luminescence data are presented in Chapter 6 which enhances and finalizes the interpretations given in the previous two chapters. Remaining mysteries that cloud the electron injection are indicated and summarized. Chapter 7 concludes the entire thesis and indicates future work. At the end, full reference details as used in the thesis are provided.

Chapter 2. Experimental methods & techniques

Introduction

In this Chapter, details pertaining to the experimental part of the PhD thesis are given. The sources of materials and their purity are provided. Experimental methods and experimental setups are described.

Solar cell materials: dye solution, TiO_2 paste, ZrO_2 paste, electrolytes, electrodes

The materials used throughout the PhD were sourced as follows. TiO_2 paste 18-NRT, which gives 6.8 µm thick TiO_2 devices, was purchased from Dyesol. Another TiO_2 paste, which gives 4.3 µm thick films was prepared in-house by Dr. Xiaoe Li following a published recipe.[72]

Different batches of dyes N3, T51, Z907 and N719 were obtained from Michael Graetzel's group in EPFL or bought from Sigma-Aldrich and Dyesol. The dyes D149 and C106 were sourced from Dr. Emilio Palomares group in Valencia, Spain.

The electrolytes were prepared in our laboratories. The materials were sourced from different locations. High purity 3-methoxypropionitrile (MPN) was obtained from "Dixie Chemical" and "Tikslioji Sinteze". The latter company used a complicated procedure of chromatographic filtering and distillation under argon atmosphere to obtain a 99.91% purity. Acetonitrile, iodine, guanidinium tiocyanate (GuSCN, >99%), benzimidazole (BzI), chenodeoxycholic acid (cheno), ethanol, isopropanol, acetone, dichloromethane, lithium iodide, titanium isopropoxide, 2,4-pentanedione, powder of titanium chloride complex with tetrahydrofuran and chloroplatinic acid were bought from Sigma-Aldrich and were HPLC grade. 1-propyl-3-methyl imidazolium iodide (PMII, 98%) and tert-butyl alcohol (TBA, 95%) were bought from "AlfaAesar".

Glass substrates with a thin film of fluorine doped tin oxide (FTO), which had 15 ohms cm^{-2}, acting as a transparent conducting electrode, were bought from "Hartford Glass Co. Inc." and "Pilkington glass".

Surlyn ionomer gaskets (Surlyn 1472 polymer) for sealing solar cells were bought from DuPont, but were sent to us from EPFL.

Distilled water was prepared with a Milli-Q water distillation equipment (Millipore Corp, 18.2 MΩ cm at 25 ^{o}C).

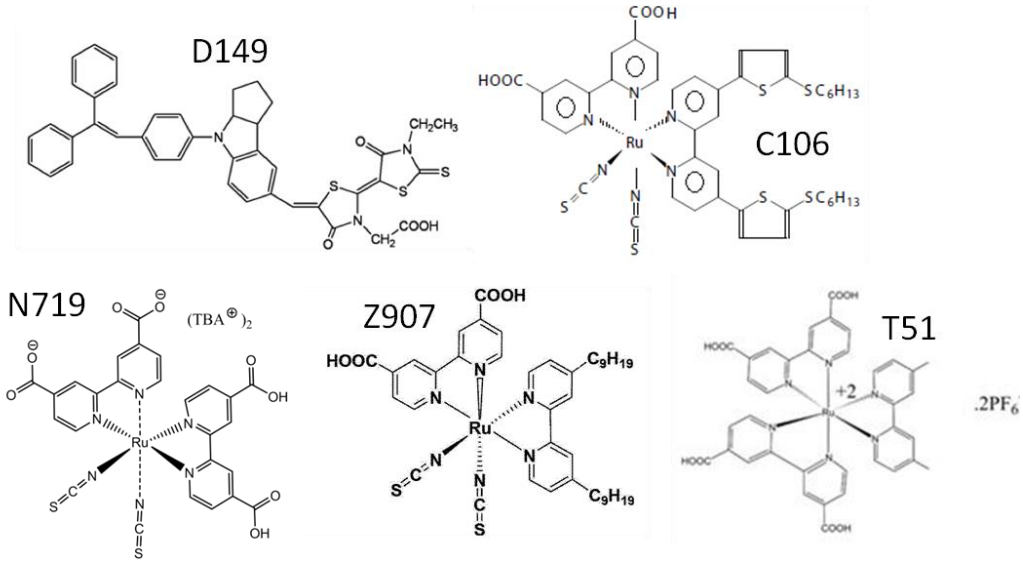


Figure 2.1. Dye chemical structures. These were used throughout the thesis. Note that N3 dye is the same as the N719 dye, except two H^+ cations replace the two tert-butyl ammonia (TBA^+) counterions.

Solar Cell Preparation.

FTO cleaning. To manufacture a working solar cell, the following procedures were used. The FTO glass was rinsed with running water, soap, distilled water and acetone, in that order. These substrates were then heated in air for 30 minutes at 450 ^oC, with the FTO facing up. In most cases, while still at 450 ^oC, a spray layer of TiO_2 was added onto the FTO to form a hole blocking layer.

Spray Solution. The solution of titanium acetoacetonate for spraying was prepared by mixing 0.6 mL of titanium isopropoxide with 0.4 mL of 2,4-pentanedione. After 5 minutes, 9 mL of EtOH (99.7% pure) was added. Approximately 4-5 times with 30 second intervals, this solution was sprayed using compressed air onto the FTO glass. The films were left at 450 ^oC to sinter. This procedure forms 30-60 nm thick TiO_2 layer on top of the FTO.

Titania film deposition. After the FTO has cooled to roughly room temperature, one layer of the TiO_2 particles (~7 µm) were deposited onto the FTO substrate by tape casting (also known as "doctor blading"). This was done using 55 µm thick scotch tape for the blading support. After leaving these bladed films in air for 30 minutes to allow solvent evaporation, the TiO_2 layers were heated to 450 °C in air for 30 min. The 450 ^oC temperature is reached gradually, in an interval of 1 hour to avoid cracking of the films. An additional ~1 nm TiO_2 layer over each particle was added by soaking the TiO_2 films in 40 mM $TiCl_4$:THF complex solution in water, cooled to 5 ^oC. Films immersed in this solution are then put into a fan-operated oven at 70 °C for 30 min. Note that the solution never actually reaches the 70 ^oC. After 30 minutes, the films are rinsed with water. Straight after the water

rinse, the films are rinsed with isopropanol. If the latter step is not done, the films may crack during sintering. The TiO_2 films are then reheated to 450 °C after the $TiCl_4$ treatment. The substrates are then cut into 2.5 x 3.5 cm strips. The TiO_2 active area is scraped away with a thin piece of glass to leave an active cell area of 1 cm^2, unless indicated otherwise. After scraping, the electrodes are rinsed with acetone and reheated to 450 ^oC. The films are allowed to cool to ~100 °C and then immersed in the dye solution for 12-14 h. TiO_2 films were dyed in 0.3 mM N719 solution in 1:1 tert-butanol and acetonitrile for 12-14 hours. The 0.15 mM C106 solution also contained 2 mM chenodeoxycholic acid in 9/9/2 (by volume) acetonitrile/tert-butanol/dimethylsulfoxide. After the dye solution, the films are rinsed with acetonitrile and the TiO_2 film substrate is sandwiched with a counter electrode with a 25 μm thick surlyn gasket. The counter electrode is an FTO substrate, which has two small holes drilled with a distance of roughly 1.4 cm away from each other, placed in the opposing corners of the 1 cm^2 TiO_2 active area. After rinsing the substrate is covered with a thin film of chloroplatinic acid solution (5 mM in isopropanol) and heated to 400 ^oC for 10 minutes. Note that no platinum is added on the substrate electrode which contains the TiO_2. This forms a hardly visually perceptible layer of platinum on the FTO substrate. An electrolyte is then injected through the hole in the counter electrode, which is drawn in by capillary forces. The holes are sealed with surlyn ionomer and an additional microscopic glass slide is glued on top of the surlyn to reduce light reflection.

Several electrolytes were used throughout the thesis. The DS electrolyte was composed of 0.8 M 1-propyl-3-methyl imidazolium iodide, 50 mM I_2, 50 mM guanidinium thiocyanate and 0.3 M benzimidazole in 3-methoxypropionitrile. No benzimidazole was present in electrolytes used for the D149 dyes. All materials were used as supplied. The Li electrolyte contained only 0.8 M of 0.8 M 1-propyl-3-methyl imidazolium iodide, 50 mM I_2 and 0.5 M of lithium iodide in MPN.

Finally, on both electrodes, to ensure good electrical contact, silver paste was deposited on the TiO_2-free FTO surfaces, carefully avoiding any short circuiting of the electrodes.

Sapphire and CaF_2 devices manufacturing

Sapphire substrates with a diameter of 2.5 cm and a thickness of 0.5 mm and CaF_2 substrates of diameter 2.5 cm and 5 mm thick were purchased from “CRYSTRAN UK”. The rinsing and spray layer deposition methods were identical to those for DSSC devices. It is very important to note that without the spray layer, the deposited TiO_2 paste delaminates. The dyeing and $TiCl_4$ procedures were identical as for solar cells. During the sandwiching step, two small holes are cut into the surlyn gasket, which will allow electrolyte injection. Alternatively, two holes were drilled at a jeweller’s

store in the sapphire substrates to have identical electrolyte injection as for the solar cells. Sapphire is transparent enough for spectroscopy up to 5500 nm while CaF_2 is transparent up to 10000 nm.

Film thickness measurements

The film thicknesses were measured using a profilometer (AlphaStep 200, Tencor Instruments). The scan would start at the TiO_2 free substrate and then move over the TiO_2 area. This would be done from all four edges of the TiO_2 to ensure the film thickness homogeneity.

Temperature control equipment

For controlling the device temperatures for both photocurrent measurements and the TCSPC, a Lauda RE104 water cooling bath was used. The devices were carefully interfaced to a metal substrate, touching the counter electrode side using a thermoconductive paste, to ensure good thermal contact. The metal substrate was then cooled or heated up with water which flowed into the metallic container. Two PT1000 (from RS) thermistors were attached at the counter and working electrodes of the device and an average of the two temperatures was taken.

Current-voltage equipment

Current-voltage (JV) measurements were performed under simulated 1 sun illumination (AM 1.5G). A 150 W xenon lamp fitted with an AM 1.5G filter were used as a light source. Calibration of the light source with a silicon photodiode in the same spot as the sample was done before measurements, to achieve roughly 100 mW cm^{-2}, equivalent to light intensity of 1 sun. During the measurement, the applied voltage scan started at 0 V, then slowly, at a speed of 0.05 V s^{-1}, is increased to 1 V and then to -1 V and then back to finish at 0 V. The data were recorded using a Keithley 2400 sourcemeter. The entire measurement is automated via a computer, software for which was written by Dr. Assaf Anderson.

UV-Vis absorption equipment

All the UV-Vis absorption spectra were recorded using a Thermo Genesys 10 spectrometer. Before each measurement, the equipment was allowed to warm up for 30 minutes, was zeroed down for background absorption and the samples were measured. Background noise was subtracted by running a measurement without a sample in place.

IPCE equipment

Incident photon conversion efficiency measurements were recorded using the following equipment and procedure. A 100 W tungsten halogen lamp was allowed to warm up for 30 minutes (Bentham IL1 with Bentham 605 stabilized current power supply). A single wavelength from the halogen lamp was selected using a computer controlled monochromator fitted with a stepper motor (Bentham M300, 300 mm focal length, slit width 3.7 nm, 1800 lines/m grating). The photon flux of light incident on the samples was calibrated using a UV enhanced silicon photodiode (Thorlabs). A 580 nm long-pass glass filter was inserted between the beam and the sample when light wavelengths were longer than 620 nm to remove second-order diffraction. Photocurrents were measured using a Keithley 2400 source meter. Measurement duration for a given wavelength was usually long enough for the current to stabilize, for approximately 10 seconds. An average of the generated photocurrent over 20 seconds was recorded. Measurements were made at 10 nm wavelength intervals between 450 and 900 nm. The cells were illuminated from either the TiO_2 (working electrode) or the Pt (counter electrode) sides. The illumination was chopped using a computer controlled shutter and the difference in stabilized short circuit photocurrents used to calculate the IPCE. Experiments with bias light used an array of eight white light emitting diodes (Luxeon star/O, white LXHL_NWE8) driven by a TTL QL564 direct current power supply. The bias light was tuned to approximately 10% of 1 sun AM 1.5G illumination intensity and was ensured to be generating a constant amount of current, without any drift, during the entire experiment. Bias illumination was from the same direction as the monochromatic light. The software for controlling the equipment and collecting the data was written by Dr. Assaf Anderson.

TCSPC equipment

The time-correlated single photon counting equipment was a Jobin Yvon IBH Fluorocube laser system. The optical pump was a 467 nm excitation (1 MHz repetition rate, 80 µW cm^{-2} average intensity, 200 ps FWHM instrument response), with one 650 nm and one 695 nm high-pass filters inserted before the light detection to avoid any stray excitation laser light getting into the detector. The data was collected with the software provided by Jobin Yvon and saved as .csv files for later analysis. Two data collection modes were used: either recording the luminescence for a fixed period of time, or recording until a specific number of photon counts at the peak wavelength were reached. The exact details are indicated where TCSPC data is presented. After positioning the devices in the instrument as to obtain the highest number of photon counts per second, the device is not moved until the entire experiment is done. An instrument response function is obtained by tuning the monochromator of the photon collector close to the excitation wavelength with two high-pass filters

below the excitation wavelength present, to obtain the same travel path of all the photons. Prompt function thus collected can then be used for fitting with reconvolution, which is described in the next chapter. The instrument response function determination method just described suffers from the fact that photons of different wavelength, and in particular the photoelectrons they generate in the detector, do not travel the exact same path. This may lead to colour effects when comparing scattered and emitted light and may give sizable differences around time zero, depending on the detector used. Ideally, the same wavelength for recording the instrument response should be used as for the excitation.

Ultrafast transient absorption spectroscopy in the mid-IR

The output (1 kHz, 800 nm) of a Ti:Sapphire regenerative amplifier (Spitfire PRO, Spectra Physics, 4W, 70 fs) was divided between two optical parametric amplifiers (TOPAS, Light Conversion). One of the parametric amplifiers was equipped with a non-collinear difference frequency generation module that enabled wavelength tuning in the mid-IR region used for the probe light. The other OPA used additional frequency mixing stages to generate near-IR and visible light pulses used as pump pulses for optical sample excitation.

The mid-IR probe beam was attenuated by neutral density filters and split in two to produce signal and reference beams. Signal beam was focused onto the sample with off-axis parabolic mirror and further with a focussing lens into a spot of roughly 100 µm diameter (full width half maximum, FWHM), depending on particular experiment. Transmitted signal and reference beams were directed to specially modified spectrometers (Triax190, Horiba) with mercury cadmium telluride (MCT, bought from "Infrared Associates") detectors (128 pixel arrays, Infrared Systems) attached to them. Data was collected and saved on a computer via a FPAS data acquisition systems device (Infrared Systems Development Corp). There were three such detectors, with wavelength spacing of 2.55 nm, 4.21 nm and 9.18 nm, depending on the wavelength range used. Visible pump beam (~300 fs timewidth) was modulated with an optical chopper (500 Hz, half of laser repetition rate) and its timing relative to probe pulse was changed with a delay line which allowed up to 1.5 ns delay relative to the pump pulse. Pump beam intensity was adjusted using reflective neutral density filters and it was focused on the sample to at least ~300 µm spot FWHM. The pump polarization was set at the magic angle relative to the probe beam, at 54.7^{o}. Pump-on minus pump-off difference spectra were obtained by shot-to-shot referencing and on-the-fly signal discrimination at 3 standard deviations to reject outliers.

During most experiments, the samples were not translated. Where samples were translated, a bespoke sample translator was used to move the samples in Lissajous patterns at an average speed of 50 μm ms^{-1}.

VIS/Near-IR ultrafast TAS

Samples were excited with a pump light at 580 nm over a very broad range of light intensities (accurate energies indicated in the text where appropriate). The pump light was generated by a commercial optical parametric amplifier TOPAS (Light conversion) pumped by a 1 kHz, 800 nm, 2.5 W, 100 fs timewidth, Solstice Ti:Sapphire regenerative amplifier (Newport Ltd.). The output of the Solstice laser was split in two. One of the 800 nm beams was used to generate a broadband pulse in a sapphire crystal (830−1450 nm). The broadband pulse follows the pump laser excitation. A HELIOS (Ultrafast systems) transient absorption spectrometer was used for recording the dynamics of the transient absorption spectra, by delaying the pump pulse with a motorized delay line, capable of delay times up to 6.5 ns. The instrument response time was roughly 200 fs. The pump pulse frequency was 500 Hz. Absorption at each time delay was recorded for 5 s (2500 pulses), and this averaging was repeated four times, scanning in both directions: starting from time 0 to 6.5 ns delay; then from 6.5 ns delay to time zero, repeated twice. The pump pulse was unfocused and had a FWHM of roughly 3 mm while the probe pulse was focused to an FWHM of < 400 μm. The pump pulse energy was measured through several diameter pinholes, at 0.15, 0.3 and 0.5 mm. The energy per pulse per cm^2 was within 5% through all pinholes indicating that the pump pulse is homogeneous within the probe pulse area. The energy per cm^2 with the aid of the pinholes was determined with a very sensitive power meter, capable of recording and averaging pulse energies at 500 Hz repetition rates (obtained from Ophir, PD10-V2).

Chapter 3. Methods and Theory

Introduction

In this chapter, the theoretical details of the experimental techniques and data analysis are discussed. The concepts presented in this chapter are instrumental to reliable analysis of the experimental results and for arriving at correct conclusions. Several experimental techniques are covered in detail. Principles of ultrafast transient absorption spectroscopy (TAS) are explained and in addition, important phenomena such as perturbed free induction decay, probe chirp and cross phase modulation are discussed. Details of data fitting to exponential functions for single photon counting (SPC) experiments are outlined. The sensitivity and reliability of the SPC equipment is provided. For deriving electron injection yields and electron diffusion lengths, IPCE front/back method is briefly introduced and theoretical background is provided.

Ultrafast pump-probe transient absorption spectroscopy

The technique of pump-probe, otherwise known as transient absorption spectroscopy (TAS) was of immense importance to the current work. The basic scheme detailing the working principles of the technique is given in Figure 3.1.

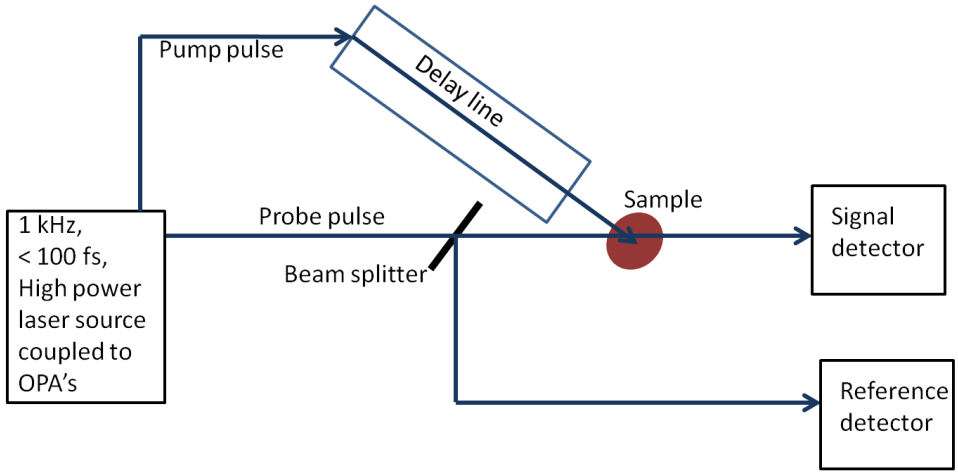


Figure 3.1. Scheme showing the components of a TAS system. Experimental details of the components can be found in Chapter 2.

As indicated in Figure 3.1, both pump and probe pulses have to be generated by the same laser source in order for them to be as synchronized in time as possible. The pump signal optically excites the sample. The probe pulse is partially absorbed by various species in the sample and is then

recorded at the signal detector. The reference detector records the probe beam as it appears without the sample; hence the absorption due to sample can be recorded with good noise rejection. In order to compute a difference spectrum due to excited species in contrast to species present at dark conditions in the sample, two spectra have to be recorded: one with the pump pulse before the probe pulse, and one with just the probe pulse, without the pump. The difference of these two spectra is then the equivalent of only the short-lived transient species present in the sample just after the optical excitation. The delay line is used to delay the pump pulse with respect to the probe pulse, so transient spectra of the sample at varying times after the excitation could be recorded. To enable the calculation of the difference spectra, every second pump pulse is chopped with a frequency of 500 Hz. Hence the probe pulse hits the sample every 1 ms, while the pump pulse hits the sample every 2 ms.

Two femto- to nano- second TAS setups were used throughout the thesis. The working principles remain the same in both cases, except for the probe light wavelengths. The only experimental differences are then in the optical parametric amplifiers used to convert 800 nm laser output to different wavelengths and the detectors used for recording the light intensity.

There are several phenomena which occur around time zero, i.e. when the probe and pump pulses are within hundreds of femtoseconds within each other. These phenomena are very important to understand and are hence discussed in the next sections. The phenomena may appear as ultrafast photophysical events occurring in the sample and that may lead to incorrect interpretations.

Probe chirp

A very well known phenomenon in ultrafast lasers is the chirp. This characteristic of laser signals can be very useful in some contexts, e.g. mapping of potential energy surfaces of molecular systems,[73] but can also be detrimental in ultrafast TAS. When the probe light pulse is a broadband signal, generated in e.g. a sapphire crystal, it possesses a property called “frequency chirp”.[74, 75] The name comes from the way birds chirp, i.e. starting with low (high) frequency tone and sweeping up (down) to finish with a high (low) frequency note. Same applies experimentally for broadband signals in fs-TAS spectroscopy, where the high or low frequencies arrive at the sample first, followed by decreasing or increasing frequencies. The origins of chirp can be several: non-linear optical effects in transparent medium (e.g. sapphire), self-interference of the white light continuum and most simply due to wavelength-dependent refractive indices of the transparent media which are encountered by the broadband probe beam. In the recorded spectrum, it is seen as the rise of an absorption signal on the red or blue side of the spectrum tens or even hundreds of femtoseconds earlier than the same rise on the other end of the spectrum. This may be erroneously interpreted as

spectral developments due to photophysical events. In addition, due to broadband light generation and similar effects which give rise to the chirp, the actual time-width of the light at different frequencies is usually not constant, and hence in the spectra it may appear that at one end of the spectrum the rise/decay of the signal occurs tens of femtoseconds faster/slower than on the other end of the spectrum. It is possible to adjust for this chirping during data analysis, however, it is always sample dependent and it would have not been useful in the context of the present work. Care was taken not to interpret chirp related artefacts as photophysical processes. These effects occurred at < 1 ps over all wavelengths and relative spectral shifts in this range were ignored.

Perturbed free induction decay in vibrational spectroscopy

Visible light absorption of molecules almost always results in some vibrational states getting excited. If the molecules are excited with a coherent light source, in this case a laser, there is a population dephasing time T_2 in which the excited molecules lose any coherence. The perturbed free induction decay (PFID) manifests itself in mid-IR ultrafast spectroscopy at negative delay times if the pump pulse time width is shorter than the T_2 time.[76] The broadband probe pulse excites coherently molecules into vibrational excited states, which then undergo dephasing. If the pump pulse hits the molecules before they are fully dephased, some molecules will undergo stimulated emission in the mid-IR. This stimulated emission will reach the detectors and it will appear as more infrared light got through the sample when the pump pulse was present (even though it hits the sample only after the probe pulse) than without the pump pulse. Hence the PFID shows itself as negative absorption change before time zero, usually around wavelengths where there are infrared absorbing compounds in the sample. This effect was observed in some of the experiments in the mid-IR region, however as it appears just before time zero, it had no impact on the interpretation of experimental data.

Cross-phase modulation

Cross-phase modulation (XPM) is an effect observed in ultrafast pump-probe spectroscopy of samples which can undergo change in the refractive index if a high peak-intensity light enters the medium, e.g. this is observed in liquid-containing samples. It is a non-linear optical effect where two light beams interact. The interaction results in a phase change of one of the beams. In essence, an intense pump beam changes the refractive index of the medium for the second (in this case, the probe) pulse. For the interaction to occur, the pulses have to overlap to some extent inside the measured medium. In ultrafast pump-probe spectroscopy, specifically the one used in this work,

with the FWHM of the light pulses of ~100 fs, it is important approximately up to a 1 ps range around time-zero. The exact effects that would be seen due to XPM can be predicted by solving the coupled non-linear wave equations of the two light pulses. Several references have done this before, with their theoretical predictions confirmed by experimental results. [77, 78] In the work presented here, it is observed around time zero as an ultrafast decrease/increase of absorption change signal and an ultrafast decay, increase/decrease of the same signal. It is important not to confuse such a signal with an electron transfer event. An example of this is given in Figure 3.2.

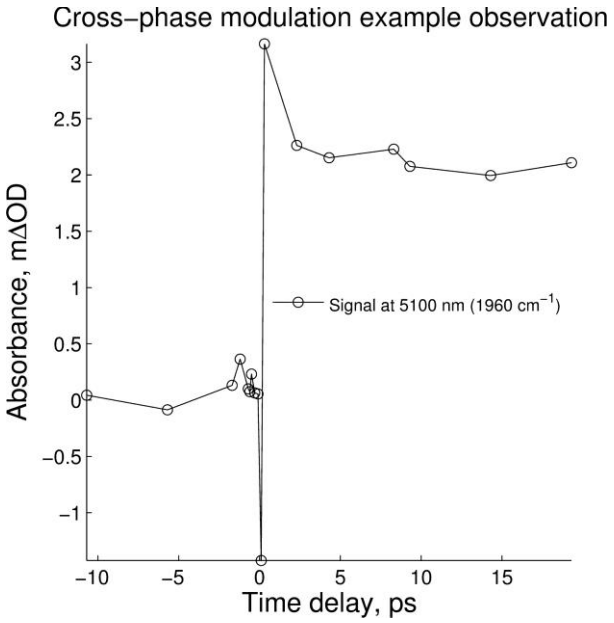


Figure 3.2. An illustration of the cross-phase modulation in ultrafast pump-probe spectroscopy.

The measurement in Figure 3.2 was generated in a typical experiment on N719 dye adsorbed on ZrO_2 deposited on CaF_2 and immersed in an I^-/I_3^- electrolyte. The XPM can be seen around time zero, where a sharp decay and a sharp rise is seen, lasting approximately 500 fs, and later decays in 2 ps to a stable signal, corresponding to the transient absorption of a photoexcited N719 dye at 5100 nm probe wavelength. The relative magnitude of this effect is comparable to that of the actual signal, hence it is important to not misinterpret it as a relevant electron transfer event in the sample.

Time-Correlated Single Photon Counting

The time resolved luminescence decays were recorded with equipment described Chapter 2. In this section, the data analysis and the instrument response are briefly reviewed.

The laser LEDs that were used to excite the samples had a pulse time-width of < 200 ps. This, combined with the electronic response function of the device, requires any data analysis that

obtains time constants (in an exponential decay context) of less than 500 ps to take into account the actual instrument response times. The usual approach in the literature is to obtain a convolution integral, which assumes a Gaussian distribution for the excitation light with a known FWHM and a fitting function, e.g. a single exponential, which describes the actual luminescence decay of the molecule. Here, however, a more empirical approach was taken and the instrument response function was always recorded before or after the luminescence measurement. For fitting the decays, either a stretched exponential or a double/triple exponential function was usually employed. The numerical procedure for obtaining the lifetimes was written in Igor Pro. Firstly, the fit parameters are guessed, the obtained luminescence decay is then reconvoluted with the measured instrument response function and compared (in terms of sum of errors squared) with the actual measured decay. The fit parameters are adjusted and the procedure is repeated until the obtained fits match the experimental data as closely as possible. The numerical formula for discrete convolution can be found in any applied mathematics textbook.[79]

Reliability of the TCSPC equipment

Claims have been made in the literature that an instrument response of < 200 ps enables lifetimes of 60 ps or below to be measured reliably. [19] This claim is challenged in the current section.

Pure erythrosine B was dissolved in water and in methanol.[80] To ensure the solutions are dilute enough, they were diluted further until no difference in the decays were observed. Excitation wavelength was 467 nm and probe wavelength 570 nm, with two long pass filters to cut out any scattered light. Room/solution temperature was ~22.5^{o} C. The fits were obtained with reconvolution using procedures written in Igor Pro and the following graph was obtained, indicated in Figure 3.3.

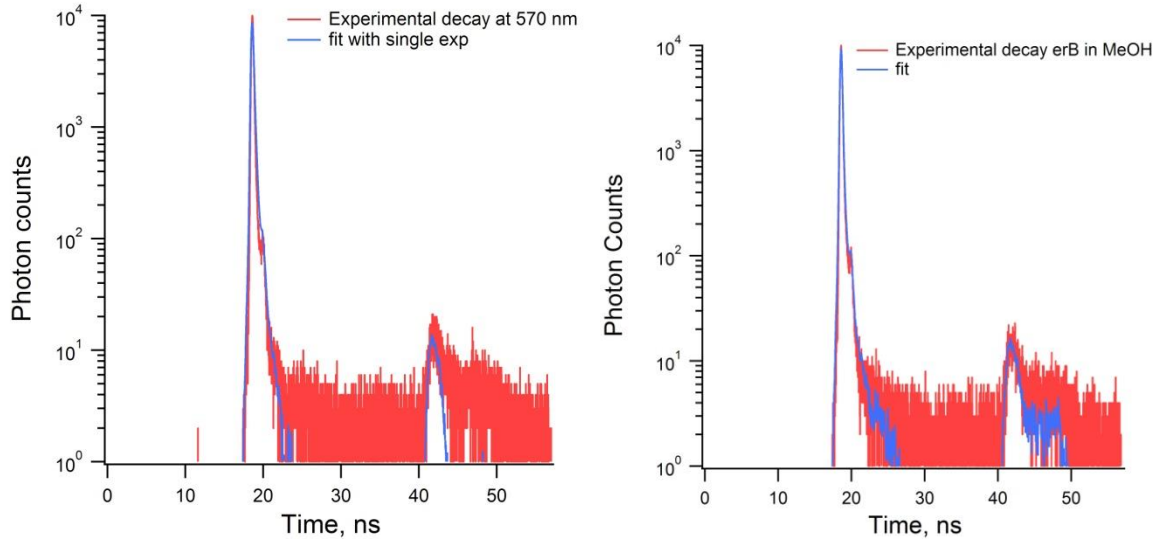


Figure 3.3. Time resolved luminescence decay of a dilute solution of erythrosine B dye in water (left) and methanol (right). Note the logarithmic y-axis. The fit (in blue) is really good in both cases.

The equipment measures time in discrete intervals. The time difference between one channel to the next is 14 ps. The instrument response function can be shifted artificially to obtain a better or worse fit. This could be an advantage to do sometimes, if the IRF is recorded under conditions when light travels a slightly different path from the luminescence measurement. In order to check if time-shifting the prompt made any difference, the prompt was shifted to the right and to the left by 1, 2 and 3 channels and then were refit. Visually, the fits looked almost identical, as in the Figure 3.3. The results are summarized in the Table 3.1 below:

Fit condition	Single exponential lifetime	Chi-squared (total)	Literature value at 20°C, excited at 488-568, probed at 550-580 nm
No artificial shift, as measured	115 ps	26.1e6	89 ps
Shifted prompt to right by 1 channel	98 ps	13.9e6	89 ps
Shifted prompt to right by 2 channels	82 ps	6.2e6	89 ps
Shifted prompt to right by 3 channels	66.5 ps	2.6e6	89 ps
Shifted prompt to left by 1 channel	132 ps	42.8e6	89 ps
Shifted prompt to left by 2 channels	150 ps	63e6	89 ps

Table 3.1. Fit parameters for SPC data recorded of an erythrosine B dye in water.

From the above table, one can see that the sum of errors squared was consistently decreasing with right-shifting of the prompt, and it gave 66.5 ps with a high confidence interval, quite off from the actual 89 ps. This illustrates that the instrument can be accurate and measure lifetimes less than the instrument response (which for the 467 nm light is < 200 ps). However, in practice it is not really possible. These experiments were done in solution, where one has very good control on the path length the photons travel, in contrast to solid state samples. Hence one would have to be very careful and cautious when measuring devices with lifetimes lower or around the instrument response.

Further support for the care required when measuring lifetimes close to instrument response was obtained when measuring erythrosine B in MeOH. The graph of the decays is on the right side of Figure 3.3. Table 3.2 provides the parameters obtained from the fitting function.

Fit condition	Single exponential lifetime	Chi-squared (total)	Literature value at 20^{o}C, excited at 488-568, probed at 550-580 nm
No artificial shift, as measured	471 ps	28e6	470 ps
Shifted prompt to right by 1 channel	447 ps	15e6	470 ps
Shifted prompt to right by 2 channels	424 ps	8.4e6	470 ps
Shifted prompt to right by 3 channels	402 ps	9e6	470 ps
Shifted prompt to left by 1 channel	496 ps	48e6	470 ps
Shifted prompt to left by 2 channels	521 ps	74e6	470 ps
WITHOUT RECONVOLUTION	517 ps	1e6	470 ps

Table 3.2. Fitting parameters of SPC data of erythrosine B in methanol solution.

From the table above, reconvolution was clearly required even at lifetimes twice higher than the instrument response. In addition, experimental skill of recording correct instrument response function was more important in obtaining the literature decay lifetime than using the prompt shift as a free parameter in the numerical procedures. In the remainder of the thesis, the prompt was not shifted when fitting the data to exponential functions and extra care was taken when setting up the SPC experiments. The instrument response was hence concluded to be around 200 ps and any lifetimes measured to be under that number are not deemed reliably accurate.

IPCE front/back method

The incident photon to current conversion efficiencies obtained by measuring the devices from both front and back electrodes and then obtaining the correct diffusion and injection rates is quite mathematically involving. Barnes et al., wrote excellent papers giving all the details required to do such analysis.[58] To describe the problem briefly, electrons in TiO_2 under a constant flux of light and under short circuit conditions undergo diffusion, recombination and injection. In one dimension, such processes are well described by the diffusion partial differential equation:

$$D_0 \frac{\partial^2 n_c(x)}{\partial x^2} - \frac{n_c(x) - n_{c0}}{\tau} + \eta_{inj} G(x) = 0$$

Here D_0 is the diffusion length, $n_c(x)$ is the electron concentration at point x, τ is the recombination lifetime, η_{inj} is the injection efficiency and G(x) is the amount of photons absorbed at point x. The diffusion constant, recombination rate and the injection efficiency are all assumed to be independent of the position x and the electron concentration at every point. The PDE under appropriate boundary conditions is solvable analytically. The boundary conditions come from the physical aspects of the device: $n_c(0) = n_{c0}$ is true at short circuit conditions, as the excess electron concentration at the working electrode is zero, because all of them are instantly extracted as current. Another boundary condition

$$\frac{dn(d)}{dx} = 0$$

is based on the fact that there is no electron gradient at the edge of TiO_2. This is true, because the TiO_2 is finite and simply ends. The G(x) function is derived from the absorption coefficients of the devices and can be measured experimentally. The G(x) is different for the measurements from the working or the counter electrode sides. Because of this difference, the diffusion coefficient can be obtained by fitting the front/back IPCE.

The analytical form of the solution was obtained with the software Mathematica and a visual fitting procedure was written in Igor Pro, results of which are presented in Chapter 6.

Once the diffusion length is obtained, the proportion of electrons reaching the electrode through the TiO_2 from a distance x is obtained via the following equation:

$1 - \exp(-D_L/x)$

If the electron concentration profile is known, by simply numerically integrating over the entire thickness of the TiO_2 it is possible to obtain the total percentage of electrons which reach the electrode without recombination. Finally, when the proportion of electrons lost to recombination are known, the amount of photons absorbed are known and the actual measured current is known, injection efficiency can be calculated correctly. This procedure will be instrumental in Chapter 6, where injection dynamics and mechanisms will be discussed.

Chapter 4. Transient absorption spectroscopy in the mid-IR

Introduction

This chapter focuses on visible-pump, mid-IR probe ultrafast transient absorption spectroscopy. The technique has been used on devices similar to DSSCs as far back as 1998.[32] More papers followed using the same technique but with varying experimental conditions.[36, 81, 82] The samples that were measured by the group of Lian et al., were never complete DSSC devices as most of the time redox pair was absent from the electrolyte employed. In addition, not enough basic experiments were done to evaluate the choice of experimental conditions in terms of light intensity, acidity of solution, sample degradation, sample translation or presence of optical artefacts around time zero. In the present chapter, several of the basic experimental setup sensitivities are investigated. In Chapter 3, instrumental artefacts are described and in the present Chapter they are shown to be important for correct interpretation of the spectra in several cases.

Mid-IR probe wavelengths are very attractive for their ease of interpretation. As will be discussed below, electrons in the metal oxide are the main absorbing species in the mid-IR, with extinction coefficients which are much higher than any vibrational changes in the excited or photo-oxidized dye spectra. The assignment and quantification of electron injection is relatively easy in the mid-IR, compared to visible/NIR spectra. The main findings of this Chapter have been published in [83]. The results presented here were achieved while working in close collaboration with Dr. Marius Kaucikas and Dr. Jasper van Thor.

Experimental methods

Variations in injection rates are reported in the present Chapter as measured with pump-probe TAS on samples sensitized with either the ruthenium metal-centered (N719, N3) dyes or an organic donor-π-acceptor D149 dye.[84] An ultrafast visible-pump, mid-infrared probe system was used with a time resolution that spans from < 300 fs to 1.5 ns. Samples which closely resemble complete devices were used, with the same components and preparation methods as for preparing working solar cells in our laboratories. The only differences were that the samples had no conductive electrodes, e.g. fluorine doped tin oxide and were deposited on sapphire or CaF_2 substrates instead of glass to allow transmission in the mid-IR. The I^-/I_3^- electrolyte used in the N719 and N3 samples was composed of 0.8 M 1-propyl-3-methyl imidazolium iodide, 50 mM I_2, 50 mM guanidinium thiocyanate and 0.3 M benzimidazole in 3-methoxypropionitrile, in the text referred to as the ‘DS’ electrolyte. The same ‘DS’ electrolyte, but without the benzimidazole additive was employed for the

D149 samples. The sample preparation methods and the experimental setup are provided in the experimental methods (Chapter2) and are similar to our previous publications.[85]

Two different nanoparticulate, mesoporous metal oxide substrates were used: 7 µm thick TiO_2 and 6 µm thick ZrO_2. The samples are labelled throughout the Chapter as e.g. ZrN719DS, indicating the N719 dye on ZrO_2 filled with the DS electrolyte.

In addition to the data on TiO_2 above, N719 dye on ZrO_2 deposited on both sapphire and CaF_2 substrates were also measured. Dyes on ZrO_2 are known to be non-injecting, hence this data gives a good baseline of how the spectra in the mid-IR look like for the dyes which do not inject. It will then be used to aid the interpretation of electron injection on mesoporousTiO_2 electrodes.

Visible pump, mid-IR probe of N719 on ZrO_2

Transient spectra at 4000 – 5700 nm range

Transient mid-IR absorption spectra of N719 on ZrO_2 deposited on a sapphire substrate and immersed in DS electrolyte was recorded in the range 4000 – 5700 nm. The photodetector array used was capable of recording an interval of 320 nm in one experiment; hence 7 partially overlapping spectra were taken over one day. For some of the wavelength ranges, the spectra contained considerable noise. It was possible to remove the noise by averaging the absorption change signal amplitude before time zero and subtracting it from the averaged last 1 nanosecond of the absorption. As a repeat of the main observation in the spectra, N719 on ZrO_2 deposited on a CaF_2 substrate and immersed in DS electrolyte was also recorded in the range of 4700 – 5200, using a different photodetector array. The transient absorption spectrum of the sample on CaF_2, after adjusting the amplitude to account for different pump pulse intensities used during the two experiments, is overlaid in red color, Figure 4.1. The two graphs coincide closely with slight differences, attributable to instrumental artefacts and noise.

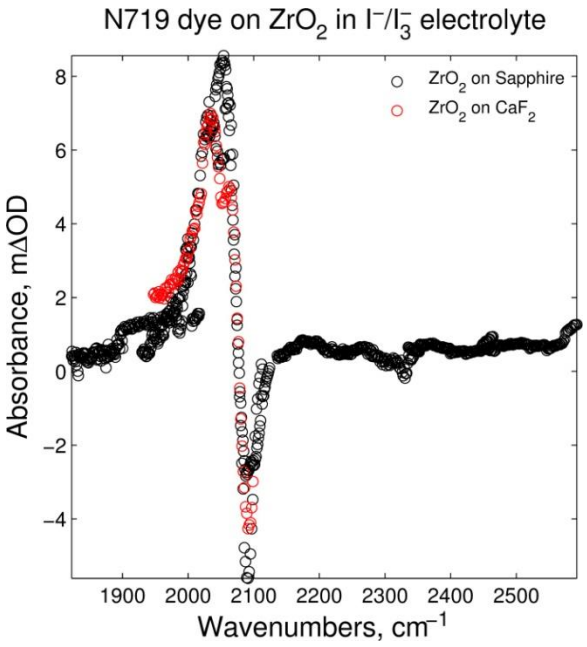


Figure 4.1. N719 dye on ZrO_2 immersed in I^-/I_3^- electrolyte in MPN (referred to as DS). Absorption change signal averaged over the time interval between 1 ns and 2 ns. The signal decays less than 10% over this time period, close to the noise threshold, hence averaging is justified. In addition, the absorption change signal before time zero was averaged and subtracted to remove background noise in some of the measurements. Pump intensity was roughly 4 μJ per pulse with a circular pump size of 300 μm FWHM.

Assignment to SCN and steady-state FTIR

The measured absorption change around 2100 cm^{-1} is assigned to the red-shifting of the SCN^- stretching vibration. Steady-state FTIR spectra of the N719 dye, in both solid form and adsorbed on TiO_2 was published in [86] and the signal at 2100 cm^{-1} was assigned to the SCN^- ligand. Same assignment was achieved in another theoretical study.[48] The SCN^- stretching absorption appears to move to lower energies after the pump pulse, consistent with calculations showing the highest-occupied molecular orbital (HOMO) of the ground state localized over the Ru metal center and SCN^- ligand. The 2100 cm^{-1} peak can be observed in a steady-state FTIR spectrum of ZrN719DS on CaF_2, given in Figure 4.2. Comparing Figures 4.1 and 4.2, in the range of 1800 – 2600 cm^{-1} only the SCN^- stretching vibration exhibits measurable change upon photoexcitation of the dye. The light absorption at 580 nm initiates a metal-to-ligand charge transfer event, where an electron from the Ru metal jumps to the π-system of the bipyridine ligand. Due to electrostatic inductive effect, the more positive charge on the Ru metal destabilizes the SCN^- bonds, hence reducing the bond strength and decreasing the amount of energy required to excite the stretching vibration to the higher energy

level. This causes a red-shifting in the absorption: the bleaching around 2100 cm^{-1} and an increase in absorption at 2050 cm^{-1}. The dye has no other absorptions in the 1800 – 2600 cm^{-1} range.[86] However, in Figure 4.2 it is evident that the electrolyte contains species which do have absorptions in that range, but nothing is observed in the transient absorption spectrum, implying that in the first 1.5 ns after excitation no observable energy or charge transfer between the photoexcited dye and any other species occur. This was true for the range 2000 – 2150 cm^{-1}, where no signal averaging was required due to strong signal. This point will be discussed in more detail below. An important wavelength worth mentioning at this point is 1960 cm^{-1}. From the spectrum it is evident that at 1960 cm^{-1}, compared to the absorption change which is occurring around 2100 cm^{-1}, is roughly 10 times lower in amplitude. In later sections, electron injection from the dye to TiO_2 will be measured at 1960 cm^{-1}.

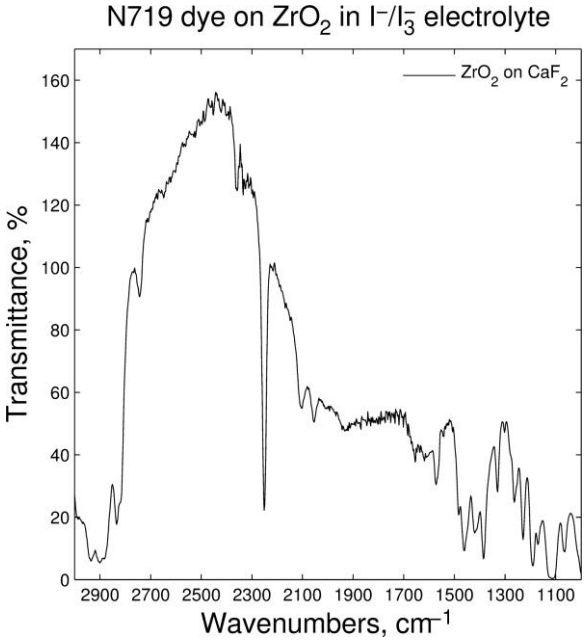


Figure 4.2. Steady state FTIR spectrum of ZrN719DS on CaF_2. Note that this spectra was recorded with the DS electrolyte present which has many components, hence a lot of high intensity peaks. The SCN^- peak can be seen at 2100 cm^{-1}.

Long-lived absorption in the TAS before time zero: another experimental artefact

To illustrate what misinterpretation of an artefact may look like, a brief example of an experimental condition is outlined. An interesting observation is made if one looks at the transient absorption spectra of ZrN719DS on CaF_2 before the pump pulse arrives, i.e. before time zero. Time zero indicates the time when the pump pulse arrives. For this particular experiment, the real time zero was somewhere between -0.5 and +2 ps of the initially observed strong absorption change. Figure

4.3 illustrates the spectrum, averaged over 20 to 40 picoseconds, before time zero and magnified 10 times to show how it compares to the photoexcited dye transient absorption. Interestingly, same pattern was observed recently by another group.[87] In that publication, the effect could have been attributed to perturbed free induction decay, as it occurred 200 fs before time zero, whereas here the effect is observed even 25 ps before time zero. Several explanations exist: instrumental artefact, higher noise due to reduced signal-to-noise ratio due to strong steady-state SCN^- 2100 cm^{-1} absorption or some kind of very long lived species. The SCN^- vibrationally excited at 2100 cm^{-1} has a lifetime of approximately 30 ps.[88] Hence, where this is observed, it could be a result of the vibrationally excited SCN^- interacting with the pump light: emitting at 2100 cm^{-1} radiation which shows up as a negative absorption change before time zero. The most likely explanation is, however, an experimental artefact arising due to 5 mm thick CaF_2 substrates. The same effect is absent when using 0.5 mm thick sapphire substrates. It is most likely due to the probe beam reflection inside the CaF_2 substrate and hence the small proportion of the probe, the one which is reflected, travels ~40 ps of additional path and hence sees the sample after it was hit by the pump pulse. Even when the probe is nominally before the pump, the reflected fraction of the probe passes the sample only after the pump, hence the appearance of the low amplitude signal which coincides with the TAS signal after 1.5 ns.

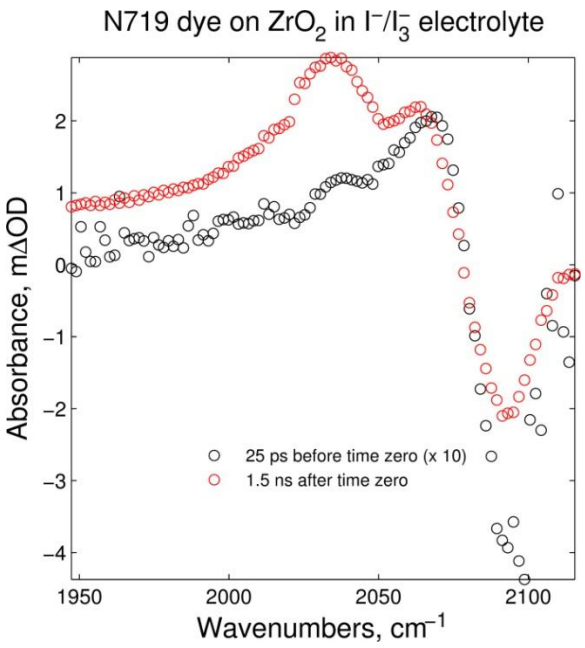


Figure 4.3. Initial averaged transient absorption signal before time zero of ZrN719DS on CaF_2. It shows that before the optical excitation (pre-pump), there is a residual weak signal around the characteristic SCN^- stretching vibration already present (black circles). This signal was averaged over 4 time-points in the interval 10 – 40 ps before time zero and multiplied by a factor of 10. Overlaid

(red circles) is the transient absorption of the photoexcited dye at the same wavelength range for comparison. The 25 ps before time zero absorption is an instrumental artefact due to light reflection in a 5 mm thick CaF_2 substrate.

Absorption of photoexcited N719 on ZrO_2 after pump pulse

Figure 4.4 illustrates the kinetics of the N719 dye adsorbed on ZrO_2. As is evident from the graph, after the initial rise of the signal around time zero due to photoexcitation the signal does not change by more than 5% at the 4 depicted wavelengths. This lack of dynamics upto 1.5 ns is in line with the photoexcited N719 average lifetime of ~20 ns. It is also the very first proof that no excited state quenching, charge transfers or charge injection into ZrO_2 occurs, at least not in the timescales slower than the instrument response time of ~300 fs. The initial jump and decay which occurs one picosecond around time zero, are attributable to a combination of the equipment artefacts described in the Chapter 3: probe chirp, cross-phase modulation and perturbed free induction decay.

With the data presented and interpreted in Figures 4.1-4.4, we can now turn to the analysis and interpretation of the mid-IR pump-probe spectroscopy of the other dyes based on ruthenium metal centered coordination compounds and adsorbed on TiO_2.

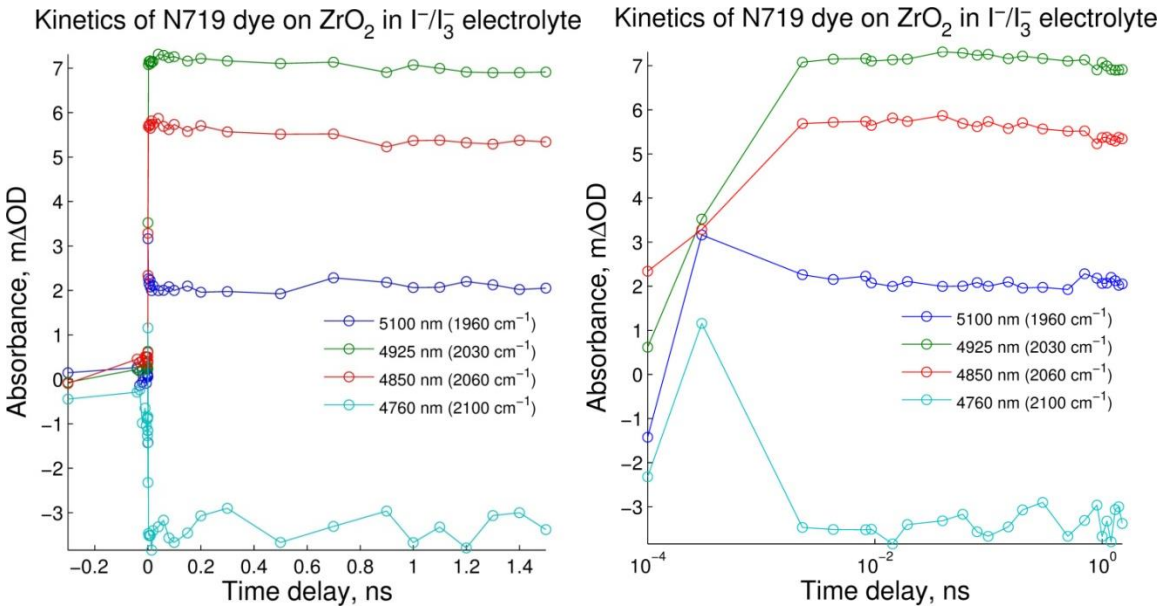


Figure 4.4. Kinetics measured by transient absorption in the mid-IR at the major absorption change peaks. Here the sample was the N719 dye on ZrO_2 in DS electrolyte (ZrN719DS).Signals decay by less than 5%, in line with photoexcited state decay lifetime. The noise around time zero was discussed in the current Chapter and in the previous Chapter on instrumental artefacts. On the right, the same

graph but with the X-axis on the log scale (note: negative time delays are not shown on logarithmic timescales).

Pump-probe spectroscopy in the mid-IR of dyes on TiO_2

Experimental conditions

In the results presented below, no sample translation was employed during a single TAS measurement. Samples were moved between the measurements to ensure a fresh spot of the sample is measured each time. Translation during the measurements was done, but was not found to make any significant impact on the measured results. Comparison and discussion of the translated versus non-translated results are given in a section below. Samples were probed in the 1900-2100 cm^{-1} range. Spectra of excited N719 on TiO_2 and on non-injecting ZrO_2, both filled with the I^-/I_3^- DS electrolyte are provided in Figures 4.1 and 4.6. They agree well with the ones reported by other researchers.[36, 87] Injection kinetics of the N719 dye on TiO_2 were probed at 1960 cm^{-1}, as the absorption was close to flat around that wavelength. Absence of strongly absorbing peaks in the spectrum on ZrO_2around 1960 cm^{-1} implies the probe signal is almost free of any contributions from both excited or oxidized dyes or any other species in the electrolyte. Some contribution of the SCN^- vibration change may contribute to the measurements at 1960 cm^{-1}, however, that contribution is much smaller than the electron absorption, as will be seen later.

In Figure 4.5, steady-state UV-Vis measurements of the samples used in this section are provided. The two samples were N719 and D149 dyes on TiO_2 in DS and DS-noBz electrolytes respectively.

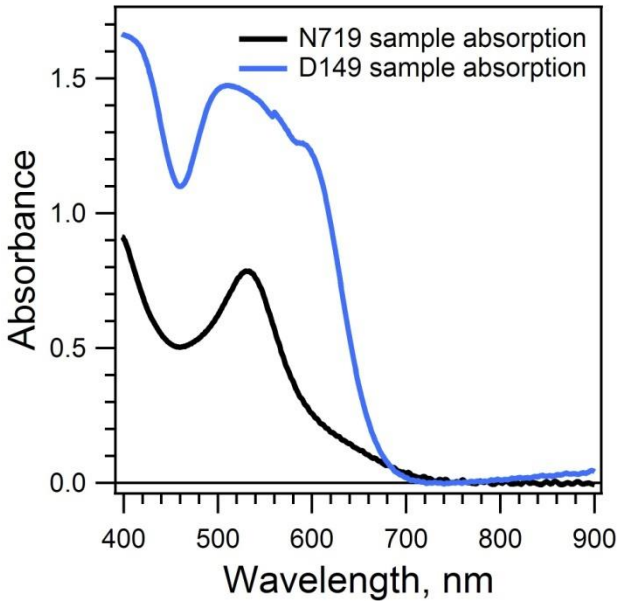


Figure 4.5. Absorption spectrum of the samples used for mid-IR transient absorption spectroscopy. The apparent absorption due to light reflection and absorption by the substrates was subtracted, leaving the absorption of the dyes only.

Spectrum of photoexcited N719 and D149 on TiO_2

In Figure 4.6, transient absorption spectrum of N719TiDS sample in the mid-IR is given at several delay times after the pump pulse. The negative absorption before time zero is attributed to electrons recombining between the pump pulses, as explained in more detail in a later section. At longer time delays, a constant rising absorption over all the wavelengths is observed, which is attributed to the injected electrons into TiO_2. A characteristic bleaching around 2100 cm^{-1} and a corresponding increase in absorption around 2050 cm^{-1} is observed, in agreement with the SCN^- stretching vibration discussed above on ZrO_2 samples. The electron absorption signal at 1350 ps is roughly 10 times stronger than the SCN^- vibration. The relative amplitude of the absorption at 2050 cm^{-1} with the absorption at 2080 cm^{-1} stays constant over the entire measured timescale of 0 to 1.5 ns, after the photoexcitation is finished. This implies no significant changes in the absorption spectrum of SCN^- stretching vibration takes place when the photoexcited dye is converted to the photooxidized dye and the entire change in the spectrum after time zero is attributed to the rise of absorption due to electron injection. On the right hand side of Figure 4.6, a time dependent spectra of D149 on TiO_2 in a redox-active electrolyte is given. No data on ZrO_2 was recorded, hence no comparison with a non-injecting sample is possible. There is a clear lack of sharp spectral features which would be the likely result of changes in the vibrational spectrum. An interesting characteristic is an apparent higher absorption, by a factor of two, in the red part of the spectrum compared to the

bluer, 2060 cm^{-1} part. Origins of this inhomogeneity are not clear. A possible explanation for the noisy spectrum could be misbehaving photodetector arrays. This has been observed on the equipment used here in other experiments and the origins of this experimental glitch were not identified. However, the double exponential fitting time and amplitude constants are close to identical for all wavelengths. The rising signal is attributed to electron injection. The photoinduced injection appears to proceed much faster in the D149 case compared to N719. The rise is almost entirely finished by 100 ps. In the N719 case, the electron absorption signal still appears to be rising even 1.4 ns after the excitation pulse.

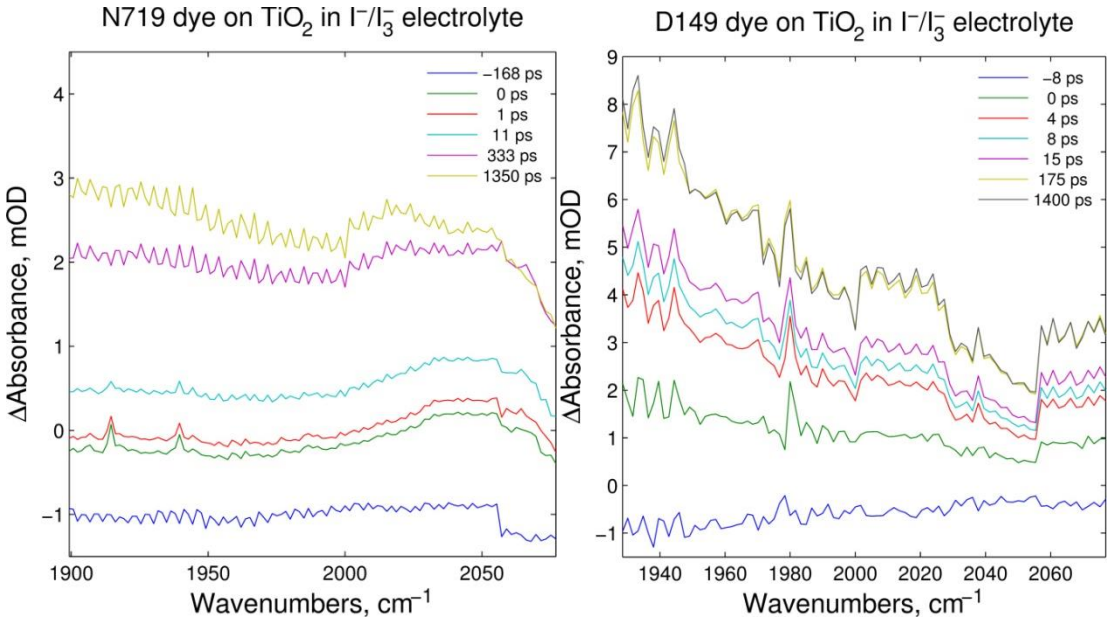


Figure 4.6. Transient absorption spectra of N719 on TiO_2 in an I^-/I_3^- electrolyte (left) and D149 on TiO_2 in an I^-/I_3^- electrolyte without benzimidazole (right). Samples were excited at 580 nm but with different pump intensities, hence the y-axes are not comparable.

Subtraction of before-time-zero negative absorption change

It is noted that all the kinetic traces on samples with TiO_2 had a negative absorption change before time zero, which was offset as a baseline in all data sets. This negative signal before the rise is attributed to the injected electrons which did not fully recombine between pump pulses. This negative offset was not observed for samples in neat acetonitrile or on non-injecting ZrO_2 films. Recombination of electrons to iodine is occurring during the waiting time between the no-pump and with-pump probe pulses. Previous transient photovoltage experiments indicated that electron lifetime is several milliseconds at 1 sun illumination in similar devices.[89] The no-pump and with-pump pulses are spaced at 1 ms. Electron recombination occurs in between these pulses and thus electron concentration differs between the two probe pulses. This difference shows up as the

negative signal before the rise. That does not change the interpretation of the results. In fact, the experimental conditions are closer to what would be observed under operating conditions at open circuit. Under such conditions, solar cells are under a constant flux of photons and a high concentration of electrons is present at all times in the TiO_2, on the order of 10^{18} cm^{-3} or equivalent to approximately 10 electrons per particle. In the current femtosecond laser spectroscopy experiment, a steady state concentration of electrons in the TiO_2 film will be reached after several pulses. At the steady state, all the injected electrons from each new pump pulse will recombine completely within the 2 milliseconds before a new pulse arrives.

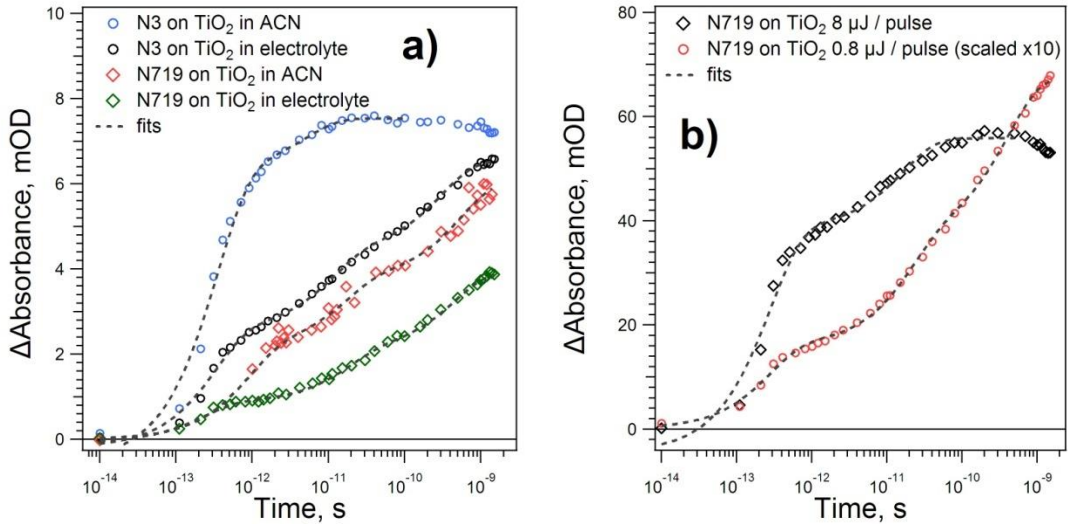


Figure 4.7. Electron absorption rise signals of N3 and N719 sensitized TiO_2 samples immersed in an I^-/I_3^- electrolyte or neat acetonitrile (ACN). Samples were pumped at 580 nm (pulse FWHM 300 µm) but at different light intensities. In graph **a)** the pump intensities were in the range of 500 – 800 nJ per pulse (peak powers of ~4.7 – 7.5 GW cm^{-2}). Graph **b)** illustrates that predominantly ultrafast kinetics are observed when the pump intensity is very high (peak power 75 GW cm^{-2}). The amplitude of the red trace with energy of 0.8 µJ per pulse was scaled by a factor of 10 to account for light intensity difference between the traces. Fitting parameters are provided in Table 4.1.

Discussion of spectra

Figure 4.7 illustrates the photoinduced absorption change at 5100 nm (1960 cm^{-1}) versus time of TiO_2 films sensitized with N3 or N719 in an I^-/I_3^- electrolyte or neat acetonitrile (ACN). The samples were pumped at 580 nm with the integrated photon flux equivalent to what the cells would absorb at approximately 4-5 suns. No differences in kinetics or spectral features were observed when lower light intensities (80 nJ / pulse) were used on the same samples, as illustrated in Figure 4.8. At lowest

pump light intensities (80 nJ / pulse), approximately 4 electrons per 20-nm diameter TiO_2 particle are injected per pulse in the first 100 nm of the film. There are approximately 350 dyes adsorbed on a single particle. Approximately 1% of the chromophores are excited at these light intensities. No second order effects such as triplet-triplet annihilation are expected to occur at such low excited state concentrations. The positive absorption change in Figure 4.7 is attributed to the injected electrons, which are known to absorb light from 500 nm to at least 8000 nm.[36, 90] It has been previously shown that rising electron absorption in TiO_2 in the mid-infrared matches the disappearance of the excited state of the N3 dye measured at 1200 nm.[52] Therefore, the absorption is attributed to injected electrons in the TiO_2. Overlaid on the data are fits using a sum of either two or three exponential functions. The fitting parameters are given in Table 4.1. Overall, the data show injection occurring over a wide range of time constants from femtoseconds to picoseconds and beyond. It is noted here that some transients appear to not have stopped increasing even at 1.5 ns. The < 300 fs components are about equivalent to the instrument response time, and thus may represent faster time constants. In three of the cases shown, a significant amount, ~40% of the rise occurs with a > 300 ps lifetime. These results closely agree with previous experiments conducted on full solar cells, but probed in the visible instead of the infrared region.[18]

Discussion of kinetics

In Figure 4.7, the sample sensitized in a freshly prepared N3 dye solution and immersed in neat acetonitrile showed ultra-fast kinetics only, in agreement with many previous results.[23, 36] N3 is more acidic than N719 and no other potential determining species were present in the solvent. Protons from the acidic dye solutions are known to adsorb to the TiO_2 surface and drive the conduction band edge down, increasing the driving force for injection and accelerating the kinetics.[59] When the N3 sample was re-filled with the I^-/I_3^- electrolyte containing base, the kinetics became close to identical to an N719 sample in both I^-/I_3^- electrolyte and neat acetonitrile. It must be noted here that the N719 sample immersed in acetonitrile was prepared from an N719 solution which was already used several times, therefore it can be expected that the solution was less acidic and did not have as many protons as a fresh one. This situation is true in a usual lab setting, where the same dye solution is used to prepare several identical devices. These differences between the samples serve as a proof that the injection kinetics are highly sensitive to any potential determining species in both the dye solution and the electrolyte.

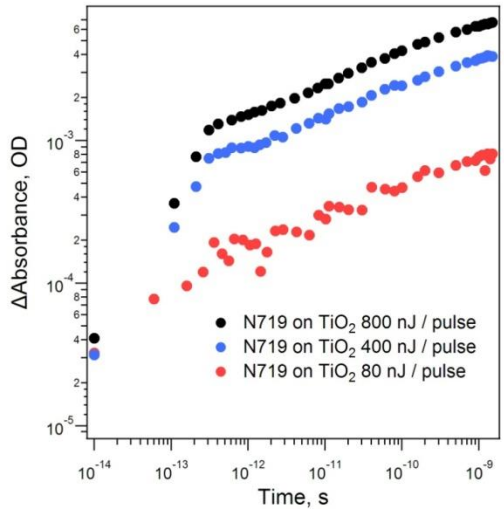


Figure 4.8. Electron injection kinetics measured at different pump intensities. The pump pulse width FWHM was 300 µm. Pump pulse wavelength was 580 nm. The sample was an N719 dye sensitized TiO_2 film immersed in an I^-/I_3^- electrolyte. No change in kinetics was observed with increasing pump light intensity. The amount of absorption change scales linearly with pulse intensity implying no second-order optical effects occur.

High light intensity induces ultra-fast apparent injection kinetics

Another phenomenon that was observed was a change in injection kinetics when high light intensity in excess of ~8 µJ / pulse (peak power: 75 GW cm^{-2}) was used. This is demonstrated in the graph of Figure 4.7b. The rise within the instrument response became dominant with a smaller component on several picoseconds timescale. A trace at lower pump light scaled by a factor of 10 to adjust for different intensities is overlaid for comparison. One explanation for the instantaneous kinetics is that the injection was occurring from a high energy, S_n ($n > 1$) excited state. The huge light intensity could produce a population of such states by doubly exciting the dye. A third of the rise is observed with a 16 ps rise-time, while virtually no rise occurs with a > 16 ps lifetime. At longer delay times a fall in the signal is observed. This fall is attributed to electrons recombining back to the photo-oxidized dye or iodine, as it has previously been shown that at high TiO_2 electron concentrations recombination becomes faster, reaching a lifetime on the order of tens of picoseconds.[91] In addition, the slower injection, if present, was also not observed as it would have been masked by the fall of the signal due to recombination. It is noted that recombination on its own cannot explain the sudden change in injection kinetics. After the kinetic traces were scaled for light intensity, the femtosecond fraction of injection appears to be several times higher, i.e. not linear in intensity, suggesting some additional effects are occurring. It is not clear at this point why that is the case. Another possibility is non-linear absorption coefficient of electrons in TiO_2. At high electron concentrations many trap states could become filled and electronic transitions inside the TiO_2 could become available which are not

observed at lower electron concentrations. These transitions could have a higher extinction coefficient and hence give rise to the observed apparent ultrafast injection. It is not clear at what excitation levels the injection becomes predominantly ultrafast. In our data, the transition was sudden when the light intensity was increased 10-fold, at light levels equivalent to illumination from ~100 suns.

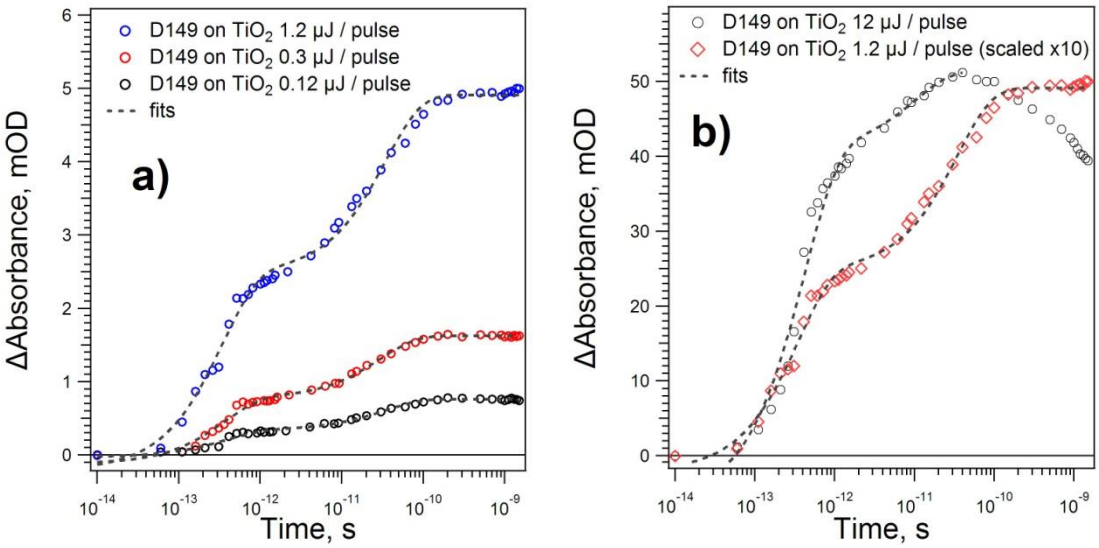


Figure 4.9. Transient absorption kinetics of TiO_2 sensitized with the D149 dye, immersed in an I^-/I_3^- electrolyte at different pump intensities. At lower pump intensities, in graph **a)**, no differences in the kinetics were observed. However, in graph **b)** the injection kinetics suddenly became ultrafast, similarly to what was seen in Figure 4.7b. The injection kinetics were fitted with a sum of two exponentials. The fitting parameters are given in Table 4.1.

Sample	Photon flux	Pulse energy	τ_1 (A1)	τ_2 (A2)	τ_3 (A3)
N3	9.3E+17	800 nJ / pulse	330 fs (41%)	11 ps (27%)	310 ps (32%)
N719 in ACN	9.3E+17	800 nJ / pulse	350 fs (35%)	17 ps (27%)	560 ps (38%)
N719	7.00E+17	600 nJ / pulse	230 fs (23%)	18 ps (30%)	460 ps (47%)
N719	9.3E+17	800 nJ / pulse	270 fs (24%)	20 ps (30%)	400 ps (46%)
N719 + TR	9.3E+17	800 nJ / pulse	320 fs (35%)	39 ps (26%)	510 ps (39%)
N3 in ACN	9.3E+17	800 nJ / pulse	340 fs (84%)	5 ps (16%)	
N719	9.30E+18	8000 nJ / pulse	280 fs (70%)	16 ps (30%)	
D149	1.40E+17	120 nJ / pulse	380 fs (46%)	33 ps (55%)	
D149	3.50E+17	300 nJ / pulse	360 fs (50%)	30 ps (50%)	
D149	1.40E+18	1200 nJ / pulse	340 fs (52%)	35 ps (48%)	
D149	9.30E+18	8000 nJ / pulse	400 fs (81%)	10 ps (19%)	

Table 4.1. Fitting parameters of a function sum of either two or three exponentials for the injection kinetics. All samples were in an I^-/I_3^- electrolyte unless stated otherwise. Photon flux is given in photons s^{-1} cm^{-2}. Pulse FWHM was 300 µm. No sample translation was employed except for the "N719 + TR" sample.

D149 TAS analysis: kinetics

The D149 dye excited at 580 nm to its S_1 state exhibited multi-exponential injection kinetics, as shown in Figure 4.9a. The rates are faster than for the N719 dye, with the slowest injection component at 30 ps. The rise has plateaued by 200 ps in all cases. The obtained injection rate is fast compared to the average luminescence lifetime of the dye which is ~280 ps in acetonitrile. [62, 92] At high light intensities, just like for N719, the kinetics became effectively instantaneous and signal decay appeared at longer delay times. As in the N719 case, the injection kinetics were otherwise independent of the light intensity below photon flux equivalents of ~10 suns. In Figure 4.9, the lowest light intensity photon flux is equivalent to the amount of photons that would be absorbed by the cell if it were irradiated with roughly one sun, which corresponds to practical operating conditions. Based on these results it can be concluded that the injection rates which are relevant to operating DSSCs are those obtained at lower light intensities and have a significant proportion of injection occurring at ~30 picosecond timescale.

Acidity causes band edge shifts, which results in lower V_{oc}

The redox active electrolyte used here has important effects on the TiO_2 energetics at the interface with the electrolyte. The electrolyte has potential determining species such as benzimidazole and cationic species and may considerably shift the TiO_2 conduction band edge compared to inert solvents.[93] Such shifts are absent from samples which use only a solvent or which are in vacuum: the conduction band edge is likely to be found at different potentials than in operating devices. Further to that, in previous femtosecond TAS experiments no attempts have been made to measure where the conduction band edge is. Injection efficiency can be very sensitive to conduction band edge shifts.[58] By employing a redox active electrolyte which may act as a buffer, fixes the band potentials and should in principle eliminate any discrepancy in measured kinetics between different laboratories. Here, larger fractions of femtosecond injection were observed in samples prepared with electrolytes which shift the conduction band edge towards more positive potentials by adding lithium ions. Full cells prepared with these same electrolytes show injection efficiencies close to unity. They have, however, ~35% lower open circuit photovoltage than with the optimized electrolyte. The efficiency optimized devices had ~15% injection losses. Results from these experiments and their relation to SPC and IPCE are described in Chapter 6.

Sample translation vs no translation

Translation of the samples during the TAS measurements has been tested in order to eliminate any effects or degradation that may arise as a result of prolonged periods of light exposure at the probe point. Some samples were spatially translated during the pump-probe measurements. The samples were translated in Lissajous pattern which guarantees that no single spot is probed twice in ~2 minutes time. The translation speed was adjusted to ensure that any given probe spot is hit with no more than 2-3 shots of the excitation pulse. The average speed of the translator was 50 $\mu m\, ms^{-1}$. [94] Although not ideal, this significantly reduces any effects which might arise due to excess charge accumulation or sample degradation at a single spot of the sample. The samples had some spatial inhomogeneity and in addition to the mechanical movements, translation increased the measurement noise by an order of magnitude. However, when translated and non-translated measurements were compared, no significant differences were observed in the injection kinetics and translation was deemed not required and was not used in further measurements. As can be seen in Figure 4.10 and Table 4.1, translation does appear to have some effect on the time constants and relative magnitudes, but translation has not significantly changed the overall wide distribution of injection times. As translation decreased signal to noise ratio by an order of magnitude it was judged unnecessary for the measurements. In Figure 4.10, in the graph on the right, transient absorption spectra with and without translation was compared for a non-injecting sample of N719 on ZrO_2. Evidently sample translation did not change the spectra at all. Higher noise was observed, just as in the TiO_2 case, however the sample translation is clearly not required for ultrafast TAS experiments.

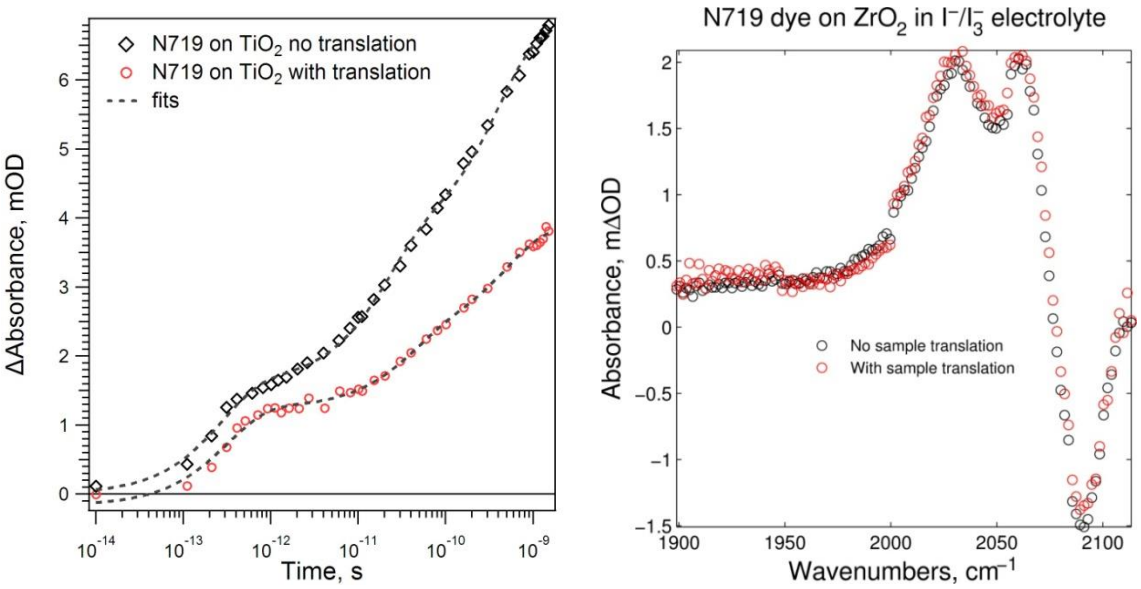


Figure 4.10. Injection kinetics of an N719 sample with an I^-/I_3^- electrolyte, without sample translation (black) and with (red). The fit coefficients are close to identical, given in Table 4.1. The reduced signal amplitude is likely a result of the sample inhomogeneity and less charging at the probe point. Graph on the right is translation and no-translation comparison of ZrN719DS sample, measured 1.5 ns after excitation by light.

Pulse peak-power intensity independence of electron injection

To further support the finding that no non-linear effects occur at least up to 15 suns equivalent light intensity of the pump pulse, short circuit current of a DSSC was recorded with varying pump pulse light strength at 580 nm. The log-log plot of current vs light intensity is provided in Figure 4.11. The slope of the curve is equal to 1, implying a linear relationship. Hence the light intensities used, even at high peak powers of several GW cm^{-2} do not affect the injection in a way that would render the analysis incorrect. At roughly 5 GW cm^{-2} peak power in Figure 4.11, the short-circuit current reaches the maximum value and does not increase any more (not shown in the Figure). The diffusion limitation of the viscous electrolyte in the DSSCs limits the current, which is not capable of carrying higher amounts of current beyond a certain threshold. The highest peak power in Figure 4.11, where the current is still linear in light intensity, is equivalent to the ~600 nJ / pulse energy given in Table 4.1. Hence most of the injection dynamics results in this Chapter were obtained at light intensities at or below the regime where short circuit current is linear in light intensity and therefore no second-order effects are expected in the spectra provided.

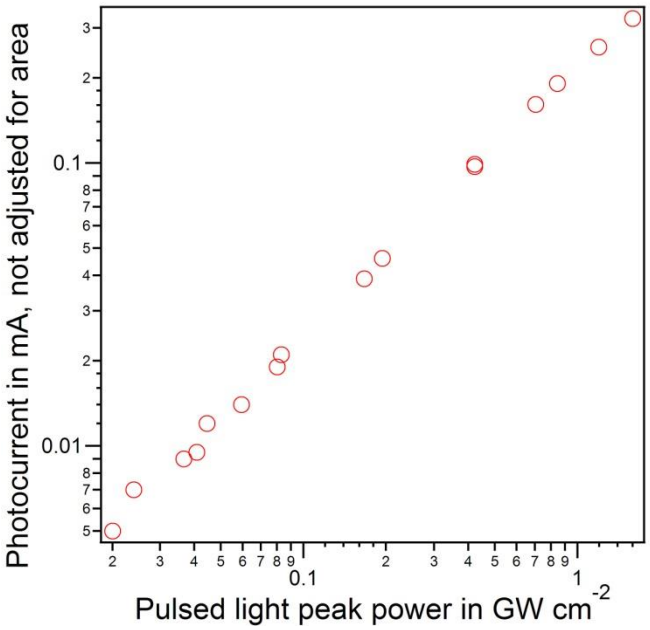


Figure 4.11. Short circuit photocurrent of a dye-sensitized solar cell utilizing a I^-/I_3^- electrolyte in MPN. The light source was ~100 fs laser pulses at 580 nm with a 500 Hz repetition rate. Photocurrent was measured using a multimeter and represents an average, steady-state photocurrent, not the peak after each pulse.

Additional spectra around 7500 nm

So far, samples prepared on sapphire substrates were analyzed. Both ZrN719DS and TiN719DS devices were also prepared on CaF_2 substrates. These substrates allow mid-IR measurements up to 10,000 nm wavelength (1000 cm^{-1}). Spectra around 7500 nm for these samples are given in Figure 4.12. The spectral time evolution of both, zirconia and of titania, completely agree with the previously shown spectra around 5000 nm. The graph illustrates additional vibrational excitations, which are attributed to the vibrational changes after excitation in the bipyridine ligands, which have multiple absorptions around 7500 nm.[95] The TiN719DS spectrum lacks the same strong spectral features because the electron signal is much stronger than the vibrational absorptions which are buried within the noise. The transient changes in the spectrum on ZrO_2 are expected in that region because bipyridine ligand receives an electron upon photoexcitation of the dye molecule. The additional charge destabilizes the whole aromatic system and changes the energy required to promote the molecule into a higher vibrationally excited state.[36] Nothing new about injection can be said from Figure 4.12 and hence it serves as additional support for the claims so far, albeit on a different substrate and at different wavelengths.

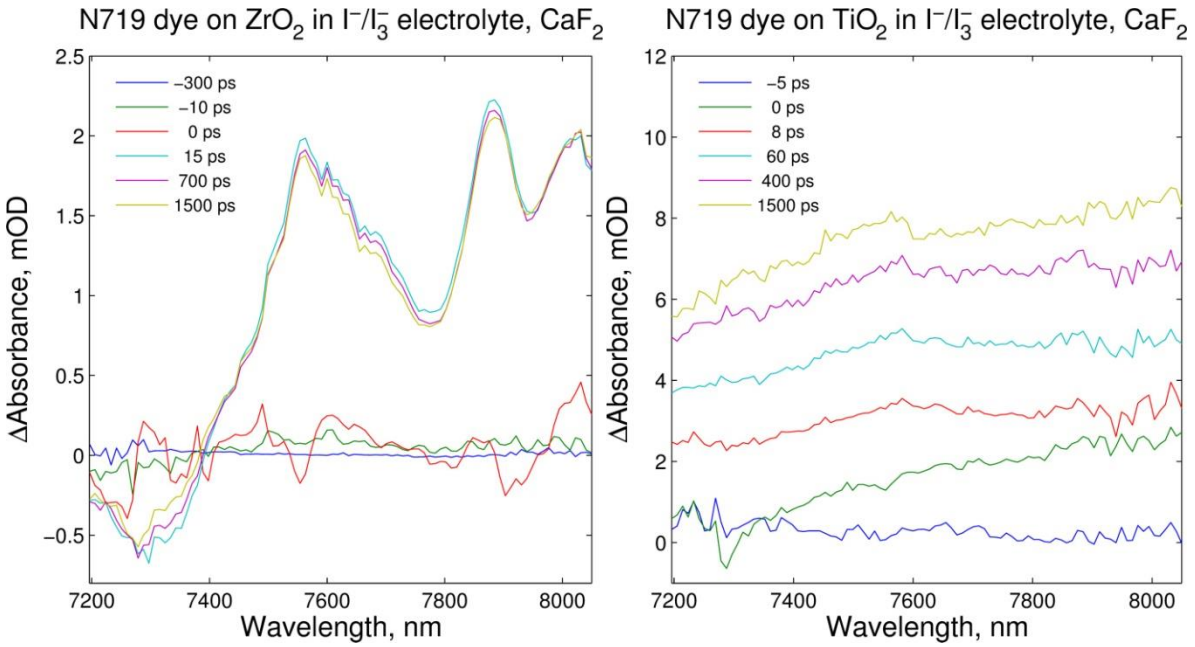


Figure 4.12. Transient absorption spectra of ZrN719DS (left) and TiN719DS (right) on CaF_2 substrate. CaF_2 allows for measurements at longer wavelengths than sapphire substrates. Additional vibrational features, compared to sapphire substrates, can be observed in the left graph. Injection kinetics were not affected and were identical than on the sapphire substrates for TiN719DS sample.

The measurements in perspective

Solar cells prepared with the N719 dye and the I^-/I_3^- electrolyte used herein had an injection efficiency of 90% ± 4%, derived from the front/back incident photon to current conversion efficiency (IPCE) ratio method, details given in Chapter 6.[58] Significant fraction of injection occurred with > 1 ps time constants in this device. Whether there were any aggregated or weakly adsorbed dyes in our samples is difficult to confirm experimentally. An additional argument follows from the N3 case in Figure 4.7. If slower than 100 fs rise components were attributed to aggregates, one can say that no more than 16% of injection occurs from aggregated dyes in the neat acetonitrile sample. The situation is very different once electrolyte is added: 60% of injection would have to occur from the aggregated dyes. It is difficult to imagine that addition of the electrolyte to the same exact film could induce such huge changes in the amount of aggregated dyes. It was, however, possible to obtain a dominant ultrafast injection component in the same samples, but only when very intense excitation pulses were used, with the photon flux on the order of several tens of suns. The differences in injection kinetics observed by other researchers referenced throughout the thesis could be at least partly explained by the observations made here. Different sample environments used among the other reports might have affected the energetics of the TiO_2, which we showed here to have a

significant impact on the injection kinetics. An additional factor is if a relatively short time delay line is used it prevents observation of injection at hundreds of picoseconds.

Open circuit condition used for TAS

These studies were carried out at the open circuit condition because conductive electrodes block the IR probe beam. Virtually all previous TAS studies of electron injection into TiO_2 have also been carried out at open circuit, without question of the appropriateness of this. Studies of electron injection concern the photocurrent producing capability of the dye/TiO_2 interface. One might argue that they should thus be studied at short circuit condition where photocurrent is measured. As mentioned above, it has rarely if ever been done. Several factors argue that the open circuit condition is acceptable for most DSSC devices. There is evidence that injection yields in most DSSCs are not decreased at V_{oc}, as compared to short circuit. This can be inferred from TAS yield vs potential and also from the success of models in reproducing the *JV* with only recombination as a source of loss.[15, 96, 97] On the other hand, there are two studies indicating injection rate is a function of external potential in inert electrolyte (one is on SnO_2) and one study indicating the opposite for functional cells.[38, 59, 98] Unfortunately it is not certain how the potential ranges used in the inert electrolytes can be related to the conduction band edge in the functional cells tested here. In reality, the solar cells are operated at the maximum power point (MPP) on the *JV*. If there are changes in injection with applied potential, the most relevant kinetics will be those at the MPP. At least in terms of the Fermi level inside the TiO_2, the MPP is arguably closer to the open circuit condition than the short circuit condition. In summary, the open circuit condition used here and other studies is defensible, though studies at short circuit should be done to compare. These are reported and discussed in Chapter 5.

Last words on the mid-IR spectra

It is important to note that transient absorption experiments in the mid-IR are experimentally complicated to setup properly and are prone to instrumental artefacts which are sometimes difficult to distinguish from actual signals. It is not always clear if the absorption change at different wavelengths is not an instrumental artefact. A good example is in Figure 4.6a, where one can clearly see a sudden increase in negative absorption change before time zero around 2060 cm^{-1}. Such sudden drops in spectrum are not known and it is most likely attributable to instrumental artefact. The fact alone that it was persistent even when averaged over 5000 shots, says that sometimes the absolute value of absorption change cannot be trusted with full certainty. Another example is a

sloping of the absorption when going towards higher energies in Figure 4.6b for the D149 dye. At longer wavelengths, the electron absorption coefficient should be increasing with a power law, according to Drude theory. It is not obvious why the slope is that big for D149 and it could have been an instrumental artefact as well. The kinetics, however, are unchanged for all wavelengths and are considered to be reliable.

Conclusion

This Chapter provided basic analysis of experimental conditions when performing TAS in the mid-IR on samples closely resembling dye-sensitized solar cells. It was shown that even at huge, on the order of GW cm^{-2} peak laser pulse intensities, the devices do not show any significant non-linear effects. The absorption changes scale linearly with light intensity, in accordance to Beer-Lambert law. In addition, it was argued that open circuit conditions and no sample translation give sufficiently reliable experimental results. Spectra of the excited N719 dye in the mid-IR was provided, which aided the interpretation of the electron injection observed at same wavelengths. It was shown that for efficiency optimized devices, the injection kinetics are at least biphasic, with N719 and N3 dyes having significant injection components at timescales longer than 10 ps. D149 dye had also biphasic injection, with a significant proportion of injection occurring at longer than 10 ps timescales as well. It was shown that acidic environments speed up the injection rate significantly. Finally, a phenomenon was presented, where the apparent kinetics become ultrafast, if very high light intensities are used on the devices.

Chapter 5. Visible to near-IR transient absorption spectroscopy

Introduction

In this Chapter, ultrafast visible pump, visible/near-IR probe spectroscopy is introduced. The technique is used to probe electron injection via the time-resolved observation of photo-excited dye, photo-oxidized dye and injected electron signal appearance in the TiO_2. TAS of dyes adsorbed on metal oxides in the vis/NIR region has been reported in the literature before. However, in this thesis, the most complete account is given due to several reasons. First, TAS was done on commercially relevant, operational dye-sensitized solar cells. This is in contrast to most studies, which used only partially assembled devices, with some components missing. Second, the time window was the longest reported so far, with the time delay spanning from femtoseconds to more than 6 nanoseconds. Thirdly, several important experimental checks were performed and reference non-injecting devices were fully characterized, which aided immensely in the analysis of the data. Lastly, a broad range of wavelengths, from 400 nm to 1500 nm were studied, adding additional confidence to the analysis. Later in the chapter and more significantly in Chapter 6, the data is correlated with the mid-IR data and with time-correlated single photon counting (time resolved photoluminescence). The majority of the results in this chapter have been published in [99].

Experimental

Vis-NIR femtosecond transient absorption setup.

Samples were excited with a pump light at 580 nm in the range of 46 – 90 μJ cm^{-2} (exact energy indicated in the text). The pump light was generated by a commercially available optical parametric amplifier TOPAS pumped by a Solstice Ti:Sapphire regenerative amplifier. More details are provided in Chapter 2. Pump laser excitation was followed by a second broadband pulse (830-1450 nm) generated in a sapphire crystal. HELIOS transient absorption spectrometer was used for recording the dynamics of the transient absorption spectra up to 6.5 ns with an instrument response function (IRF) of ~200 fs. The pump pulse frequency was 500 Hz. Absorption at each time delay was recorded for 5 seconds (2500 pulses) and this averaging was repeated 4 times, scanning in both directions. The pump pulse was unfocused and had a FWHM of roughly 3 mm while the probe pulse was focused to an FWHM of <0.4 mm. The pump pulse energy was measured through both 0.15 mm and

0.5 mm diameter pinholes. The energy per pulse per cm^2 was within 5% through both pinholes. The pump pulse is therefore homogeneous within the probe pulse area.

The procedure for determining accurate pulse energies was as follows. A pinhole with a known diameter is placed instead of the sample in front of the power detector. The pump light position is adjusted until maximum power is obtained through the pinhole. The pinhole is then exchanged for a wider diameter pinhole and the process is repeated. The pulse energy per unit area is thus obtained with high accuracy.

Sample preparation

Functional devices for vis-NIR TAS were prepared on FTO glass. One layer of the TiO_2 particles (~7 μm) was deposited onto sapphire or FTO glass by tape casting (also known as "doctor blading"). Further preparation instructions are provided in Chapter 2. Films were then glued using a surlyn gasket (DuPont, 25 μm thick) in a sandwich structure with either glass or sapphire and then filled with an electrolyte.

Device description and their absorption spectra

The majority of vis/NIR TAS spectra were recorded for eight main samples: two metal oxides (ZrO_2 and TiO_2), two dyes (C106 and N719, structures in Figure 2.1 in Chapter 2) and two electrolytes (DS and Li). Two different electrolytes were used to fill the solar cells. Abbreviation 'DS' stands for electrolyte containing 0.8M 1-propyl-3-methyl imidazolium iodide (PMII), 0.3M benzimidazole, 0.05M guanidinium thiocyanate and 0.05M I_2 in 3-methoxypropionitrile (MPN). Abbreviation 'Li' stands for electrolyte containing 0.8M PMII, 50 mM I_2 and 0.5M LiI in 3-methoxypropionitrile. Two different nanoparticulate, mesoporous metal oxide substrates were used: 7 μm thick TiO_2 and 6 μm thick ZrO_2. The samples are labelled throughout the Chapter as e.g. ZrN719DS, indicating the N719 dye on ZrO_2 filled with the DS electrolyte. The absorption spectra of the samples are given in Figure 5.1.

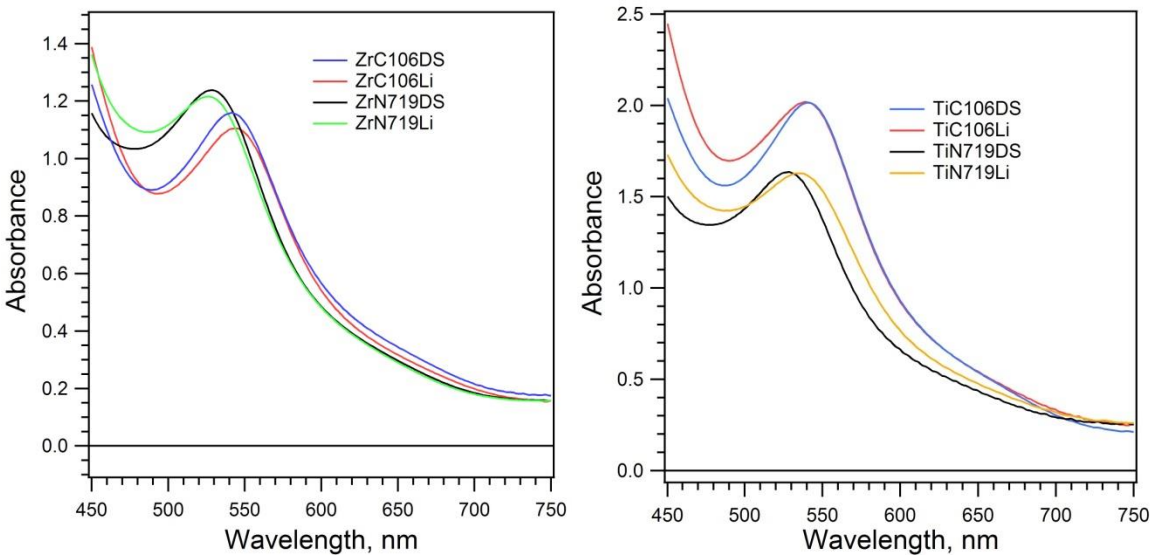


Figure 5.1. Absorption spectra of dye-sensitized devices prepared on ZrO_2 (left), the non-injecting samples. The operational devices, prepared on TiO_2 using the most common techniques are depicted on the right.

Current-voltage and performance of the solar cells

The devices on TiO_2 were fully operational and their current-voltage (JV) curves recorded under illumination of simulated 1 sun AM1.5G are given in Figure 5.2. The measured solar cell efficiencies and parameters are given in Table 5.1.

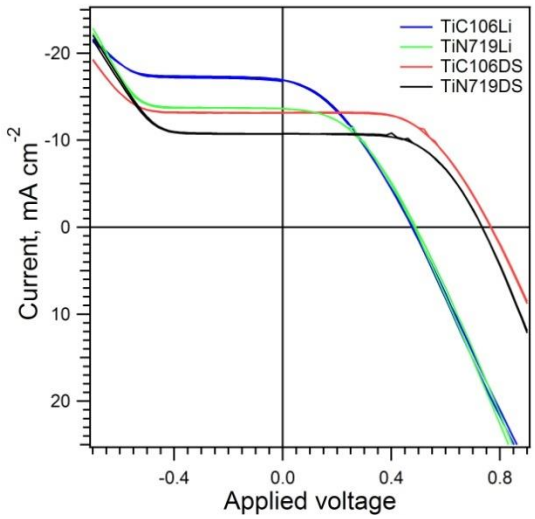


Figure 5.2. Current-Voltage curves of the TiO_2 devices at 1 sun simulated spectrum (AM1.5).

Device	V_{OC}, V	J_{SC},mA cm^{-2}	FF	Efficiency, %
TiC106Li	0.478	16.9	0.37	3
TiC106DS	0.766	13.2	0.58	5.9
TiN719Li	0.486	13.6	0.45	3
TiN719DS	0.734	10.7	0.60	4.7

Table 5.1. Solar cell parameters of the devices used in the experiments.

The devices with DS electrolyte are efficiency optimized and have a V_{OC} closely equivalent to champion devices utilizing electrolytes in MPN.[100] A smaller J_{SC} is mostly due to reduced light harvesting as only a single layer of non-scattering TiO_2 was employed. Lower J_{SC} for the DS devices compared to Li ones, even though the absorption is close to identical as shown in Figure 5.1, are possibly due to injection losses. Experimental results confirming this will be discussed in Chapter 6.

Samples do not degrade or change during the TAS measurements

Ultra-short pulsed lasers possess very large peak power intensities. In addition, to get a good signal-to-noise ratio, higher pulse intensity is usually employed. No sample translation was used in the vis/NIR TAS measurements. This was shown to not be a problem in the previous Chapter. However, a question of sample degradation/change was further addressed here. The issue of degradation is also important, because a complete measurement may last up to several hours. Hence if the sample changes over that period of time, it may change the dynamics or the steady-state spectrum. During a complete measurement, the sample was usually measured 4 times: scanning from negative time delays to 6.3 ns, then from 6.3 to negative delays, and this process repeated twice and in the end all the results would be averaged. To ensure the sample did not change during the measurement, the first forward scan and the last backward scans were compared. They were found to be close to identical (within noise) in all cases. Figure 5.3 illustrates a typical case, a TiO_2 sample sensitized with N719 and filled with the DS electrolyte, probed at 1200 nm.

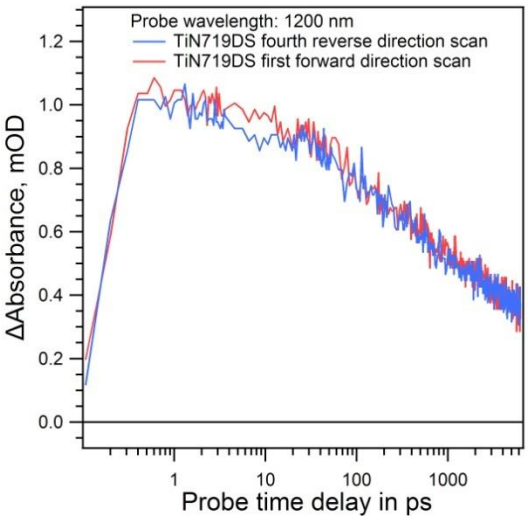


Figure 5.3. Red trace is a forward scan (from 0 ps to 6300 ps) of the sample TiN719DS probed at 1200 nm. Overlaid on top is the last scan in reverse (from 6300 ps to 0 ps) approximately one hour after the initial scan. Two more scans were recorded in between the first and last.

Pump pulse intensity affects amplitude linearly and does not change absorption difference dynamics

As in Chapter 4, pump-pulse intensity dependence was studied in the vis/NIR spectral range. Just like in the previous chapter, not only does the photocurrent scale linearly with intensity, but the spectrum varies linearly as well. In addition, no change in kinetics was observed either. This is true for light intensities which are not too high (< 10 suns). Figure 5.4 illustrates this at 1200 nm probe wavelength. The absorption change amplitude, which is the combined absorption of injected electrons and remaining photo-excited or photo-oxidized dyes, scales linearly with light intensity. This is as expected if no non-linear effects (e.g. exciton annihilation) take place. The dynamics should not be changing either, as long as the excited state density on the surface of the metal oxide is small enough for the excited molecules to not interact.

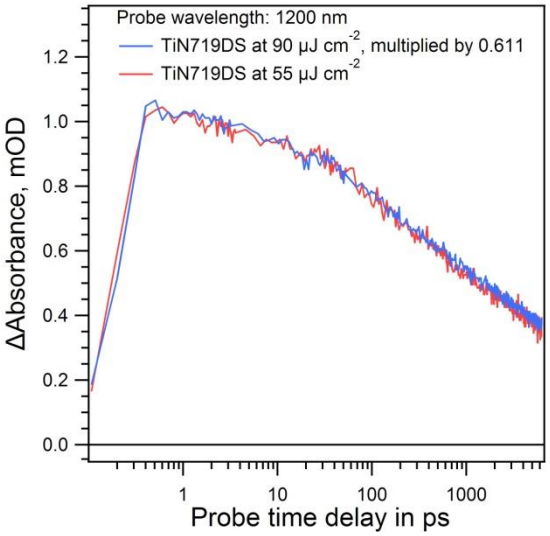


Figure 5.4. Sample TiN719DS probed at 1200 nm and excited with 580 nm pulses at two different intensities: 55 µJ cm^{-2} and at 90 µJ cm^{-2} per pulse. The higher intensity trace was multiplied by a factor of 0.611 (55/90). The two traces coincide perfectly and hence the scaling is linear. This observation suggests no non-linear effects were present during the transient absorption measurements and no intensity-dependent processes were observed at the light intensities used.

Short circuit or open circuit measurement conditions do not impact injection kinetics

Solar cells can be measured at different operating conditions. Most of the measurements reported in the literature and as discussed in Chapter 4, are usually done under conditions closest to the open-circuit, when the rate of injection and regeneration is perfectly balanced by electron recombination to electrolyte or photooxidized dyes. In this case, electrons will build up in the metal oxide until an electron density will be reached at which the injected electron amount per unit time will equal the amount of electrons recombining during the time until the next pump pulse. Under the short-circuit conditions, however, electrons have another escape path, i.e. to recombine with the electrolyte at the counter electrode. The steady-state electron concentration that an injection dye sees upon arrival of a pulse is hence different by an order of magnitude, as reported in the literature.[101] It may be argued that at much higher electron concentrations, electrostatics would prevent or slow down electron injection into the metal oxide nanoparticle. However, due to the high dielectric constant of titania (~80), this is not the case. In fact, the electron injection dynamics are not affected at all, as illustrated in Figure 5.5.

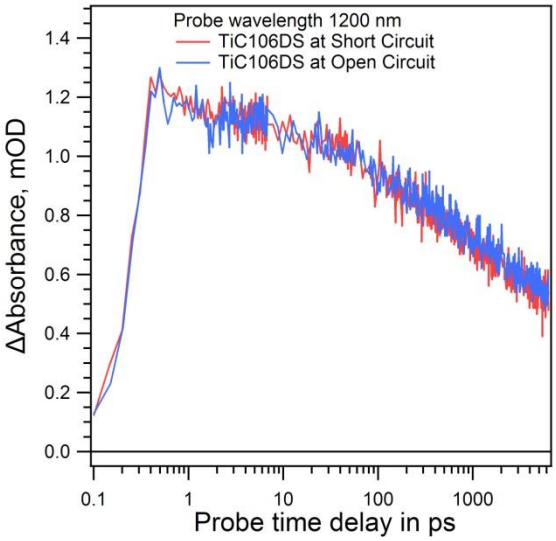


Figure 5.5. Transient absorption change at 1200 nm of the TiC106DS sample at open circuit and short circuit conditions. The short circuit data was multiplied by 1.08 to match peak absorptions. A single forward scan was used here instead of an average of 4.

In the remainder of the Chapter, transient absorption spectra of dyes on ZrO_2 and TiO_2 metal oxides in two different electrolytes are presented and interpreted. Assignments of the transient species are given and where relevant, extinction coefficients determined. These parameters will then be used to interpret the dynamics of the transient spectra.

Photo-excited N719 on ZrO_2 does not undergo any charge transfers

The transient absorption of N719 on ZrO_2 in both electrolytes exhibits a broad absorption spectrum ranging from <850 to >1300 nm (Figure 5.6). Transient absorption spectra in Figure 5.6 of the ZrN719DS and ZrN719Li are essentially the same. The spectra are in agreement with previously published reports of the photo-excited state of N719 in solution and on non-injecting ZrO_2 substrates.[102] In addition, the decay kinetics probed at 1200 nm (Figure 5.6) are consistent with previously published average luminescence lifetime of ~20 ns for the N719 dye.[59] The transient absorption amplitude is decreasing over all wavelengths equally and no spectral evolution in the wavelength space is observed. The excited state absorption of N719 in solution agree closely with the spectra of N719 adsorbed on ZrO_2 (Figure 5.6).[102] The dye ground state absorption is not changed by adsorption on ZrO_2 either. These observations imply there are no charge transfer processes occurring between the excited state of the dye (N719*) and the ZrO_2 surface. The entire transient absorption spectrum is therefore assigned solely to the N719* in Figure 5.6. No injection is expected theoretically also, as the conduction band edge energy of ZrO_2 is considerably higher than

the HOMO of the N719 in its excited state. According to several publications, TiO_2 conduction band edge (CBE) could be found at around -4.2 eV vs vacuum, while ZrO_2 CBE is -2.8 eV vs vacuum. [4, 103] According to computational TD-DFT calculations, the LUMO of the N719 may be anywhere between 0 to 1 eV higher in energy than the TiO_2 CBE.[100] In the literature, there are reports utilizing experimental data to estimate the energy difference between TiO_2 CBE and the dye LUMO level, and in some cases the gap is very close to 0.[104] In addition, one paper summarized UPS/XPS and UV-Vis spectroscopy results and found that there was a 0.25 eV barrier to electron injection from N719 into TiO_2.[105] These results were obtained in vacuum, hence the conditions are quite different from the devices investigated here. Hence even if one took the upper limit for the LUMO and the lower limit for ZrO_2, there's still 0.5 eV missing for the bands to align. Another possibility for an electron transfer to occur from an excited dye to ZrO_2 would be for the electron to get injected into a lower energy surface state. However, according to the experimental observations outlined above, this is not likely to have happened.

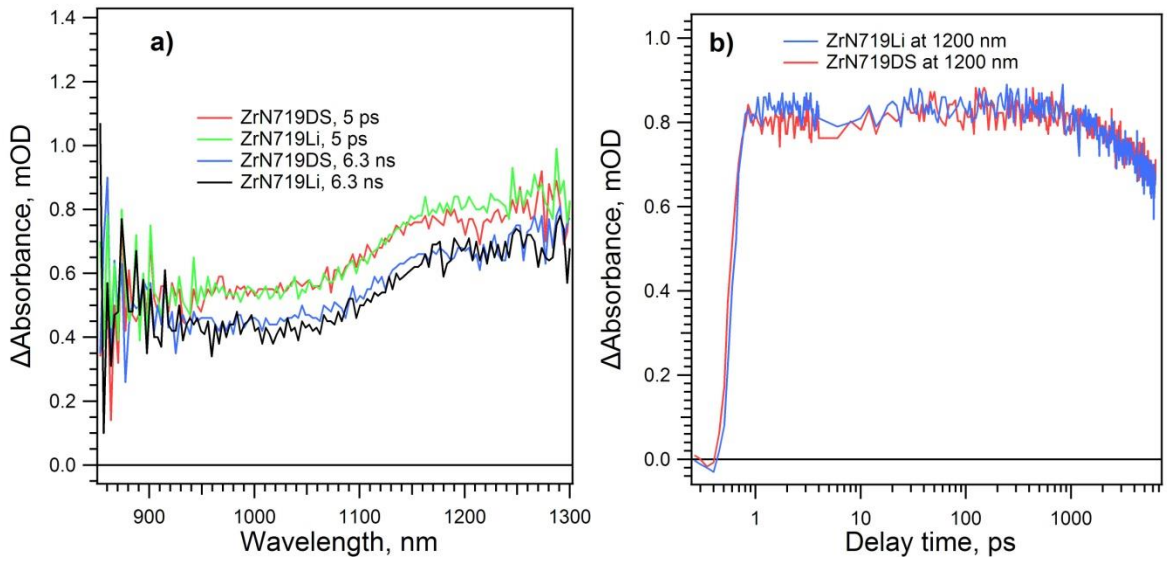


Figure 5.6. a) Transient absorption spectra of N719 on ZrO_2 in both DS and Li (0.5 M Li^+ added) electrolytes. The spectra is at 5 ps and at 6.3 ns delay after the excitation pulse. No difference in the two spectra is observed; b) decay of the transient absorption at 1200 nm probe wavelength. Samples were optically excited at 580 nm with energy of 48 μJ cm^{-2} per pulse.

Spectrum of N719 on TiO_2: electron injection

The early time (<1 ps) TAS of N719 on TiO_2 in both electrolytes (TiN719DS and TiN719Li) in Figure 5.7 is similar in magnitude and shape to the ZrO_2 data and covers the entire NIR region. It is asserted here that it is reasonable to assume it is mainly (> 50%) composed of the N719*. The transient

spectra of N719 on TiO_2 behave differently than those on ZrO_2, indicative of electron injection. The much faster decays in the NIR are attributed to electron injection. The spectra evolves over a broad timescale, starting from <100 fs (instrument response limited) to 6.5 ns. A major observation is the existence of an isosbestic point in the spectra at ~900 nm for the TiN719DS and at ~960 nm for TiN719Li. The isosbestic point is composed of balancing contributions from N719*, $N719^+$ and injected e-. The rising absorption at <900 nm occurs because $N719^+$ and e- absorption outweighs the falling N719* absorption in this area. The falling absorption at >900 nm occurs because N719+ does not absorb >1000 nm and e- absorption is smaller than N719* absorption. In the literature, researchers have often reported TAS at a single wavelength in the range 800 - 900 nm and concluded that >80% of injection occurs faster than 100 fs.[56, 71] However, as is clear from Figure 5.7, wavelengths around 900 nm have isosbestic character and cannot be used for reliable analysis of electron injection. In addition, one report has found that the $N719^+$ and N719* spectra may coincide completely for a particular sample in the wavelength range <900 nm.[52]

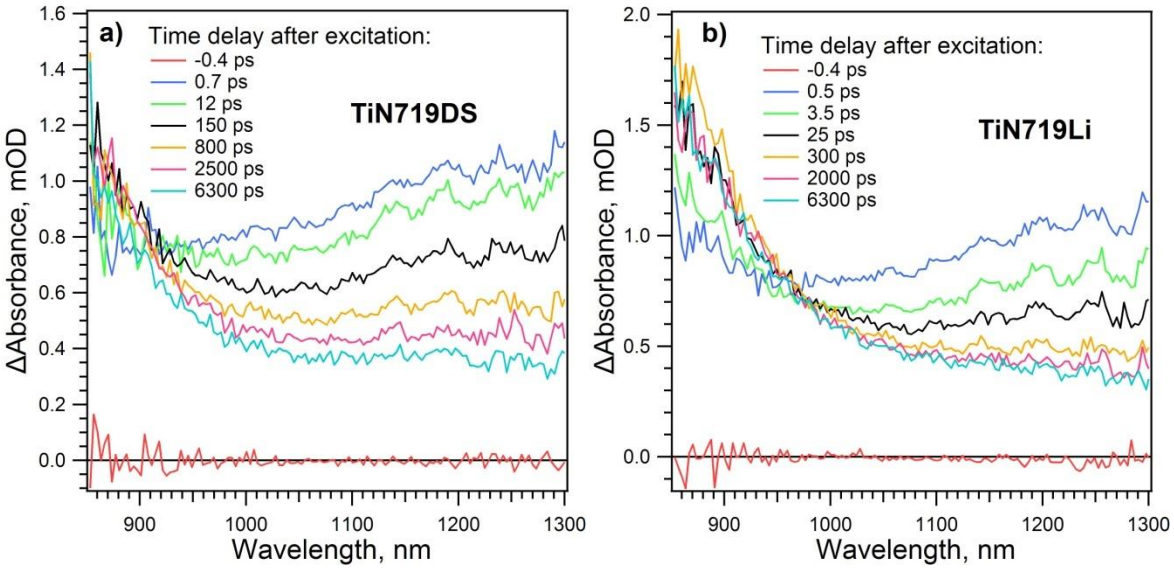


Figure 5.7. a) Transient absorption spectra of N719 on TiO_2 with DS electrolyte at different delay times after the excitation pulse; b) Transient absorption spectra of N719 on TiO_2 with Li electrolyte, where 0.5 M Li^+ was added. Devices were optically excited at 580 nm with energy of 55 μJ cm^{-2} per pulse.

The Vis/NIR kinetics of N719 on TiO_2

In the following sections, electron injection kinetics are discussed and quantified. Figure 5.8a shows the decay at 1200 nm probe wavelength. The signal decays with kinetics spanning a wide range of timescales. For instance, 150 ps after the excitation the TiN719DS absorption has decayed 50% of

the entire registered fall between 0.7 ps and 6.5 ns. For TiN719Li, the decay at 1200 nm is much faster and is nearly finished by 100 ps. The faster kinetics may be due to the Li^+ ions lowering the TiO_2 conduction band edge energy, which increases the rate of injection.[59] For comparison, mid-IR transient electron absorption rise signals at 5100 nm are overlaid on the decays at 1200 nm. In order to compare the two signals, the mid-IR data had to be inverted from rising to a falling signal and multiplied by a normalisation constant. The inversion and normalisation operations do not change the relative amplitudes and lifetimes of exponential fits and hence do not change the observed dynamics. The rise of the electron signal at 5100 nm matches the decay of the excited state kinetics at 1200 nm very well. From this data it is concluded that the decay in the NIR at >1100 nm can be used to get a general sense of injection kinetics. It is virtually impossible to use the Vis-NIR data to fully quantify the fraction of fs injection, as discussed below.

In Figure 5.8a, the absorption rise at 5100 nm before ~1 ps is the instrument response limited <100 fs measurement of electron injection. The data was already shown in Chapter 4 and was inverted for this Figure, to correspond to excited dye decay instead of electron injection. By contrast, in Figure 5.8b, at 900 nm for TiN719DS, an ultrafast rise is observed which has constant amplitude for 6.3 ns. This is due to the spectrum having an isosbestic point at 900 nm and should not be assigned to a <100 fs injection. The early rise at 900 nm for the TiN719Li sample is attributed to electron injection. It is possible to erroneously conclude that 75% of the injection is <100 fs and finishes at ~100 ps, consistent with the decay at 1200 nm. However, because the dye excited state and the photo-oxidized dye have similar extinction coefficients at this wavelength, the exact proportion of injection occurring on the femtosecond scale can be anywhere between 0% and 75%. This argument is supported by the mid-IR data in Figure 5.8a. The proportion of femtosecond injection is more reliable when determined from electron-only signals, i.e. as measured in the mid-IR. This way, no estimates of extinction coefficients and no excited state subtractions are required. The proportion of the femtosecond injection estimated from the mid-IR data is ~25% for the N719 dye in the DS electrolyte. In contrast, one could obtain 100% if only the 900 nm transient absorption was used instead.

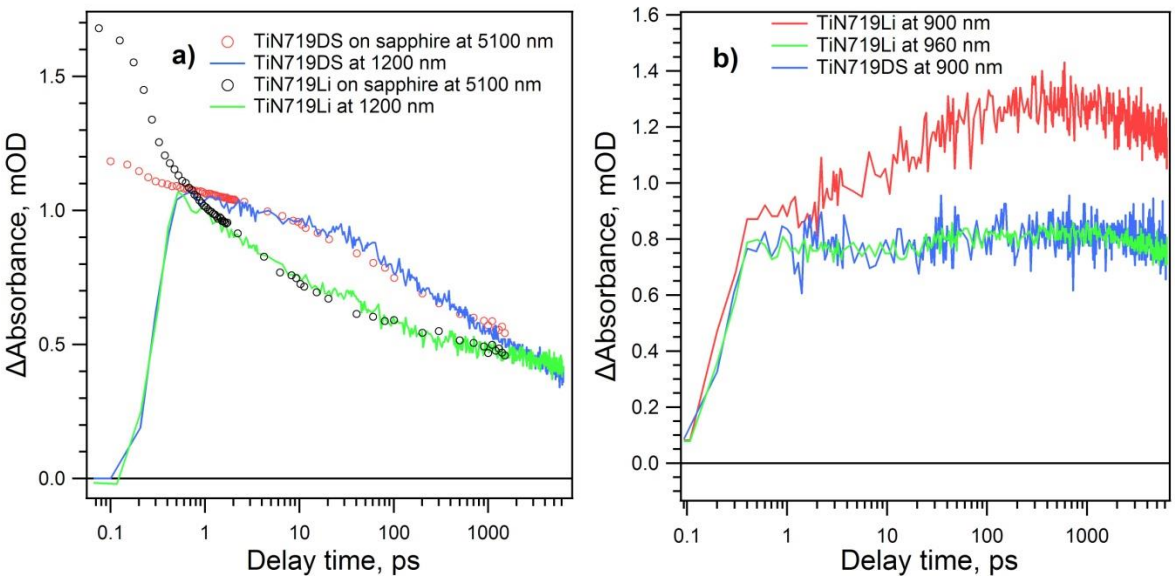


Figure 5.8. a) Time resolved kinetics of excited TiN719DS and TiN719Li devices. Overlaid are inverted and normalised data of identical devices prepared on sapphire instead of FTO coated glass and measured in the mid-IR at 5100 nm. The excited state decay kinetics at 1200 nm and the rise of the electron signal at 5100 nm are close; b) Transient absorption change at the isosbestic point of TiN719DS and TiN719Li devices. Kinetics of TiN719Li at 900 nm probe wavelength are also included to illustrate the difficulties of electron injection analysis in the Vis-NIR region. Pump pulse wavelength was 580 nm with energy of 55 μJ cm^{-2} per pulse.

In the following paragraphs the reasoning and quantitative analysis are outlined behind the spectral assignments above. A detailed analysis of the spectra in Figure 5.7 is also provided.

In Figure 5.7 at wavelengths longer than the isosbestic point the absorption change is much faster than the excited state relaxation observed on ZrO_2. These faster kinetics are attributed to electron injection into the TiO_2. Electrons in TiO_2 have a broad absorption range, from <850 nm to >1400 nm, overlapping with the N719 dye excited state absorption. With electron injection, a rise in the transient absorption amplitude is expected. The extinction coefficient for electrons in TiO_2 is in the range of 1000 – 2000 M^{-1} cm^{-1}.[96] We determined the extinction coefficient of the excited state of N719 on ZrO_2 to be ~5000 M^{-1} cm^{-1} at 1200 nm and 3650 M^{-1} cm^{-1} at 900 nm. Hence a decay is expected and observed at wavelengths longer than the isosbestic point. The excited state extinction coefficient calculation details are given in the following box:

Proportion of photons absorbed at 580 nm: $1 - 10^{-0.54}$ = ~70%
Total energy per pulse (homogeneous in the range 150 - 500 μm pulse diameter): 46-48 μJ cm^{-2}

Total amount of photons per pulse: $1.4 * 10^{14}$ cm^{-2}

Total amount of excited dye molecules: $1 * 10^{14} = 1.65 * 10^{-10}$ molecules cm^{-2}

Concentration of excited dye molecules: $2.75 * 10^{-4}$ M

Absorption amplitude at 1200 nm: $0.8 * 10^{-3}$

Extinction coefficient at 1200 nm = A / c / l = 0.0008 / 2.75e-4 / (6e-4) = 4850 M^{-1} cm^{-1}

Extinction coefficient at wavelengths 900 – 1000 nm = 3650 M^{-1} cm^{-1}

The spectra can now be decomposed to the main contributing components. The extinction coefficients for TiN719DS obtained below are in agreement with literature values. At the isosbestic point the extinction coefficient of the excited state of the dye must be identical to the sum of the extinction coefficients of the photo-oxidized dye and injected electron. Here it is assumed the extinction coefficient of the excited N719 is roughly the same on ZrO_2 as on TiO_2 when immersed in an identical redox electrolyte. At 900 nm, which is the isosbestic point of TiN719DS in Figure 5.7a, the extinction coefficient of 3650 M^{-1} cm^{-1} for the excited dye is used and a literature value of 1200 M^{-1} cm^{-1} for the electron. By subtraction, an extinction coefficient of 2450 M^{-1} cm^{-1} is obtained for the photo-oxidized N719 at 900 nm. Extinction coefficient at peak absorption wavelength can be inferred from its value at 900 nm. As reported in several papers, the peak absorption of the photo-oxidized N719 on TiO_2 is electrolyte dependent and varies between 830-860 nm.[23, 35, 50, 106, 107] The absorption coefficient at peak is roughly twice higher than at 900 nm. The estimated extinction coefficient of the photo-oxidized dye in TiN719DS device at peak absorption is thus ~4900 M^{-1} cm^{-1}. This is in agreement with several recent papers, where the photo-oxidized dye's absorption at peak wavelength was found to be 3-4 times higher than the electron absorption at 980 nm in similar devices.[96]

From the spectra above, it is clear that the photo-oxidized dye and the excited state of the dye absorption spectra may change significantly when in different chemical environments. The photo-oxidized N719 dye is known to absorb in the region of 700 – 900 nm, with the absorption maximum strongly dependent on the chemical environment of the dye. Not only the absorption maxima but also the extinction coefficient can vary due to different local dielectric environments in different solvents, solutes and the metal oxide used as a substrate. This variation is observed in many papers which measured a different absorption spectrum of the photo-oxidized N719 in different chemical environments.[23, 35, 50, 106, 107] This is well illustrated in Figures 5.6 and 5.7. The excited dye spectrum on ZrO_2 is almost identical in electrolytes with 0.5 M Li^+ and without. The same is not true when the dyes are on TiO_2, as illustrated in Figure 5.7, where a shift of 60 nm in the isosbestic point

is observed. It is not clear if the shift is due to changes in the excited state or photo-oxidized dye spectrum induced by lithium ions, or due to the dyes being attached to TiO_2 instead of ZrO_2, or both. If possible, the assumption that the extinction coefficients and the shape of the spectra can be transferred between different samples should be avoided when comparing TAS measurements.

It should be pointed out that ultrafast formation of an intermediate, charge-transfer state between the excited state of the dye and the TiO_2 is unlikely. The dye excited state spectrum on the TiO_2 matches closely the one on ZrO_2. In addition, the luminescence spectrum of the dye on TiO_2 matches the one on ZrO_2 without any significant shifting (<70 meV blue-shifted on TiO_2). If charge-transfer species are formed with ultrafast, <100 fs timescales, their spectra closely resembles the excited state spectra in solution and can thus be safely treated just as an excited state still mainly localized on the dye, and not as a charge-transfer state. After several nanoseconds, when electron injection is nearly finished, the spectra can be decomposed into the photo-oxidized dye and electron spectra in TiO_2. Hence even if an intermediate charge-transfer complex is formed, it is very short lived and decays into the dye excited state in <100 fs. This is also supported by the high dielectric coefficient of the TiO_2, which would render the energy of such a bound state to be very low. To conclude, here electron injection from the dye excited state to the TiO_2 without any observable intermediates was observed and the rising electron absorption in mid-IR is a direct measure of this process.

The Vis/NIR kinetics of C106 on TiO_2

To complement and corroborate the data for N719, TAS of devices sensitized with a similar ruthenium polypyridyl dye C106 was measured. The conclusions drawn from these measurements mirror those obtained for N719. The observed minor differences in the spectra of C106 from those with the N719 dye are outlined below without providing the same rigorous analysis as above.

Figure 5.9a is the transient absorption spectrum of the C106 dye on ZrO_2 in DS and Li electrolytes. In contrast to Figure 5.6a, the transient spectrum of ZrC106Li absorbs less in the range 900 – 1100 nm compared to ZrC106DS. The observed change may be due to C106 containing thiophene rings which are not present in N719. Lithium ions may coordinate to them, affecting the absorption. Figure 5.9b shows the decay signal at 1200 nm probe wavelength. A small, fast initial decay with <5 ps lifetime is observed. It may be due to the excited state thermalisation or reorganisation of solutes around the excited state. Otherwise the decays are consistent with the luminescence lifetime of C106 in the literature.

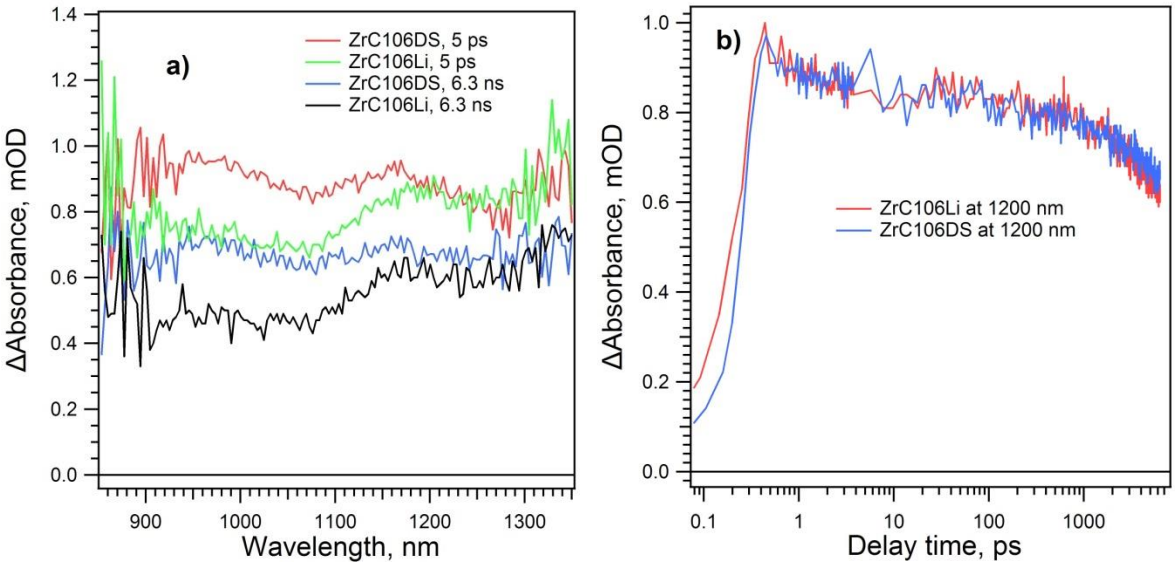


Figure 5.9. a) Transient absorption spectra of N719 on ZrO_2 in both DS and Li (0.5 M Li^+ added) electrolytes. Spectra shown is at 5 ps and at 6.3 ns delay after the excitation pulse. Spectrum in Li electrolyte has less absorption in the 900 – 1200 nm relative to >1200 nm; b) decay of the transient absorption at 1200 nm probe wavelength. Samples were optically excited at 580 nm with energy of 48 μJ cm^{-2} per pulse.

Transient absorption spectra of TiC106DS and TiC106Li are given in Figure 5.10. There is a clear isosbestic point in both graphs with a ~100 nm shifting upon addition of lithium ions. The initial early-time transient spectra in both devices are similar in shape and magnitude to the excited state of the dye. The spectra evolve similarly to the N719 and are indicative of electron injection. The photo-oxidized C106 absorption extends beyond 1000 nm with a decreasing absorption coefficient, in agreement with the literature.[108] However, the excited state has a higher extinction coefficient at NIR wavelengths than the photo-oxidized dye and the electron, hence decays are still observed at probe wavelengths longer than the isosbestic points. The injection analysis is identical to the N719 case. Injection occurs over a broad timescale of <100 fs to >1500 ps. With addition of lithium, the injection rate increases.

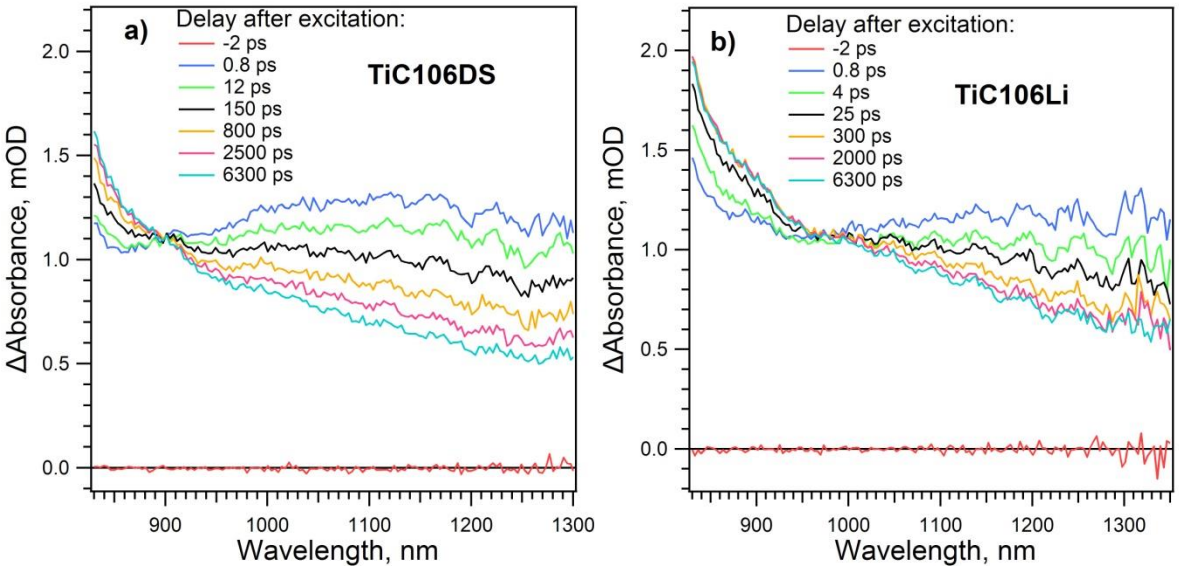


Figure 5.10. a) Transient absorption spectra of C106 on TiO_2 with DS electrolyte at various delay times after the excitation pulse; b) Transient absorption spectra of C106 on TiO_2 with Li electrolyte, where 0.5 M Li^+ was added. Devices were optically excited at 580 nm with energy of 55 μJ cm^{-2} per pulse.

Figure 5.11a shows the absorption change of TiC106DS probed at 1200 nm and attributed to the decay of the dye excited state. The signal matches closely the absorption rise observed in the mid-IR at 5100 nm of the TiC106DS device prepared on sapphire. TiC106Li decay at 1200 nm does not match as closely as the TiC106Li sample on sapphire as the mid-IR data stabilises after ~100 ps. The C106 solution used for Vis-NIR measurements was the same as used for the mid-IR measurements and may have been less acidic due to proton depletion than in the mid-IR measurements. The conduction band edge energy would not be pushed down as much for the vis-NIR measurements than for the mid-IR measurements. As for the N719 devices, Figure 5.11b illustrates that by analysing the injection at the isosbestic point one obtains a constant signal with an instantaneous rise. Interestingly, no real isosbestic point could be found for the TiC106Li sample. Although from Figure 5.10b it appears the isosbestic point should be in the range 950 – 980 nm, however, the decays at these wavelengths all had a ~1 ps fast ~10% decrease in the magnitude of absorption. It may be attributable to noise, or it may be the same process as observed on ZrO_2 at very early times after the excitation. It remains unclear what exactly the ~1 ps decay is, if not an ultrafast artefact. Adding lithium shifts the absorption spectrum of both $C106^+$ and C106* species and due to these changes, a small rise is observed at 900 nm. However, as stated previously, electron-only (e.g. mid-IR) data is required for reliable interpretation of the injection kinetics.

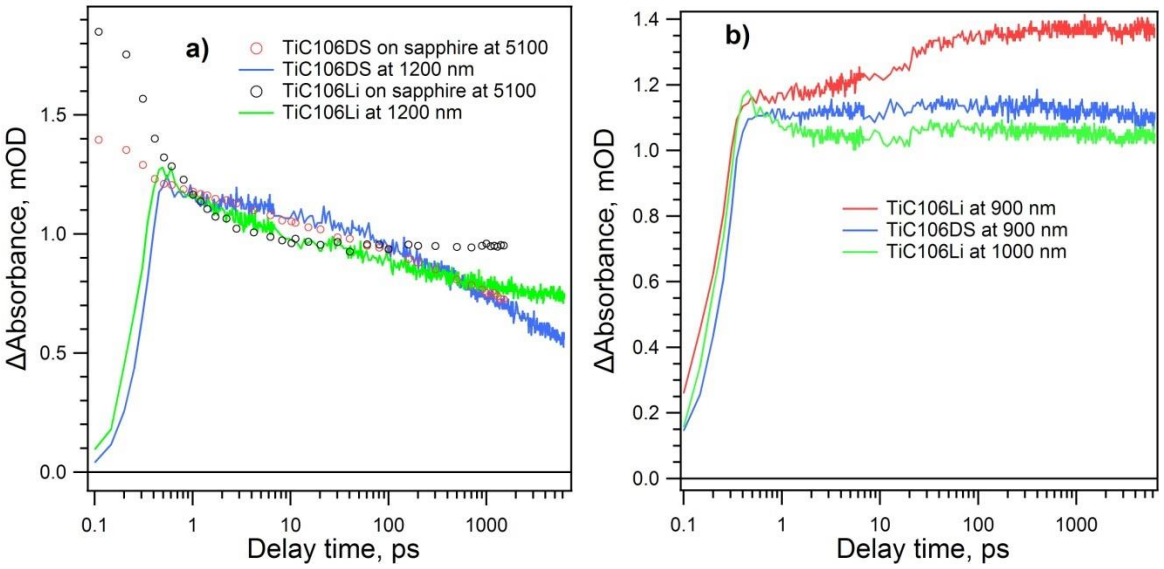


Figure 5.11. a) Transient absorption kinetics of excited TiC106DS and TiC106Li devices. Overlaid are inverted and normalised data of identical devices prepared on sapphire instead of FTO coated glass and measured in the mid-IR at 5100 nm. The excited state decay kinetics at 1200 nm and the rise of the electron signal at 5100 nm match closely for TiC106DS but only moderately for the TiC106Li device; b) Transient absorption change at the isosbestic point of TiN719DS and TiN719Li devices. Kinetics of TiC106Li at 900 nm probe wavelength are also included to illustrate the difficulties of electron injection analysis in the Vis-NIR region. Pump pulse wavelength was 580 nm with energy of 55 μJ cm^{-2} per pulse.

As a last point, it should be emphasized that even the relative injection yields are difficult to estimate between two different samples. This is because the magnitudes of the spectral shifts of the transient species are not easily quantified: different electrolytes affect the extinction coefficients of the dyes, making direct comparison between two absorption change magnitudes impossible. In addition, in the slower injection case, it is not clear if the injection is completely finished by 6.5 ns and if any excited dye contribution remains. This point is addressed in the next Chapter, where TCSPC data is incorporated into the discussion. Hence, in the Vis-NIR measurements, no suitable wavelength exists to compare the relative injection yields in the samples studied in the present Chapter. It is virtually impossible to get any reliable quantification of the injection utilizing only vis-NIR spectroscopy.

Conclusion

This Chapter provided additional evidence that electron injection in commercially relevant DSSCs occurs over a broad time scale: from fs to several ns. Of the multiphasic injection, the slowest component is close to the luminescence lifetime of the dyes studied here, showing that losses at the injection step, while theoretically small, could be big enough to warrant attention. In addition, the results presented here help explain the efficiency gap between record cells made from high volatility electrolytes and commercially relevant cells designed for stability, to last longer in terms of stability. As in previous Chapter, basic work relating to the ultrafast experiments was done. It was showed that the injection kinetics are not affected over a broad range of light intensities, the samples do not degrade or change over several hours of ultrafast, pulsed illumination and that short circuit or open circuit conditions do not affect the measured spectra or kinetics at all. Two dyes, N719 and C106 were utilized for the experiments and yielded close to identical conclusions. Finally, after careful quantification of the various absorption coefficients of the relevant species in the devices, and after comparing the results to the mid-IR range, it is evident that full quantitative analysis of the electron injection process in the vis/near-IR region is practically impossible. However, the vis/near-IR region does provide additional important information regarding the photophysics of the DSSCs but should always be used in combination with other spectroscopic methods.

Chapter 6. Electron injection mechanisms and efficiency

Introduction

Previous chapters focused mainly on spectroscopy and electron injection kinetics. In this chapter, a broader context for the spectroscopic findings is provided. Injection efficiency of six devices is derived from front-back IPCE measurements. The efficiency is then correlated to the femtosecond TAS results of the Chapters 4 and 5. The solar cells are measured with a time-resolved photon counting (TCSPC) equipment to obtain luminescence lifetimes and relative amount of luminescence between the samples. All the mid-IR TAS, VIS/NIR TAS, TCSPC, IPCE results and device efficiency measurements are collated and analysed as a whole. A complete picture of electron injection, as accurately as possible in light of all the results, is discussed.

Device details and absorption

Devices were based on mesoporous, nanocrystalline, 6.8 µm thick TiO_2 films. The films were sensitized with Ru-polypyridyl dyes, one of N719, Z907 or C106. They were filled with one of the two electrolytes, either the DS, or a Li electrolyte, composed of 0.8 M PMII, 50 mM I_2 and 0.5 M LiI in 3-methoxypropionitrile (MPN).

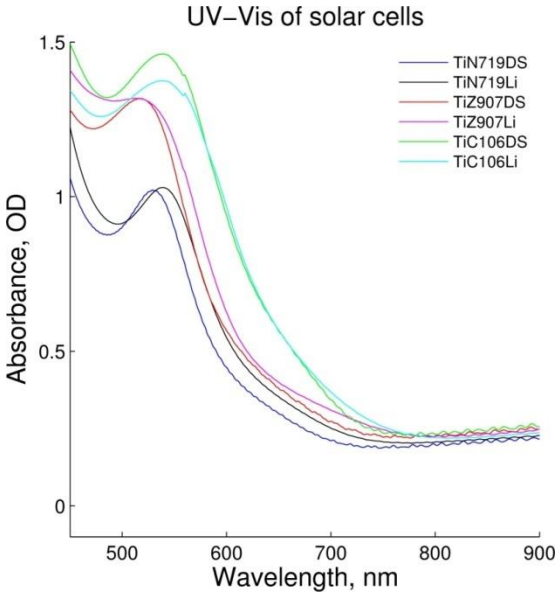


Figure 6.1. UV-Vis absorption spectra of the solar cells used throughout this chapter.

The UV-Vis absorption spectra of the DSSC devices which are discussed in this chapter are given in Figure 6.1. The spectrum is indicative of the Ru-bpy based dyes' spectrum. The addition of 0.5 M of

Li^+ to the electrolyte and omission of the benzimidazole base and GuSCN seems to affect the dye optical absorption. In particular, absorption of N719 is strongly red-shifted with the extinction coefficients unchanged. Z907 spectrum develops a shoulder to the red part of the spectrum without an obvious shift in the maximum absorption wavelength. On C106, there seems to be no red-shifting or additional shoulder, however, the extinction coefficient at maximum absorption seems to be increased by roughly 10%. The origin of these spectral shifts is unclear, but the shifting of dyes adsorbed on the TiO_2 surface upon acidification of the electrolyte is frequently observed in the literature.[86] The lithium ions can act as hydrogen ions and 'protonate' the carboxy acids of the dyes. This would remove some electron density form the bipyridines, stabilizing the system and hence redshift the absorption wavelengths, as observed in the spectra.

Very strong absorption is observed in the > 450 nm wavelengths due to the presence of I_2 in the electrolyte and the TiO_2 film itself. In addition, Ru-bpy dyes have a second strongly absorbing shoulder around 400 nm. The absorption quickly reaches > 3 below 450 nm and is therefore not displayed for clarity.

The absorption at NIR wavelengths, starting at > 750 nm, is due to reflected light from the air/glass, electrolyte/glass interfaces and light scattering due to TiO_2. As will be seen later, the absorption at > 750 nm does not contribute to the photocurrent. The wavy absorption seen at > 750 nm wavelengths is attributed to Mie scattering by the ~25 nm spherical TiO_2 particles.

Current-Voltage and device efficiencies

Current-Voltage (JV) curves have been recorded of all the devices under irradiation of simulated 1 sun (AM1.5G), i.e. power of 1 kW m^{-2} at AM1.5 spectrum. The curves are displayed in Figure 6.2.

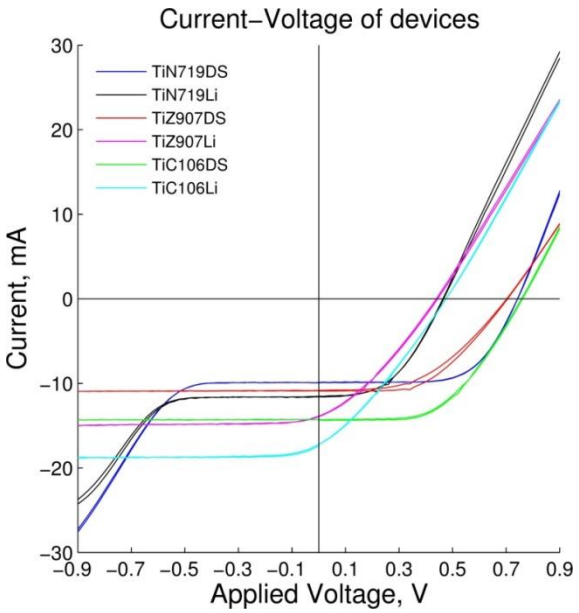


Figure 6.2. Current-voltage curves of the devices investigated in the current chapter, recorded under simulated 1 sun, AM1.5G irradiation.

Device JV curves in Figure 6.2 were analyzed and the solar cell efficiencies along with other parameters are outlined in Table 6.1.

Device	J_{sc}, mA cm^{-2}	V_{oc}, V	FF	η, %
TiN719DS	9.9	0.74	0.65	4.81
TiN719Li	11.6	0.46	0.49	2.64
TiZ907DS	10.9	0.70	0.52	4.00
TiZ907Li	14.8	0.44	0.32	1.97
TiC106DS	14.3	0.76	0.54	5.82
TiC106Li	18.8	0.48	0.30	2.50

Table 6.1. Solar cell parameters

An interesting observation stands out from the parameters given in Table 6.1. A significant increase in J_{sc} is observed after addition of lithium ions. The relative short-circuit current for the DS electrolyte compared to Li electrolyte is 85%, 74% and 76% for N719, Z907 and C106, respectively. However, the addition of lithium ions results in lower power conversion efficiency due to a significant reduction in V_{oc} and the fill factors for the devices. This effect can be roughly explained by a phenomenon that the conduction band edge energy of a metal oxide decreases upon addition of small, positive ions.[59] Both hydrogen and lithium ions are known to adsorb to the metal oxide surface, and due to the additional positive charging of the surface, the conduction and valence bands are shifted down in energy. This lowers the achievable V_{oc} of the solar cells, as the redox potential of the electrolyte doesn't change as much. In addition, the relative energy of the

conduction band edge to the LUMO of the dye molecule shifts down,[104] hence there is a larger downhill energy gap for electron injection. This larger energy gap may lead to faster electron injection kinetics due to reduced reorganization energy as per the Marcus electron transfer picture.

The lower J_{SC} for the DS electrolyte relative to Li electrolyte could not come from light harvesting, at least not for C106 and Z907 dyes, as the absorption changes are very minor, as pictured in Figure 6.1. Regeneration has been shown to occur with a quantum efficiency of unity for Ru-bpy dyes in electrolytes similar to DS. [97, 109] However, the most important argument for higher yield of injection will be outlined in the next sections.

Comparing the solar cell performance between dyes, C106 emerges as a champion dye. However, the solutions used to prepare the N719 devices were not as concentrated as initially prepared, hence lower dye loading in the N719 case occurred. Z907 and N719 have very close extinction coefficients hence it is reasonable to assume, from the absorption spectra in Figure 6.1, that there were somewhere between 10% to 20% less N719 dyes than Z907. However, in this Chapter, the amount of dye loading is not of material importance, as the focus is on injection efficiency and the loss mechanisms for injection. It was an oversight to manufacture the N719 cells not from freshly prepared solutions, which would have enabled additional comparisons between N719 and C106.

Photon to current conversion efficiency measurements

Incident photon to current conversion efficiencies (IPCE) were measured for all devices. The IPCE fraction represents the percentage of photons which are converted to measurable short-circuit current in the device. The IPCE fraction is given by the formula:

IPCE = LHE * IE * EC

Here LHE is light harvesting efficiency; IE is injection efficiency; EC is electron collection efficiency.

Light harvesting efficiency can be calculated by estimating the amount of photons absorbed by the dyes alone relative to total incident light. Data from steady-state UV-Vis absorption measurements can be used, however it has to be carefully adjusted, as the measurement includes all the light reflection and scattering, which is incorporated into the absorption measured. For the devices in this Chapter, fluorine-doped tin oxide (FTO) film coated glass was used as a substrate. In some cases, it was additionally coated with a TiO_2 spray thin film. A transmission spectrum for the two films is given in Figure 6.3.

Tin oxide has a refractive index of approximately 2, while air has 1. According to the Fresnel equation for refracted light at incident angle normal to the surface, approximately 10% of light will be reflected at the tin oxide – air interface. On the other hand, 3-methoxypropionitrile has a refractive index of 1.4 and only 3% of the light will be reflected at the FTO – MPN interface. To obtain the

amount of light reaching the dyes in the solar cell, it is reasonable to assume that 4% will be lost at the air-glass interface, 2% will be lost at the glass-FTO interface and 3% will be lost at the FTO-MPN interface. FTO itself absorbs up to 4% of the light. Hence, approximately 11%, within +- 2% of the light is lost to reflection and absorption of the FTO before it reaches the dyes adsorbed on the TiO_2. Amount of light lost will be additional 2-4% higher for devices with a TiO_2 spray layer. These numbers are in line with the observed absorption spectrum in Figure 6.3.

By doing a similar analysis, it was estimated that adding a platinum layer on an FTO, approximately 7% additional light is lost at the interfaces and due to absorption by the platinum.

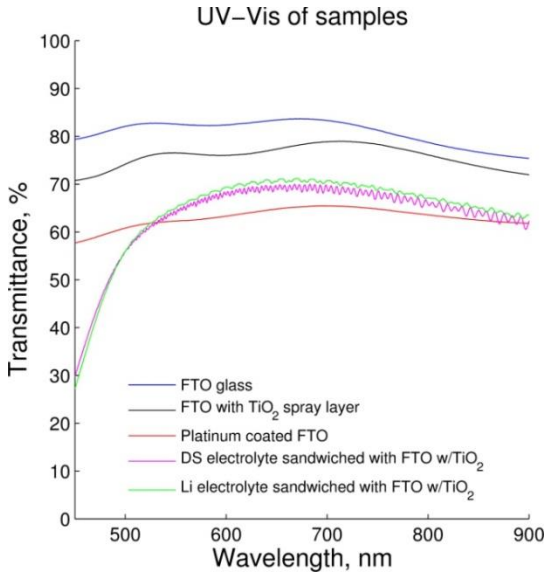


Figure 6.3. Transmittance measurements for the relevant substrates. The magenta and green lines are samples closely matching full solar cells but without the dye adsorbed and without the platinum coating on the counter electrode.

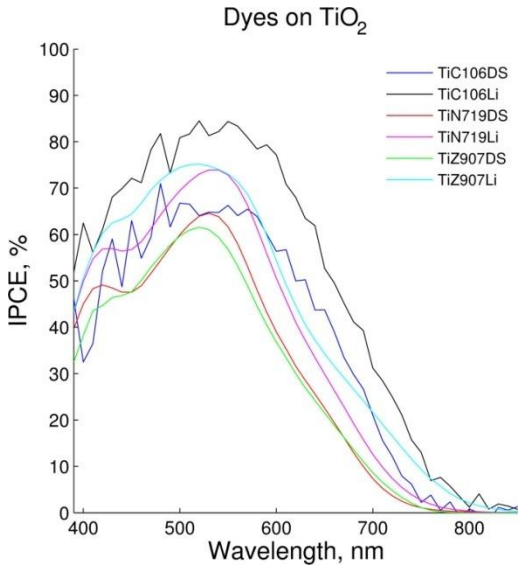


Figure 6.4. Incident photon to current conversion efficiencies (IPCE) of the devices studied in this Chapter. These IPCEs were obtained with a background white light of approximately 10% of a full sun, so the IPCE conditions are more close to actual operating conditions. The additional bias light is required because the light from the monochromator is very weak and the amount of electrons it produces in the TiO_2 is very small. When the electron density in TiO_2 is not big enough, the diffusion length of the electrons is too short to collect them without losses. Hence a bias light is required to bring the electron density in TiO_2 to a level where electron diffusion is fast enough to effectively compete with electron recombination.[58] On the other hand, illuminating the cell at one full sun may induce a small drift in the photocurrent in the device and in the time it takes to run the IPCE measurement over the entire wavelength range, the DSSC might change slightly and give less accurate values. The 10% of a full sun is a good compromise to bring the cell as close to operating conditions as possible.

IPCEs of all the devices are given in Figure 6.4. However, it is more interesting to consider the absorbed photon to current conversion efficiency (APCE). APCE can be obtained by dividing the IPCE by the fraction of incident photons absorbed by the dyes. First, the IPCE is divided by 89% to account for the 11% of photons which were reflected on the substrate side. It is then possible to obtain the fraction of incident light absorbed solely by the dyes by doing a simple subtraction. Two full, identical devices have to be measured except one has to be without the dye, the other with the dye. By simple subtracting no-dye sample absorption from the dye containing sample, the absorption solely due to the dye is obtained. This subtraction is correct assuming light reflection due to additional TiO_2/dye/electrolyte interface is minimal. The IPCE adjusted for reflected light has to be further adjusted for absorption by the dye. APCEs obtained with the method just described for all three dyes are given in Figure 6.5. This approach is subject to small uncertainty errors arising from experimental noise in the IPCE; from slightly overestimated dye absorption due to no Pt on FTO adjustment; from uncertainties in the reflected amount of photons. However, these errors are small and the APCEs thus obtained are expected to be quite reliable, within +- 0.03. In addition, for purposes of the current discussion, the absolute values are not as important as the relative magnitudes of the DS and Li electrolytes.

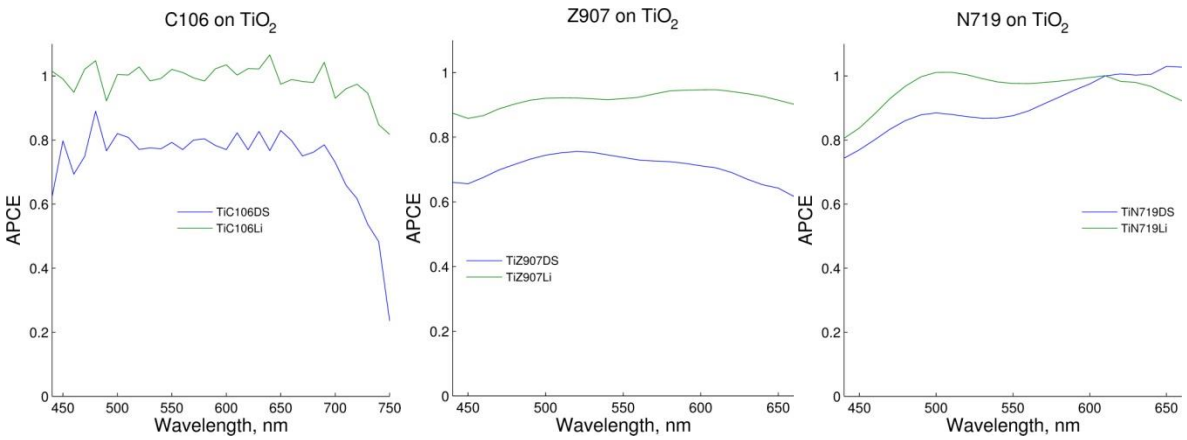


Figure 6.5. Absorbed photon to current efficiency measurements of the three dyes on TiO_2 in both DS and Li electrolytes. These figures are subject to higher errors at the blue and the red parts of the spectrum due to optical measurement uncertainty.

The APCEs for all three dyes are expected to be constant over the wavelengths where the dye absorbs, i.e. 450 – 700 nm. Some differences in APCEs arise at different wavelengths, but these arise from non-constant absorption of the FTO (blue line in Figure 6.3). In addition, at higher wavelengths, the uncertainty in the amount of light absorbed increases, as the amount of photons absorbed becomes less and comparable to the amount of photons lost to light reflection/scattering. Hence, due to subtraction, significant digits get reduced and the numbers become unreliable. This is not a problem for wavelengths where the dyes absorb strongly, with an extinction coefficient of > 1000 M^{-1} cm^{-1}. Interestingly, the APCE for TiN719DS seems to be increasing from 550 to 650 nm. Whether this is an experimental artefact or a genuine increase in efficiency is not clear. Comparing the UV-Vis absorption spectrum with the IPCE, it appears that the IPCE shape had a broadened FWHM compared to pure absorption spectrum, hence the increase from 550 to 650 nm observed in the APCE graph.

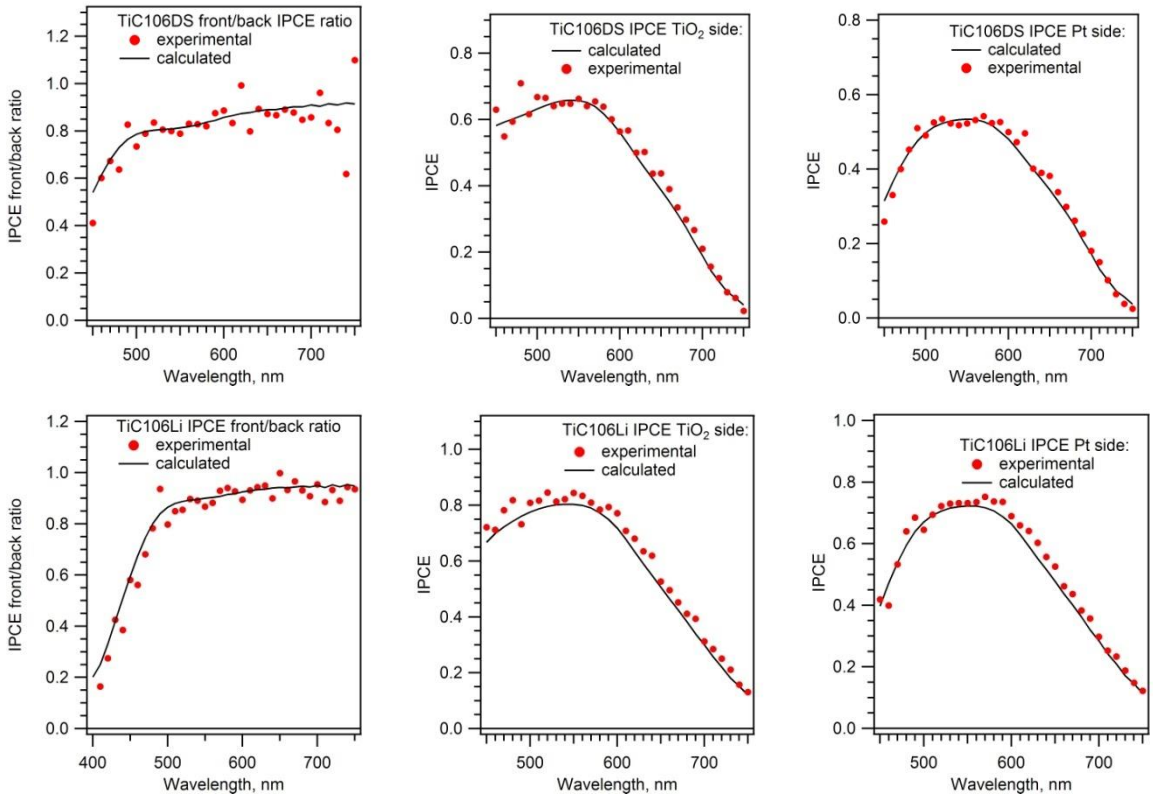
The APCEs are expected to be constant over all absorbing wavelengths if both electron injection and collection were wavelength-independent. This is the case for the C106 dye. However, TiZ907DS has a sloping down APCE at the red wavelengths. It is possibly due to collection losses: most of the photons at lower wavelengths are absorbed at the front electrode hence the electrons don't have to diffuse far to be collected. For the redder wavelengths, however, the injected electrons are distributed more uniformly and the average length an electron has to diffuse is longer. This approach to collection efficiency losses and injection efficiency estimation can be fully quantified if an additional IPCE is recorded with the counter electrode facing the incoming light. It is known as the

front/back IPCE method and is very well documented by Barnes et al. A brief description of the equations and methods are given in Chapter 3.

Only two fitting parameters need to be estimated to fit the experimental front/back IPCE curves. However, the equation which needs to be solved in the front/back IPCE method is highly non-linear with many local minima. A program was written in Igor Pro, where manual sliders could be used to fit the data and inspect visually how sensitive the fits are to a set of given parameters.

In all fitted samples, the incident light loss on the TiO_2 side was set to 11%, as before. For illumination from the back counter electrode, the amount of light loss was set to 18% to account for additional 7% loss due to the platinum thin film. The injection efficiency is assumed to be constant over all wavelengths. The IPCE front/back ratio is then computed and an electron diffusion length is chosen which gives the closest fit to the experimental data. Finally, injection efficiency is adjusted so that both, the front and the back IPCE curves are matched as closely as possible by the computed IPCE curves.

The IPCE and IPCE ratio graphs with the fits are displayed in Figure 6.6.



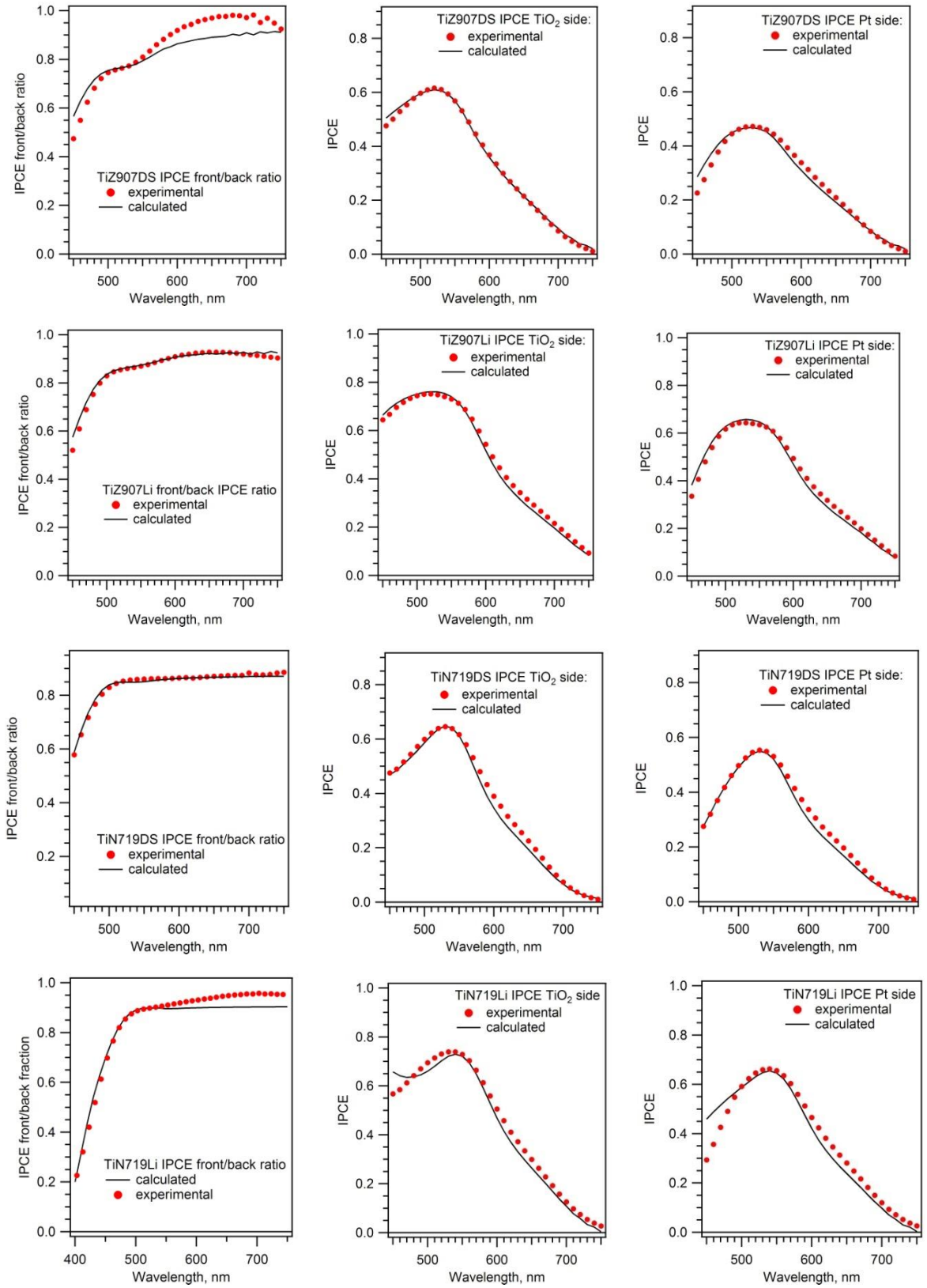


Figure 6.6. Red dots represent IPCE graphs recorded with illumination from front and from back electrodes separately. The graphs on the left are the front/back IPCE ratio obtained experimentally. Solid black lines are the best fits using the diffusion equation with appropriate boundary conditions as explained in Barnes et al.[58]

Fitting parameters and extreme fitting values are given in Table 6.2. The best fit parameters are the parameters that reproduce the graphs in Figure 6.6. In addition, a few extreme fitting parameter cases are given for illustration of the possible parameter range. To obtain the lowest possible diffusion length that still explains the front/back IPCE data, injection is assumed to be 100%. This is given under the column "η_{Inj} = 100%". The other extreme case is to assume the electron diffusion length to be infinite and find the injection efficiency which still satisfies the front/back IPCE graphs. This column is called "$D_L$infinite". Note that values entered in these two columns do not give satisfactory fits for the IPCE front/back ratio graph – these values are off by on average of at least 15%.

The diffusion length is interpreted as the distance an electron would travel without recombining with a ~64% probability (distributed normally). Hence the amount of electrons which would successfully reach an electrode x µm away without recombination is given by the equation:

$1 - \exp(-D_L/x)$

Assuming electrons are distributed uniformly in an electrode of length 6.8 µm, with a D_L of 9.5 µm (TiC106DS), which is the case when the solar cells are illuminated with the red light (~650 nm), the average amount of electrons that would reach the collecting FTO electrode would be ~91%. This number, together with the injection efficiency of 87% is in line with a roughly 80% APCE observed for the TiC106DS sample.

Device	Best fit	Assuming D_L infinite	Assuming η_{Inj} = 100%
TiC106DS	D_L = 9.5 µm, η_{Inj} = 87%	η_{Inj} = 77%	D_L = 6.5 µm
TiC106Li	D_L = 20 µm, η_{Inj} = 100%	η_{Inj} = 97%	D_L = 20 µm
TiZ907DS	D_L = 7.2 µm, η_{Inj} = 89%	η_{Inj} = 72%	D_L = 5.6 µm
TiZ907Li	D_L = 13 µm, η_{Inj} = 100%	η_{Inj} = 92%	D_L = 13 µm
TiN719DS	D_L = 20 µm, η_{Inj} = 90%	η_{Inj} = 87%	D_L = 10 µm
TiN719Li	D_L = 25 µm, η_{Inj} = 100%	η_{Inj} = 100%	D_L = 25 µm

Table 6.2. Parameters obtained from the front/back IPCE analysis.

From the above IPCE analysis, it is evident that the injection efficiency increases with addition of lithium ions. The stable electrolyte which is optimized for power conversion efficiency has roughly 10-15% of absorbed photons that were not injected into the TiO_2. The increase in injection efficiency upon addition of lithium ions can be explained by a lowering of the conduction band edge and hence higher injection yield due to a larger energy gap between the CBE and the dye molecule LUMO. As is evident from Table 6.2, the addition of lithium ions increases the diffusion length too. The reason for the increase in D_L is not clear. Overall, as is evident from the measured device J_{SC}, there is roughly

20% more short-circuit current coming out from devices containing lithium ions in the electrolytes, albeit the energy efficiency is reduced due to the lower open-circuit voltage and fill factors. The exact loss of current mechanisms in the high efficiency electrolyte devices will be discussed in the next sections.

Time-resolved Photoluminescence

Time-resolved single photon counting (TCSPC) equipment was utilized to measure the time-resolved photoluminescence of the solar cells. The TCSPC equipment had a fastest response time resolution of roughly 200 ps and can record decays lasting hundreds of nanoseconds. The dyes studied in this chapter are ruthenium based, which due to the heavy metal effect undergo inter-system crossing to a long-lived triplet state in less than 100 fs.[28] Triplets are known to be long-lived excited states and the phosphorescence usually occurs on the order of tens of nanoseconds to microseconds. When the dyes are on TiO_2, where they can undergo injection, any dyes that emit light indicate a failure to inject and the devices give lower photocurrents compared to less emitting solar cells.

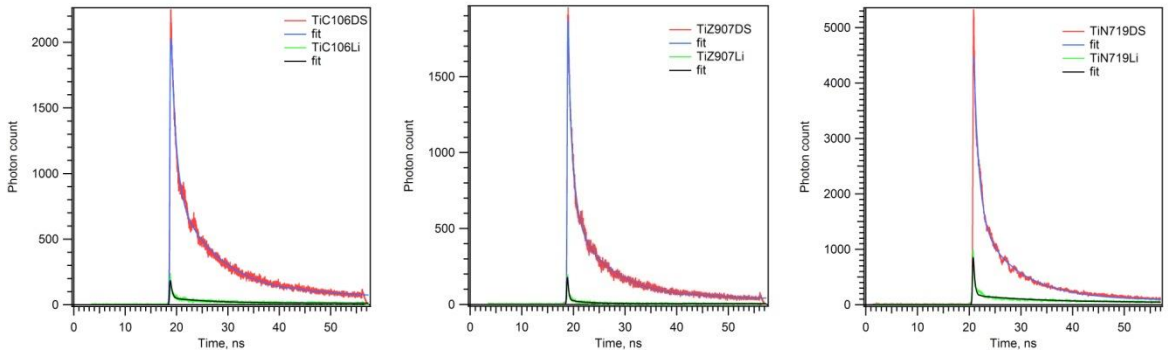


Figure 6.7. Time resolved single photon counting photoluminescence decays for the solar cells discussed in this chapter. Note the different timescale for the N719 dye. The double/triple exponential fits were convoluted with the instrument response function. Details are given in Chapter 3. Dyes were excited at 467 nm and the luminescence collected at 750 nm.

Figure 6.7 illustrates photoluminescence decays for the devices considered in the present chapter. All TCSPC measurements were run for a fixed amount of time, stopping the experiment once the time elapses. This way, the samples with the same dye are comparable in terms of total light absorption and luminescence. The graphs should not be compared between dyes, as to derive injection efficiency as per [59], very careful control samples have to be prepared. Such control samples are not available for the present analysis. However, comparing the DS and Li electrolytes, it is clear that the amount of photons collected for the cells with Li electrolyte is less than 5% of what

was collected for the cells with DS electrolytes in the same amount of time. This is in line with the IPCE front/back analysis, where injection efficiency for the Li devices was found to be very close to unity. In devices with Li electrolyte, if there were dyes which did not inject but underwent luminescence instead, it would have showed up in the present Figure as a higher number of total collected photons.

The fact that cells with DS electrolyte shows photoluminescence is indicative of electron injection which does not proceed with 100% efficiency. The exact efficiency is impossible to determine without additional reference or reliable photophysical parameters of the dyes on metal oxides.

Overlaid on the graphs are curves obtained by fitting the data with either a triple or a double exponential functions. The best fits in terms of lowest sum of squared error were obtained by an iterative procedure and the final fits were reconvoluted with the instrument response function. The decays could not be fit satisfactorily by a single exponential function, indicating a non-trivial photoluminescence and injection process. The fits to the Li electrolyte data were on the borderline with the instrument response time and are not useful for quantitative analysis. The fitting parameters for the samples with the DS electrolytes are given in Table 6.3. Note that the triple exponential function is highly non-linear and the fitting parameters are strongly correlated which results in a minimization of a loss function with many local minima. The parameters obtained, even though representative of a global minima, are only indicative of the overall kinetics. In addition, it is not clear if there is any physical explanation for why the decay kinetics should be composed of a triple exponential function. To get a more intuitive fit, the data within the instrument response time was ignored and only longer-lived kinetics were used, fitting the data with a double exponential function. Results are given in Table 6.4. This way, the fitting is less prone to errors due to parameter correlation and the obtained parameters can be more reliably compared between the samples.

Device	Decay param 1	Decay param 2	Decay param 3
TiC106DS	7%, 1 ns	59%, 0.9 ns	34%, 9 ns
TiZ907DS	47%, < 200 ps	36%, 1 ns	17%, 7.8 ns
TiN719DS	56%, < 200 ps	31%, 1.8 ns	13%, 12 ns

Table 6.3. Triple exponential decay parameters with instrument response function convolution

Device	Decay param 1	Decay param 2
TiC106DS	50%, 0.8 ns	50%, 8 ns
TiZ907DS	58%, 0.85 ns	42%, 7 ns
TiN719DS	65%, 1 ns	35%, 8 ns

Table 6.4. Double exponential fits ignoring data within instrument response time region

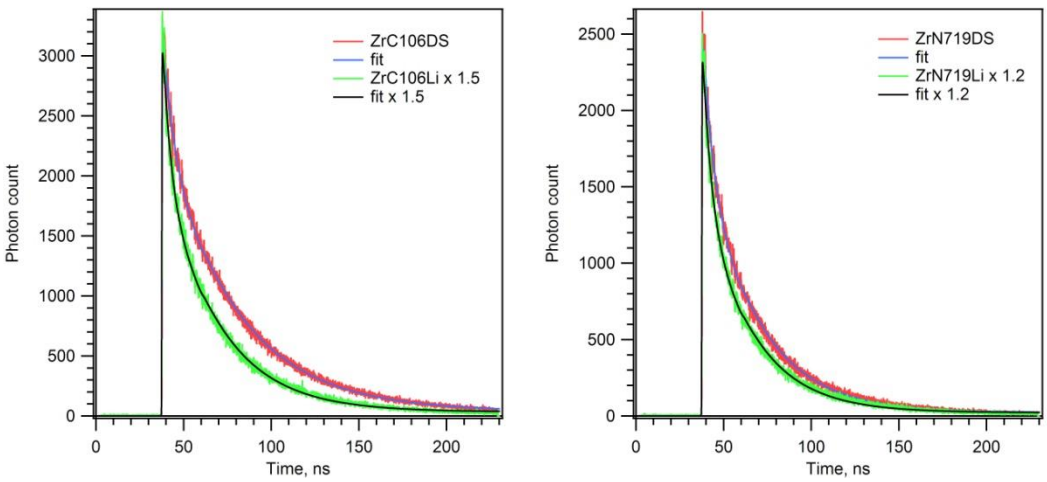


Figure 6.8. Time resolved luminescence decays with reconvoluted fits for C106 on ZrO_2 (left) and N719 on ZrO_2 (right). The Li samples were multiplied by 1.5 and 1.2 to match peak intensities, respectively. The Li samples show faster decay kinetics with less total photoluminescence.

ZrC106DS	30% 5.8 ns	70% 40 ns.
ZrC106Li	38% 4.3 ns	62% 31 ns
ZrN719DS	35% 5.4 ns	65% 30 ns
ZrN719Li	42% 4.6 ns	58% 27 ns

Table 6.5. Fitting parameters of time resolved photoluminescence of the zirconia samples.

The C106 and N719 dyes adsorbed on ZrO_2 substrate immersed in either DS or Li electrolytes were also measured using the TCSPC equipment. The photoluminescence decay traces are depicted in Figure 6.8. The fitting parameters of a double exponential function are provided in Table 6.5. The samples with Li electrolyte were multiplied by a constant factor to normalize for the peak of the signal. This way, the differences in decay kinetics are more visually clear. In both cases, changing the electrolyte from DS to Li reduced the average lifetimes of the excited dyes by roughly 50%. This change in lifetimes is not entirely unexpected: changing the electrolyte from DS to Li introduced visible spectral changes in the ultrafast TAS, as outlined in Chapter 5. Even for non-injecting samples, the data could not be fit with a single exponential function, implying a non-trivial luminescence process. The data on ZrO_2 is depicted only for rough comparison with the data on TiO_2. On ZrO_2, from Figure 6.8, the excited dyes decay roughly 10% in the first 1 ns. This amount of decay is correct assuming there is no decay component faster than the instrument response time of roughly 200 ps. This is reasonable to assume because the ultra-fast TAS of dyes on ZrO_2 showed almost no decay in the first 200 ps. Fluorescence might occur from the singlet state, but that would have to happen in < 100 fs, which was not possible to measure with the current equipment.

Ultrafast pump-probe spectroscopy in the mid-IR

As discussed in previous chapters, injection kinetics can be monitored using mid-IR pump-probe spectroscopy. The rise of the absorption change in the mid-IR corresponds to the appearance of an electron in the metal oxide. Figure 6.9 illustrates the injection kinetics of the relevant devices.

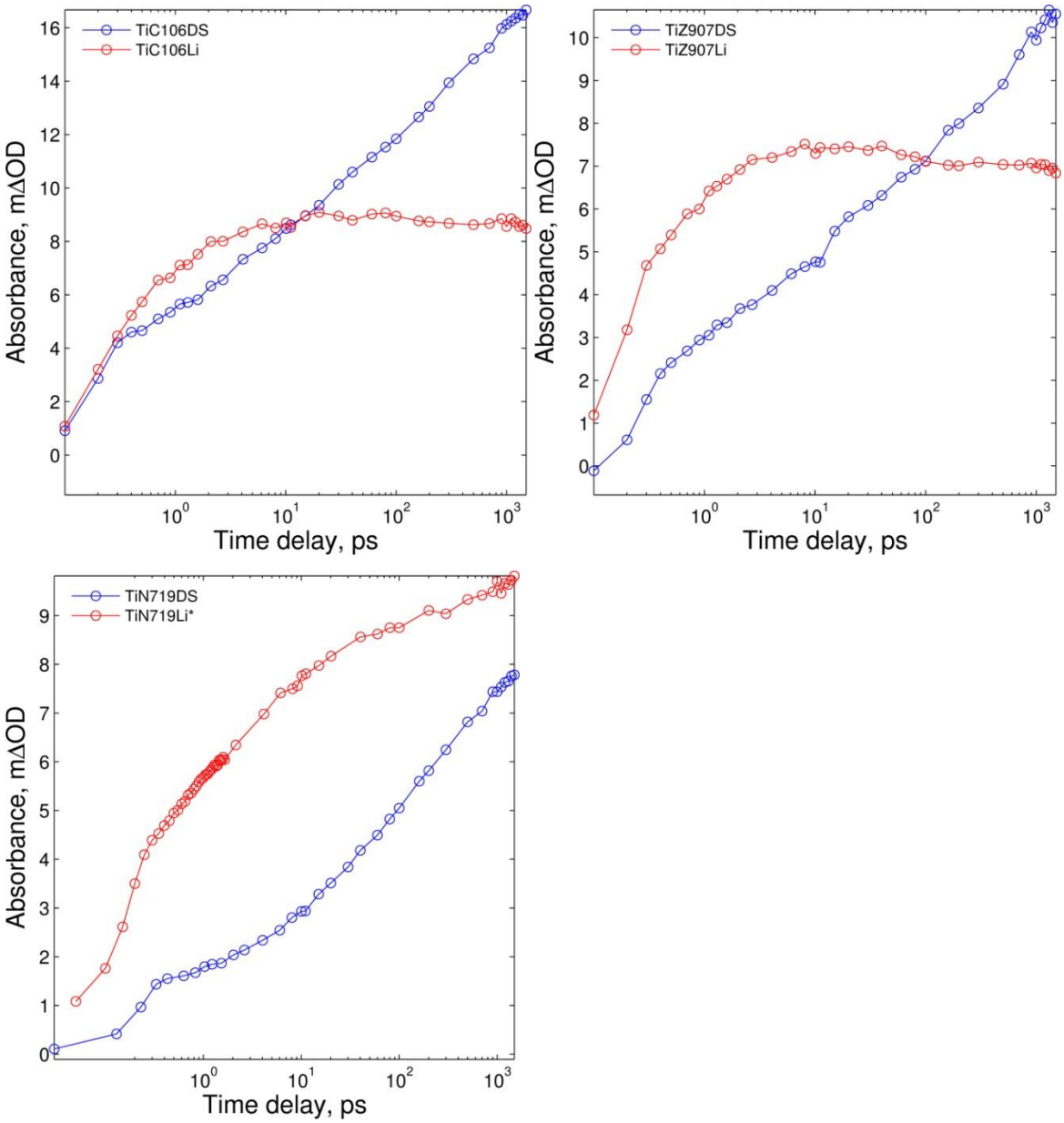


Figure 6.9. Transient absorption kinetics of the C106, Z907 and N719 dyes on TiO_2 with either DS or Li electrolytes. In case of N719, the Li electrolyte data was not available, however, another electrolyte, containing 0.1 M Li^+ ions was used. The absolute signal amplitude was multiplied by a factor of 2 for TiZ907Li to aid visual inspection. All samples were pumped at different light intensities

hence the absolute signal amplitudes are not comparable. Only difference in kinetics between DS and Li are of importance.

Evidently from Figure 6.9, addition of lithium ions to the electrolyte renders the injection kinetics faster by several orders of magnitude. The absolute value of the injected electron signal is not comparable between devices due to measurement differences arising from putting the device at a different spot, different laser power and variations in device thickness. However, for analysis of kinetics, the graphs in Figure 6.9 are sufficient. For Li electrolytes, the injection is finished in 10 ps for both C106 and Z907 electrolytes. In the case of N719, 80% of injection is finished in 10 ps. The difference in the kinetics of N719 compared to C106 and Z907 samples is attributed to a different electrolyte used, which had only 0.1 M lithium ions and no base in the N719 case instead of 0.5 M as in Li electrolyte.

Discussion of electron injection

The different measurements provided so far are all quite consistent. Important observations are highlighted here. From the IPCE front/back and APCE measurements it was inferred that solar cells prepared with 0.5 M lithium ions have close to 100% injection efficiency. As expected, these devices did not show measurable photoluminescence, shown in Figure 6.7. From Figure 6.9 it is clear that electron injection is finished in tens of picoseconds for the Li electrolyte devices and no excited dyes are able to decay radiatively or non-radiatively. In addition, the luminescence lifetimes of the dyes on ZrO_2 in DS/Li electrolytes were on the order of tens of nanoseconds, given in Table 6.5. Therefore, the photoluminescence of the excited dyes is much slower than the ultrafast injection observed in the case of Li electrolytes. In contrast, the DS electrolyte has at least 30% of the entire electron injection occurring at times longer than 100 ps after optical excitation. On ZrO_2, from Figure 6.8, the excited dyes decay less than 10% in the first 1ns. Hence, there is some room for potential loss of electron injection to radiative/non-radiative decay pathways of the excited dyes.

The kinetics observed in this and the previous chapters are all non-exponential. The kinetics can be represented mathematically by a multi-component exponential or by a stretched exponential formula. To decide which formula might be more physically meaningful is, however, very difficult. The origins of the non-exponential kinetics are numerous. For example, differences in the mode of dye adsorption on TiO_2, different TiO_2 surfaces, dye to dye interactions via hydrogen bonding may all contribute to the differences in chemical environments of the dye and hence influence the electronic interactions involved in electron injection and excited state decay. Most observed kinetics

can be satisfactorily fit starting with at least 2 exponential components, but in the electron injection case, at least 3 are required. It is hence more intuitive to analyze the injection kinetics and losses in purely observational manner, as opposed to model-based analysis, as is attempted in the section below.

Figure 6.10 is a graph showing electron injection tracked with pump-probe system in the mid-IR, overlaid on the electron signal and excited state probed at 1200 nm and on photoluminescence data obtained with a TCSPC equipment at 750 nm. The data has been normalized as follows. The TCSPC signal peak was reset to represent time-zero by removing the rise of the signal. It was then multiplied by an appropriate factor to match the amplitude of the TAS data. The TAS data was offset down by a constant factor, to match the TCSPC data, which decays to 0 in amplitude. If such an offset was not applied, the TAS data would never reach zero, because after all the dye excited states have decayed, electron signal still remains. By offsetting down by a constant number, the electron signal is effectively removed. As explained in the previous Chapter, such normalizations are justified, as the effective kinetic constants are not affected. These normalizations simply account for different extinction coefficients and different light intensities.

To aid intuition, the entire graph in Figure 6.10 can be interpreted as a single curve representing the dye excited state. Hence, just before any injection occurs, there is 0.9 of dye excited state, which decays down to 0.1 in the next 6 ns. The final 11% of the initial peak decays over roughly 50 ns. It is physically unlikely that injection would simply “stop” after 6 ns. A more likely scenario is that there is a very slow, with a lifetime of > 2 ns, electron injection component, which competes with the natural excited state decay. Up to around 1 ns there is effectively lossless injection and after that, injection losses occur due to ineffective competition between the loss pathways and injection itself. It is interesting to note that roughly 50% of the excited dyes inject before the TCSPC equipment starts registering the excited state decay. This proportion is true for both, TiN719DS and TiC106DS devices.

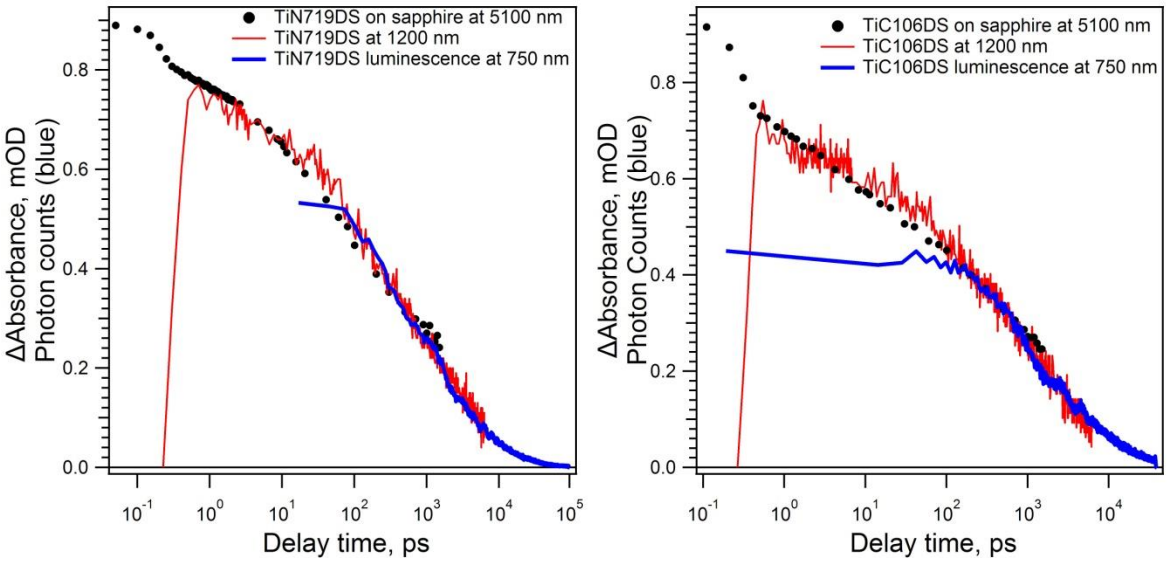


Figure 6.10. Graphs illustrating full concatenation, after adjusting for different extinction coefficients and light intensities, of ultrafast TAS in the mid-IR and near-IR regions. In addition, TCSPC data is overlaid. The combined curve should be interpreted as the overall decay of the dye excited state after optical excitation.

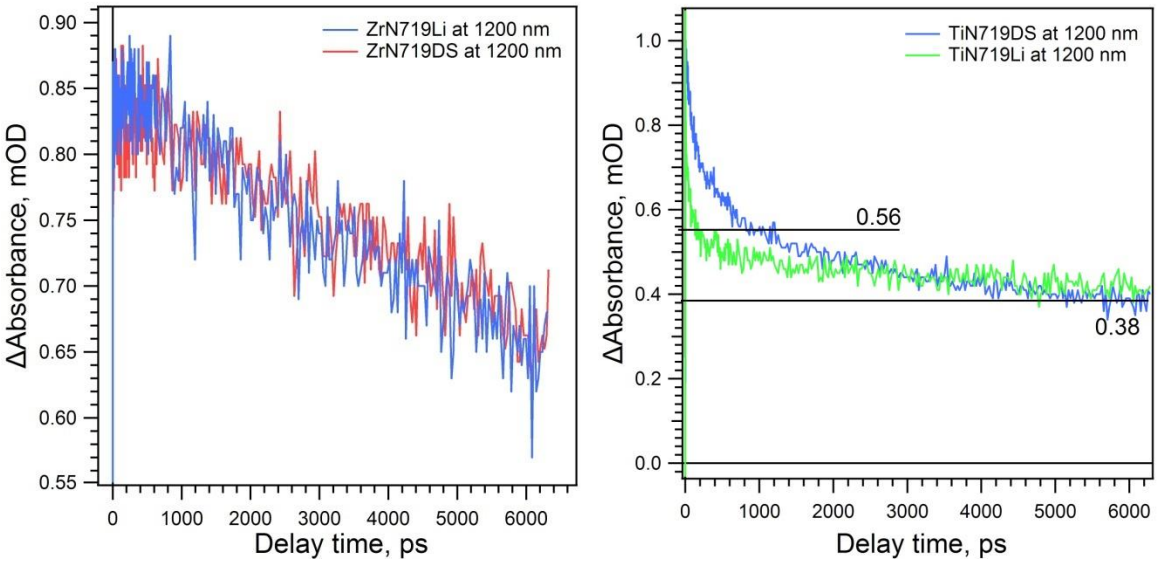


Figure 6.11. Ultrafast TAS of N719 on zirconia and titania in DS and Li electrolytes. On zirconia, virtually no decay before 1 ns occurs. On titania, the decays are much faster.

When the N719/C106 dye is on ZrO_2, negligible excited state decay occurs up to 500 ps, indicated in Figure 6.11. The entire decay of the dye on TiO_2 up to 500 ps is hence attributed to electron injection. From Figure 6.10, it is clear that roughly 25% of the initial ultrafast signal is not observed in the near-IR, 1200 nm TAS. In addition, concatenating the TCSPC data to the TAS data, a roughly 10-15% of the initial excited state concentration still exists ~6 ns after light excitation. Whether these are non-injecting dyes or simply very slowly injecting dyes is difficult to say. An additional

experiment is needed, where only the electron signal would be tracked with a delay line of at least 6 ns. If the electron signal would saturate in 1-2 ns, it would be clear that the remaining excited states decay without injecting. Such equipment was not available at the time of the PhD, unfortunately. Some additional inference can be made. Because only around 10% injection losses occur in the DS electrolyte, and roughly 25% of the excited states are still available after 1 ns (it can also be observed in Figure 6.7), electron injection must be continuing, with a very slow injection rate. In addition, in the first 6 nanoseconds, around 35% of the excited states decay on non-injecting ZrO_2 (Figure 6.8), implying there will be non-zero losses as the dyes continue to inject after 1 ns, where more than 30% of excited dyes are still remaining after initial fast injection. All these observations support the hypothesis that a fraction of the electrons are getting injected with very slow, several nanosecond rate. The alternative hypothesis that there exist non-injecting dyes seems less plausible in light of this discussion.

It is worth noting that very similar results in terms of electron injection dynamics have been recently obtained by another group.[87] There they combined photoexcited emission measurements, TAS in the mid-IR and in the visible domains. The systems that were studied in that paper are very similar to the ones presented herein and their results are effectively confirmed in this and previous Chapters: the slow, > 100 ps injection components were observed and attributed to slow injection.

Temperature dependence of electron injection

An important observation in DSSC devices utilizing ruthenium polypyridyl dyes with non-viscous solvents (MPN included) is that the short circuit current does not change over a broad temperature range, from 0 to 70 ^{o}C. Two devices, one utilizing the N719 dye, the other a thiocyanate-free T51 were used for this study. The absence of change in the short circuit current implies that the injection efficiency is not affected by the temperature.

The TiN719DS device (4.4 µm thick, Li-21 TiO2 paste, 0.81 cm2 area, N719 dye) used for the temperature dependent studies was an old device, which was prepared 2 years before the TCSPC measurements. The injection yield is known to go down with the age of the device. The short circuit current decreased from 9.6 mA cm^{-2} when the cell was prepared to 6.5 mA cm^{-2} over the 2 year period but was still constant in the temperature range 0 – 70 ^{o}C.

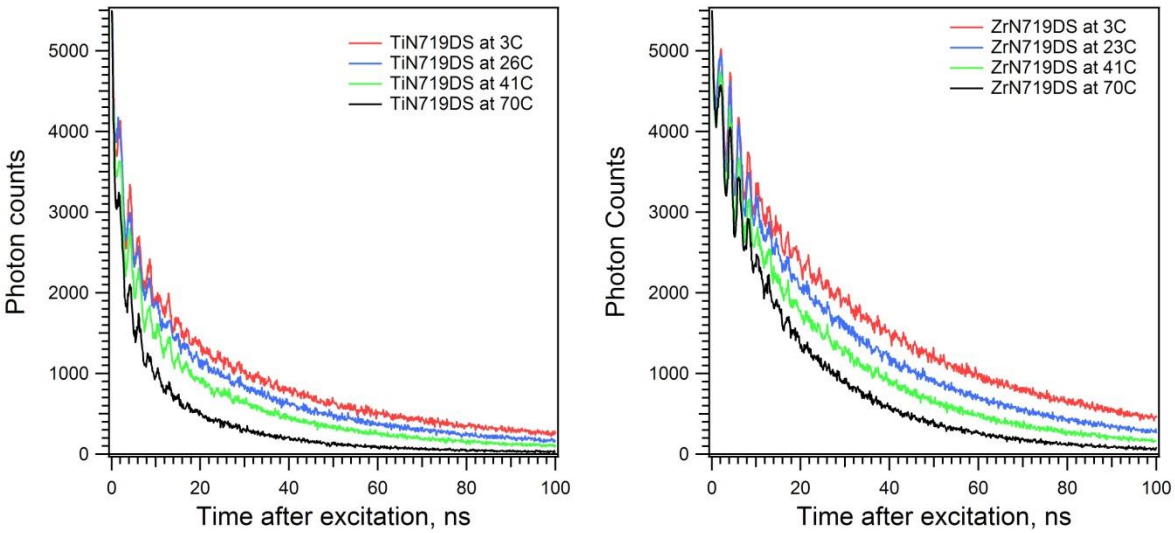


Figure 6.12. Temperature dependent luminescence of the N719 dye on either TiO_2 or ZrO_2 metal oxides immersed in the DS electrolyte. Luminescence decays were recorded until the peak of the decay signal reached 5500 photon counts.

A thiocyanate free ruthenium dye T51 was also used for temperature dependent studies. Solar cells made with T51 show very low short circuit currents of 1 mA cm^{-2}. In this case, an additional method for estimating injection efficiency was used. A non-injecting reference of the T51 dye on ZrO_2 was prepared, that had a matched optical density of the T51 dye on TiO_2. ZrO_2 film of thickness of 5.5 µm was used and TiO_2 thickness was 6.8 µm. Both sensitized films had very similar optical densities at 467 nm excitation wavelength. Additional error is introduced due to different scattering of the TiO_2 and ZrO_2 films. The observed injection efficiency of 66% does not account for the low J_{SC}, however the thiocyanate free ruthenium dyes usually have regeneration/recombination issues and hence reduced electron diffusion length. To support the latter claim, a device prepared on a 2.6 µm thick TiO_2 film with the T51 dye, with matched optical density had a J_{SC} of 1.4 mA cm^{-2}, 40% higher than the measured device which was 6.8 µm thick. But the important fact for the present section is the constant short circuit current at different temperatures for the T51 dye, which implies constant injection efficiency. As optical densities of these solar cells were closely matched and SPC was recorded so that all samples were subjected to the same amount of excitation photons, the areas under the curves in Figure 6 can be compared to give an injection yield. Such analysis gave ~66% injection yield at all temperatures.

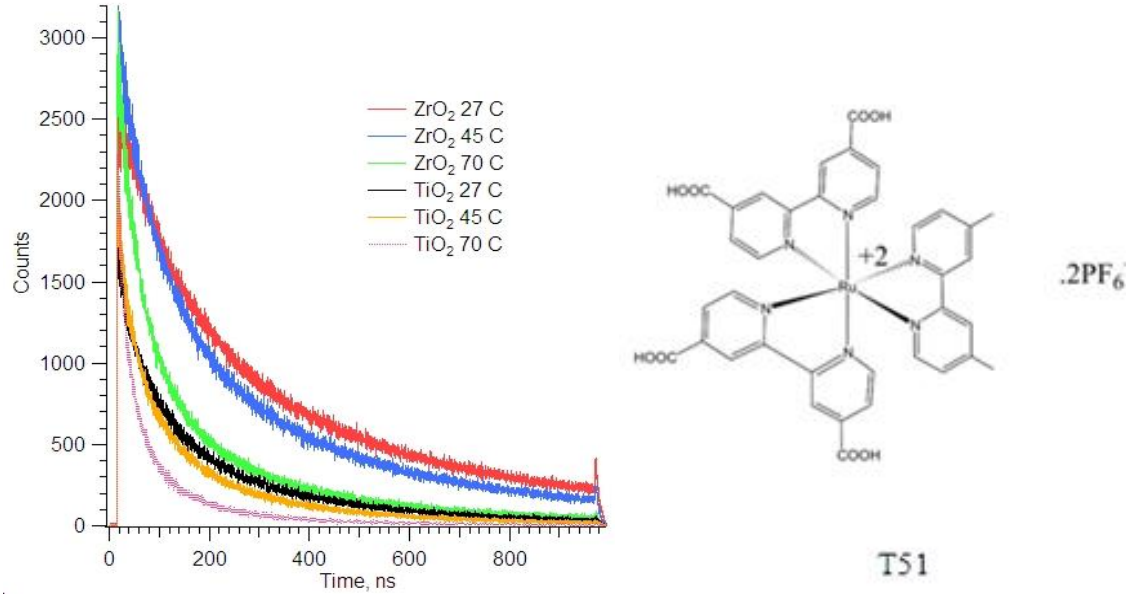


Figure 6.13. Temperature dependent luminescence decays of the T51 sensitized TiO_2 and ZrO_2 devices in a DS electrolyte.

The luminescence lifetime of the dye on non-injecting ZrO_2 decreases with increasing temperature. The increase in the rate of the excited state decay implies that there is a thermally activated step for the dye to return to the ground state from the excited state. It has been suggested that in order for the excited state to relax after the optically induced metal to ligand charge transfer, the electron has to be promoted from the π-orbitals of the bipyridine ligands to the d-orbitals of the Ru metal. The energy gap for the bipyridine Ru metal complexes is around a few hundred meV.[110] However, it may as well be that the activation energy for injection and excited state decay accidentally coincides with the energy required for an electron to be promoted to the d-d states of the Ru metal complex. The observation that the injection efficiency was constant over all measured temperatures implies that electron injection speeds up the same amount as the non-injecting excited state decay pathways. These observations imply that electron injection proceeds through thermally activated step from the triplet state, just as in the non-injecting excited state decay pathway.

Conclusion

In this Chapter, front/back IPCE measurements were done and injection efficiencies of DSSCs estimated. Efficiencies were obtained for N719, C106, Z907 dyes in either DS or Li electrolytes. Time-resolved photoluminescence was then correlated to the ultrafast TAS results from previous two Chapters. All the data fit together very reliably. In optimized solar cells (e.g. those utilizing the DS electrolyte) with a high V_{OC}, there a much slower injection component was found, with a lifetime of >

2 ns, which cannot be observed with most ultrafast TAS setups because the delay lines are usually of shorter length. Injection efficiency was negatively impacted by the presence of the slow component. This slow component was absent in devices where the conduction band edge is shifted downwards in energy relative to the dye LUMO, for example in devices with additional lithium ions added. These devices have a higher injection yield. However, such speed up of injection comes at a cost of reduced overall energy conversion efficiency. In addition, the slower non-100% efficient injection component appears to be a thermally activated process, proceeding through a pathway which is identical to the one taken by the non-injecting excited state decay pathways.

Chapter 7. Summary and further work

Electron injection in dye-sensitized solar cells was studied extensively in this thesis. One of the main experimental techniques used was transient absorption spectroscopy. It was found that samples which closely resemble working solar cells are quite robust for the TAS experiments both in terms of being stable against degradation and the samples not changing over time. It was found that at illumination levels equivalent to at least 15 suns (when integrating the absorbed pump pulse light over unit time), all the effects which arise due to illumination scale linearly with intensity where appropriate. To be more exact, transient absorption change and photocurrents were found to be linear. When on the order of a 100 suns light intensity was used, the results were much less predictable and huge ultrafast absorption change accompanied by fast decays on the order of picoseconds were observed. These observations were true for both organic dyes and for metal-organic complexes utilizing the ruthenium metal. In addition, no differences in the transient spectra were observed when the devices were measured at open circuit or at short circuit conditions. Also, sample transient absorption did not change over several hours of continuous illumination with the laser pump pulse. Sample translation was used in several cases and was shown to be unnecessary for the present study. To obtain reliable reference spectra, some of the dyes had their spectra recorded in the 800 – 8000 nm range when adsorbed on the non-injecting ZrO_2. These spectra correspond to the dye excited state spectra. To complement these, time resolved luminescence data was also taken. These spectra aided interpretation of the results when the dyes were adsorbed on TiO_2.

The devices utilizing the stable, performance optimized electrolytes with champion N719, Z907 or C106 dyes showed broad, multiphasic electron injection kinetics. When electrolytes with high concentration of lithium ions were used, the kinetics became predominantly ultrafast, with only a minor fraction of injection occurring at > 10 ps timescales. Comparing the TAS and TCSPC measurements it became clear that reliable injection efficiency determination from transient techniques is not possible, at least not with the equipment that was available during the PhD. A steady-state technique, called IPCE front/back method, was employed. It allowed a reliable determination of injection efficiency. Combining the results from steady state and transient measurements, a full picture of injection was obtained. Devices with slower, multiphasic kinetics resulted in 75-90% efficient injection, depending on the particular system. The addition of potential determining species to the electrolyte, specifically, driving the conduction band edge down by adding lithium ions, resulted in significantly faster injection and close to 100% injection efficiency. However, the V_{OC} of such devices was decreased considerably, yielding lower overall power

conversion efficiency. Hence there seems to be an injection rate/efficiency trade-off in DSSCs. One cannot have, at least not in the systems described in the present thesis, both 100% ultrafast kinetics and a high V_{OC}. The exact origins of these differences were not determined. Another interesting observation was made in the temperature dependence studies. It was found that injection proceeds via a thermally activated step, which is also present in all the other excited state decay pathways.

There are many unanswered questions that arise from the work of the PhD. The most important is the question whether it is possible to determine what exactly causes the degradation of injection efficiency when using high stability, high V_{OC} electrolytes and is it possible to overcome it. To answer this question, many parameters of the DSSC systems would have to be studied in relation to both, the injection kinetics and the efficiency. The parameters that would have to be varied in order to find their relation to injection are many, e.g. the solvent viscosity and dielectric coefficient; influence of other chemical components present in the electrolyte; treatment of the metal oxide surface and utilization of other metal oxides. The dyes are, however, the most interesting in terms of future work. Although similar in structure, but different injection efficiencies were obtained for ruthenium dyes. Many questions arise, such as why exactly is Z907 worse at injection than the less hydrophobic N719? Is the injection from the D149 dye dependent on the excitation wavelength? Is injection rate dependent on temperature only for injection from the thermalized triplet state, or from the singlet state as well? Answer to these questions would shed more light onto what exactly influences the injection rate and efficiency. Armed with these answers, researchers would be much better at designing new, high efficiency dyes and electrolytes.

References

1. Lewis NS (2007) Powering the Planet. *MRS Bulletin* 32(10):808-820.
2. Advancing the Science of Climate Change (2010), *The National Academies Press*.
3. Lewis NS & Nocera DG (2006) Powering the planet: Chemical challenges in solar energy utilization. *Proc. Natl. Acad. Sci. U. S. A.* 103(43):15729-15735.
4. Gratzel M (2001) Photoelectrochemical cells. *Nature* 414(6861):338-344.
5. Solar Cell Efficiency Graph (2014). *National Renewable Energy Laboratory, Colorado, US.*
6. Gregg BA (2003) Excitonic Solar Cells. *J. Phys. Chem. B* 107(20):4688-4698.
7. Kopola P*, et al.* (2011) Gravure printed flexible organic photovoltaic modules. *Sol. Energy Mater. Sol. Cells* 95(5):1344-1347.
8. Ramasamy E, Lee WJ, Lee DY, & Song JS (2007) Portable, parallel grid dye-sensitized solar cell module prepared by screen printing. *J. Power Sources* 165(1):446-449.
9. Oregan B & Gratzel M (1991) A Low-cost, High-efficiency Solar-cell Based on Dye-sensitized colloidal TiO2 Films. *Nature* 353(6346):737-740.
10. Deb SK (2005) Dye-sensitized TiO2 thin-film solar cell research at the National Renewable Energy Laboratory (NREL). *Sol. Energy Mater. Sol. Cells* 88(1):1-10.
11. Tsubomura H, Matsumura M, Nomura Y & Amamiya T (1976). Dye sensitised zinc oxide: aqueous electrolyte: platinum photocell. Nature, 261(5559), pp. 402-403
12. Moser J & Graetzel M (1984) Photosensitized electron injection in colloidal semiconductors. *J. Am. Chem. Soc.* 106(22):6557-6564.
13. ISI Web of Science, http://www.isiknowledge.com, accessed 2014-12-15.
14. Hagfeldt A & Gratzel M (2000) Molecular photovoltaics. *Acc. Chem. Res.* 33(5):269-277.
15. O'Regan BC & Durrant JR (2009) Kinetic and Energetic Paradigms for Dye-Sensitized Solar Cells: Moving from the Ideal to the Real. *Acc. Chem. Res.* 42(11):1799-1808.
16. Nelson, J (1999). *Physics of Solar Cells*. London: Imperial College Press
17. Gratzel M (2003) Dye-sensitized solar cells. *J. Photochem. Photobiol., C* 4(2):145-153.
18. Haque SA*, et al.* (2005) Charge Separation versus Recombination in Dye-Sensitized Nanocrystalline Solar Cells: the Minimization of Kinetic Redundancy. *J. Am. Chem. Soc.* 127(10):3456-3462.
19. Koops SE & Durrant JR (2008) Transient emission studies of electron injection in dye sensitised solar cells. *Inorg. Chim. Acta* 361(3):663-670.
20. O'Regan B, Moser J, Anderson M, & Graetzel M (1990) Vectorial electron injection into transparent semiconductor membranes and electric field effects on the dynamics of light-induced charge separation. *J. Phys. Chem* 94(24):8720-8726.
21. Fessenden RW & Kamat PV (1995) Rate Constants for Charge Injection from Excited Sensitizer into SnO2, ZnO, and TiO2 Semiconductor Nanocrystallites. *J. Phys. Chem* 99(34):12902-12906.
22. Eichberger W (1990) Ultrafast electron injection from excited dye molecules into semiconductor electrodes. *J. Chem. Phys.* 141(1):159-173
23. Tachibana Y, Moser JE, Gratzel M, Klug DR, & Durrant JR (1996) Subpicosecond Interfacial Charge Separation in Dye-Sensitized Nanocrystalline Titanium Dioxide Films. *J. Phys. Chem* 100(51):20056-20062.
24. Rehm JM, Mclendon GL., Nagasawa Y, Yoshihara K, Moser J, Gratzel MJ (1996) Femtosecond Electron-Transfer Dynamics at a Sensitizing Dye−Semiconductor (TiO2) Interface *J. Phys. Chem.* 100(23):9577-9578.
25. Burfeindt B, Hannappel T, Storck W, & Willig F (1996) Measurement of Temperature-Independent Femtosecond Interfacial Electron Transfer from an Anchored Molecular Electron Donor to a Semiconductor as Acceptor. *J. Phys. Chem* 100(41):16463-16465.

26. Kuciauskas D*, et al.* (2002) Transient Absorption Spectroscopy of Ruthenium and Osmium Polypyridyl Complexes Adsorbed onto Nanocrystalline TiO2 Photoelectrodes. *J. Phys. Chem. B* 106(36):9347-9358.
27. Katoh R*, et al.* (2002) Efficiencies of Electron Injection from Excited Sensitizer Dyes to Nanocrystalline ZnO Films as Studied by Near-IR Optical Absorption of Injected Electrons. *J. Phys. Chem. B* 106(50):12957-12964.
28. Benkö G, Kallioinen J, Korppi-Tommola JEI, Yartsev AP, & Sundström V (2001) Photoinduced Ultrafast Dye-to-Semiconductor Electron Injection from Nonthermalized and Thermalized Donor States. *J. Am. Chem. Soc.* 124(3):489-493.
29. Tachibana Y, Haque SA, Mercer IP, Durrant JR, & Klug DR (2000) Electron Injection and Recombination in Dye Sensitized Nanocrystalline Titanium Dioxide Films: A Comparison of Ruthenium Bipyridyl and Porphyrin Sensitizer Dyes. *J. Phys. Chem. B* 104(6):1198-1205.
30. Hannappel T, Burfeindt B, Storck W, & Willig F (1997) Measurement of Ultrafast Photoinduced Electron Transfer from Chemically Anchored Ru-Dye Molecules into Empty Electronic States in a Colloidal Anatase TiO2 Film. *J. Phys. Chem. B* 101(35):6799-6802.
31. Heimer TA & Heilweil EJ (1997) Direct Time-Resolved Infrared Measurement of Electron Injection in Dye-Sensitized Titanium Dioxide Films. *J. Phys. Chem. B* 101(51):10990-10993.
32. Ellingson RJ*, et al.* (1998) Dynamics of Electron Injection in Nanocrystalline Titanium Dioxide Films Sensitized with [Ru(4,4‘-dicarboxy-2,2‘-bipyridine)2(NCS)2] by Infrared Transient Absorption. *J. Phys. Chem. B* 102(34):6455-6458.
33. Ghosh HN, Asbury JB, & Lian T (1998) Direct Observation of Ultrafast Electron Injection from Coumarin 343 to TiO2 Nanoparticles by Femtosecond Infrared Spectroscopy. *J. Phys. Chem. B* 102(34):6482-6486.
34. Ghosh HN, Asbury JB, Weng Y, & Lian T (1998) Interfacial Electron Transfer between Fe(II)(CN)64- and TiO2 Nanoparticles: Direct Electron Injection and Nonexponential Recombination. *J. Phys. Chem. B* 102(50):10208-10215.
35. Moser JE*, et al.* (1998) Comment on "measurement of ultrafast photoinduced electron transfer from chemically anchored Ru-dye molecules into empty electronic states in a colloidal anatase TiO2 film". *J. Phys. Chem. B* 102(18):3649-3650.
36. Asbury JB*, et al.* (1999) Femtosecond IR Study of Excited-State Relaxation and Electron-Injection Dynamics of Ru(dcbpy)2(NCS)2 in Solution and on Nanocrystalline TiO2 and Al2O3 Thin Films. *J. Phys. Chem. B* 103(16):3110-3119.
37. Ghosh HN (1999) Charge Transfer Emission in Coumarin 343 Sensitized TiO2 Nanoparticle: A Direct Measurement of Back Electron Transfer. *J. Phys. Chem. B* 103(47):10382-10387.
38. Tachibana Y*, et al.* (2001) Modulation of the Rate of Electron Injection in Dye-Sensitized Nanocrystalline TiO2 Films by Externally Applied Bias. *J. Phys. Chem. B* 105(31):7424-7431.
39. Tachibana Y, Nazeeruddin MK, Grätzel M, Klug DR, & Durrant JR (2002) Electron injection kinetics for the nanocrystalline TiO2 films sensitised with the dye (Bu4N)2Ru(dcbpyH)2(NCS)2. *Chem. Phys.* 285(1):127-132.
40. Kallioinen J*, et al.* (2004) Photoinduced Ultrafast Dynamics of Ru(dcbpy)2(NCS)2-Sensitized Nanocrystalline TiO2 Films: The Influence of Sample Preparation and Experimental Conditions. *J. Phys. Chem. B* 108(20):6365-6373.
41. Ai X, Anderson NA, Guo J, & Lian T (2005) Electron Injection Dynamics of Ru Polypyridyl Complexes on SnO2 Nanocrystalline Thin Films. *J. Phys. Chem. B* 109(15):7088-7094.
42. Katoh R*, et al.* (2004) Efficiencies of Electron Injection from Excited N3 Dye into Nanocrystalline Semiconductor (ZrO2, TiO2, ZnO, Nb2O5, SnO2, In2O3) Films. *J. Phys. Chem. B* 108(15):4818-4822.
43. Furube A*, et al.* (2003) Ultrafast Stepwise Electron Injection from Photoexcited Ru-Complex into Nanocrystalline ZnO Film via Intermediates at the Surface. *J. Phys. Chem. B* 107(17):4162-4166.

44. Stockwell D*, et al.* (2010) Comparison of Electron-Transfer Dynamics from Coumarin 343 to TiO2, SnO2, and ZnO Nanocrystalline Thin Films: Role of Interface-Bound Charge-Separated Pairs. *J. Phys. Chem. C* 114(14):6560-6566.
45. Anderson NA & Lian T (2005) ULTRAFAST ELECTRON TRANSFER AT THE MOLECULE-SEMICONDUCTOR NANOPARTICLE INTERFACE. *Annu. Rev. Phys. Chem.* 56(1):491-519.
46. Paoprasert P*, et al.* (2010) Bridge-Dependent Interfacial Electron Transfer from Rhenium−Bipyridine Complexes to TiO2 Nanocrystalline Thin Films. *J. Phys. Chem. C* 114(21):9898-9907.
47. She C*, et al.* (2007) Comparison of Interfacial Electron Transfer through Carboxylate and Phosphonate Anchoring Groups†. *J. Phys. Chem. A* 111(29):6832-6842.
48. Asbury JB, Anderson NA, Hao E, Ai X, & Lian T (2003) Parameters Affecting Electron Injection Dynamics from Ruthenium Dyes to Titanium Dioxide Nanocrystalline Thin Film†. *J. Phys. Chem. B* 107(30):7376-7386.
49. Bergeron BV, Kelly CA, & Meyer GJ (2003) Thin Film Actinometers for Transient Absorption Spectroscopy: Applications to Dye-Sensitized Solar Cells. *Langmuir* 19(20):8389-8394.
50. Ardo S, Sun Y, Staniszewski A, Castellano FN, & Meyer GJ (2010) Stark Effects after Excited-State Interfacial Electron Transfer at Sensitized TiO2 Nanocrystallites. *J. Am. Chem. Soc.*
51. Katoh R, Huijser A, Hara K, Savenije TJ, & Siebbeles LDA (2007) Effect of the Particle Size on the Electron Injection Efficiency in Dye-Sensitized Nanocrystalline TiO2 Films Studied by Time-Resolved Microwave Conductivity (TRMC) Measurements. *J. Phys. Chem. C* 111(28):10741-10746.
52. Du L, Furube A, Hara K, Katoh R, & Tachiya M (2010) Mechanism of Particle Size Effect on Electron Injection Efficiency in Ruthenium Dye-Sensitized TiO2 Nanoparticle Films. *J. Phys. Chem. C* 114(18):8135-8143.
53. Haque SA*, et al.* (2000) Parameters Influencing Charge Recombination Kinetics in Dye-Sensitized Nanocrystalline Titanium Dioxide Films. *J. Phys. Chem. B* 104(3):538-547.
54. Tachibana Y*, et al.* (2001) Transient luminescence studies of electron injection in dye sensitised nanocrystalline TiO2 films. *Journal of Photochemistry and Photobiology A: Chemistry* 142(2-3):215-220.
55. Benkö G*, et al.* (2004) Interligand Electron Transfer Determines Triplet Excited State Electron Injection in RuN3−Sensitized TiO2 Films. *J. Phys. Chem. B* 108(9):2862-2867.
56. Wenger B, Grätzel M, & Moser J-E (2005) Rationale for Kinetic Heterogeneity of Ultrafast Light-Induced Electron Transfer from Ru(II) Complex Sensitizers to Nanocrystalline TiO2. *J. Am. Chem. Soc.* 127(35):12150-12151.
57. Pellnor M, Myllyperkiö P, Korppi-Tommola J, Yartsev A, & Sundström V (2008) Photoinduced interfacial electron injection in RuN3-TiO2 thin films: Resolving picosecond timescale injection from the triplet state of the protonated and deprotonated dyes. *Chem. Phys. Lett.* 462(4-6):205-208.
58. Barnes PRF, Anderson AY, Koops SE, Durrant JR, & O'Regan BC (2008) Electron Injection Efficiency and Diffusion Length in Dye-Sensitized Solar Cells Derived from Incident Photon Conversion Efficiency Measurements. *J. Phys. Chem. C* 113(3):1126-1136.
59. Koops SE, O'Regan BC, Barnes PRF, & Durrant JR (2009) Parameters Influencing the Efficiency of Electron Injection in Dye-Sensitized Solar Cells. *J. Am. Chem. Soc.* 131(13):4808-4818.
60. Bai Y, Zhang J, Wang Y, Zhang M, & Wang P (2011) Lithium-Modulated Conduction Band Edge Shifts and Charge-Transfer Dynamics in Dye-Sensitized Solar Cells Based on a Dicyanamide Ionic Liquid. *Langmuir* 27(8):4749-4755.
61. Pijpers JJH, Ulbricht R, Derossi S, Reek JNH, & Bonn M (2011) Picosecond Electron Injection Dynamics in Dye-Sensitized Oxides in the Presence of Electrolyte. *J. Phys. Chem. C* 115(5):2578-2584.
62. Fakis M, Stathatos E, Tsigaridas G, Giannetas V, & Persephonis P (2011) Femtosecond Decay and Electron Transfer Dynamics of the Organic Sensitizer D149 and Photovoltaic

Performance in Quasi-Solid-State Dye-Sensitized Solar Cells. *J. Phys. Chem. C* 115(27):13429-13437.
63. Sunahara K*, et al.* (2011) Coexistence of Femtosecond- and Nonelectron-Injecting Dyes in Dye-Sensitized Solar Cells: Inhomogeniety Limits the Efficiency. *J. Phys. Chem. C* 115(44):22084-22088.
64. Ziolek M*, et al.* (2012) Femtosecond to millisecond studies of electron transfer processes in a donor-([small pi]-spacer)-acceptor series of organic dyes for solar cells interacting with titania nanoparticles and ordered nanotube array films. *Phys. Chem. Chem. Phys.* 14(8):2816-2831.
65. Griffith MJ*, et al.* (2012) Porphyrins for dye-sensitised solar cells: new insights into efficiency-determining electron transfer steps. *Chem. Commun.* 48(35):4145-4162.
66. Tian H*, et al.* (2009) Tuning of phenoxazine chromophores for efficient organic dye-sensitized solar cells. *Chem. Commun.* (41):6288-6290.
67. Milot RL, Moore GF, Crabtree RH, Brudvig GW, & Schmuttenmaer CA (2013) Electron Injection Dynamics from Photoexcited Porphyrin Dyes into SnO2 and TiO2 Nanoparticles. *J. Phys. Chem. C* 117(42):21662-21670.
68. Sobuś J*, et al.* (2014) Comparison of TiO2 and ZnO Solar Cells Sensitized with an Indoline Dye: Time-Resolved Laser Spectroscopy Studies of Partial Charge Separation Processes. *Langmuir* 30(9):2505-2512.
69. Sharma D*, et al.* (2013) Impact of the Anchoring Ligand on Electron Injection and Recombination Dynamics at the Interface of Novel Asymmetric Push–Pull Zinc Phthalocyanines and TiO2. *J. Phys. Chem. C* 117(48):25397-25404.
70. Cid J-J*, et al.* (2007) Molecular Cosensitization for Efficient Panchromatic Dye-Sensitized Solar Cells13. *Angewandte Chemie International Edition* 46(44):8358-8362.
71. Teuscher J*, et al.* (2012) Photoinduced Interfacial Electron Injection Dynamics in Dye-Sensitized Solar Cells under Photovoltaic Operating Conditions. *J Phys Chem Lett* 3(24):3786-3790.
72. Barbé CJ*, et al.* (1997) Nanocrystalline Titanium Oxide Electrodes for Photovoltaic Applications. *J. Am. Ceram. Soc.* 80(12):3157-3171.
73. Yoon M-C, Cho S, & Kim D (2004) Femtosecond coherent spectroscopic study of Zn(II)porphyrin by chirping-controlled ultrashort pulses. *14th International Conference on Ultrafast Phenomena*, (Optical Society of America), p TuE28.
74. Polli D, Brida D, Mukamel S, Lanzani G, & Cerullo G (2010) Effective temporal resolution in pump-probe spectroscopy with strongly chirped pulses. *Phys. Rev. A* 82(5):053809.
75. Shen Y-C & Cina JA (1999) What can short-pulse pump-probe spectroscopy tell us about Franck-Condon dynamics? *J. Chem. Phys.* 110(20):9793-9806.
76. Yan S, Seidel MT, & Tan H-S (2011) Perturbed free induction decay in ultrafast mid-IR pump–probe spectroscopy. *Chem. Phys. Lett.* 517(1–3):36-40.
77. Ekvall K*, et al.* (2000) Cross phase modulation artifact in liquid phase transient absorption spectroscopy. *J. Appl. Phys.* 87(5):2340-2352.
78. Wilson JW, Samineni P, Warren WS, & Fischer MC (2012) Cross-phase modulation spectral shifting: nonlinear phase contrast in a pump-probe microscope. *Biomed. Opt. Express* 3(5):854-862.
79. Oppenheim A, Shafer R (1998). *Discrete time signal processing.* New Jersey: Prentice Hall.
80. Boens N*, et al.* (2007) Fluorescence Lifetime Standards for Time and Frequency Domain Fluorescence Spectroscopy. *Anal. Chem.* 79(5):2137-2149.
81. Anderson NA & Lian T (2004) Ultrafast electron injection from metal polypyridyl complexes to metal-oxide nanocrystalline thin films. *Coord. Chem. Rev.* 248(13-14):1231-1246.
82. She C, Guo J, & Lian T (2007) Comparison of Electron Injection Dynamics from Re-bipyridyl Complexes to TiO2 Nanocrystalline Thin Films in Different Solvent Environments†. *J. Phys. Chem. B* 111(24):6903-6912.

83. Juozapavicius M, Kaucikas M, van Thor JJ, & O'Regan BC (2013) Observation of Multiexponential Pico- to Subnanosecond Electron Injection in Optimized Dye-Sensitized Solar Cells with Visible-Pump Mid-Infrared-Probe Transient Absorption Spectroscopy. *J. Phys. Chem. C* 117(1):116-123.
84. Horiuchi T, Miura H, Sumioka K, & Uchida S (2004) High Efficiency of Dye-Sensitized Solar Cells Based on Metal-Free Indoline Dyes. *J. Am. Chem. Soc.* 126(39):12218-12219.
85. O'Regan BC*, et al.* (2009) Structure/Function Relationships in Dyes for Solar Energy Conversion: A Two-Atom Change in Dye Structure and the Mechanism for Its Effect on Cell Voltage. *J. Am. Chem. Soc.* 131(10):3541-3548.
86. Nazeeruddin MK, Humphry-Baker R, Liska P, & Grätzel M (2003) Investigation of Sensitizer Adsorption and the Influence of Protons on Current and Voltage of a Dye-Sensitized Nanocrystalline TiO2 Solar Cell. *J. Phys. Chem. B* 107(34):8981-8987.
87. Antila LJ, Myllyperkiö P, Mustalahti S, Lehtivuori H, & Korppi-Tommola J (2014) Injection and Ultrafast Regeneration in Dye-Sensitized Solar Cells. *J. Phys. Chem. C* 118(15):7772-7780.
88. Kim H, Park S, & Cho M (2012) Rotational dynamics of thiocyanate ions in highly concentrated aqueous solutions. *Phys. Chem. Chem. Phys.* 14(18):6233-6240.
89. Barnes PRF & O'Regan BC (2010) Electron Recombination Kinetics and the Analysis of Collection Efficiency and Diffusion Length Measurements in Dye Sensitized Solar Cells. *J. Phys. Chem. C* 114(44):19134-19140.
90. Redmond G & Fitzmaurice D (1993) Spectroscopic determination of flatband potentials for polycrystalline titania electrodes in nonaqueous solvents. *J. Phys. Chem* 97(7):1426-1430.
91. Haque SA, Tachibana Y, Klug DR, & Durrant JR (1998) Charge Recombination Kinetics in Dye-Sensitized Nanocrystalline Titanium Dioxide Films under Externally Applied Bias. *J. Phys. Chem. B* 102(10):1745-1749.
92. Lohse PW*, et al.* (2011) Ultrafast photoinduced relaxation dynamics of the indoline dye D149 in organic solvents. *Phys. Chem. Chem. Phys.* 13(43):19632-19640.
93. Enright B, Redmond G, & Fitzmaurice D (1994) Spectroscopic determination of flatband potentials for polycrystalline TiO2 electrodes in mixed solvent systems. *J. Phys. Chem* 98(24):6195-6200.
94. Warren MM*, et al.* (2013) Ground-state proton transfer in the photoswitching reactions of the fluorescent protein Dronpa. *Nat Commun* 4:1461.
95. Schwarz O, van Loyen D, Jockusch S, J. Turro N, & Dürr H (2000) Preparation and application of new ruthenium(II) polypyridyl complexes as sensitizers for nanocrystalline TiO2. *Journal of Photochemistry and Photobiology A: Chemistry* 132(1–2):91-98.
96. Anderson AY, Barnes PRF, Durrant JR, & O'Regan BC (2010) Simultaneous Transient Absorption and Transient Electrical Measurements on Operating Dye-Sensitized Solar Cells: Elucidating the Intermediates in Iodide Oxidation. *J. Phys. Chem. C* 114(4):1953-1958.
97. Jennings JR, Liu Y, & Wang Q (2011) Efficiency Limitations in Dye-Sensitized Solar Cells Caused by Inefficient Sensitizer Regeneration. *J. Phys. Chem. C* 115(30):15109-15120.
98. Iwai S*, et al.* (2000) Ultrafast interfacial charge separation processes from the singlet and triplet MLCT states of Ru(bpy)[sub 2](dcbpy) adsorbed on nanocrystalline SnO[sub 2] under negative applied bias. *J. Chem. Phys.* 113(8):3366-3373.
99. Juozapavicius M*, et al.* (2013) Evidence for "Slow" Electron Injection in Commercially Relevant Dye-Sensitized Solar Cells by vis–NIR and IR Pump–Probe Spectroscopy. *J. Phys. Chem. C* 117(48):25317-25324.
100. Nazeeruddin MK*, et al.* (2005) Combined Experimental and DFT-TDDFT Computational Study of Photoelectrochemical Cell Ruthenium Sensitizers. *J. Am. Chem. Soc.* 127(48):16835-16847.
101. Barnes PRF, Miettunen K, Li X, Anderson A, Bessho T, Gratzel M & O'Regan B (2013) Interpretation of Optoelectronic Transient and Charge Extraction Measurements in Dye-Sensitized Solar Cells. *Adv. Mater.* 25(13):1881-1922

102. Murai M, Furube A, Yanagida M, Hara K, & Katoh R (2006) Near-IR transient absorption spectra of N3 dye as a probe of aggregation on nanocrystalline semiconductor films. *Chem. Phys. Lett.* 423(4-6):417-421.
103. Robertson J (2000) Band offsets of wide-band-gap oxides and implications for future electronic devices. *Journal of Vacuum Science & Technology B* 18(3):1785-1791.
104. Listorti A*, et al.* (2011) The mechanism behind the beneficial effect of light soaking on injection efficiency and photocurrent in dye sensitized solar cells. *Energy Environ. Sci.* 4(9):3494-3501.
105. Lyon JE, Rayan MK, Beerbom MM, Schlaf R (2008) Electronic structure of the indium tin oxide/nanocrystalline anatase (TiO2)/ruthenium-dye interfaces in dye-sensitized solar cells. *J. Appl. Phys.* 104, 073714.
106. Kallioinen J, Benkö G, Sundström V, Korppi-Tommola JEI, & Yartsev AP (2002) Electron Transfer from the Singlet and Triplet Excited States of Ru(dcbpy)2(NCS)2 into Nanocrystalline TiO2 Thin Films. *J. Phys. Chem. B* 106(17):4396-4404.
107. Juozapavicius M, O'Regan BC, Anderson AY, Grazulevicius JV, & Mimaite V (2012) Efficient dye regeneration in solid-state dye-sensitized solar cells fabricated with melt processed hole conductors. *Organic Electronics* 13(1):23-30.
108. Yu Q*, et al.* (2010) High-Efficiency Dye-Sensitized Solar Cells: The Influence of Lithium Ions on Exciton Dissociation, Charge Recombination, and Surface States. *ACS Nano* 4(10):6032-6038.
109. Anderson AY, Barnes PRF, Durrant JR, & O'Regan BC (2011) Quantifying Regeneration in Dye-Sensitized Solar Cells. *J. Phys. Chem. C* 115(5):2439-2447.
110. Lide DR (2001). *CRC handbook of physics and chemistry.* Cleveland, OH: The Chemical Rubber Company.